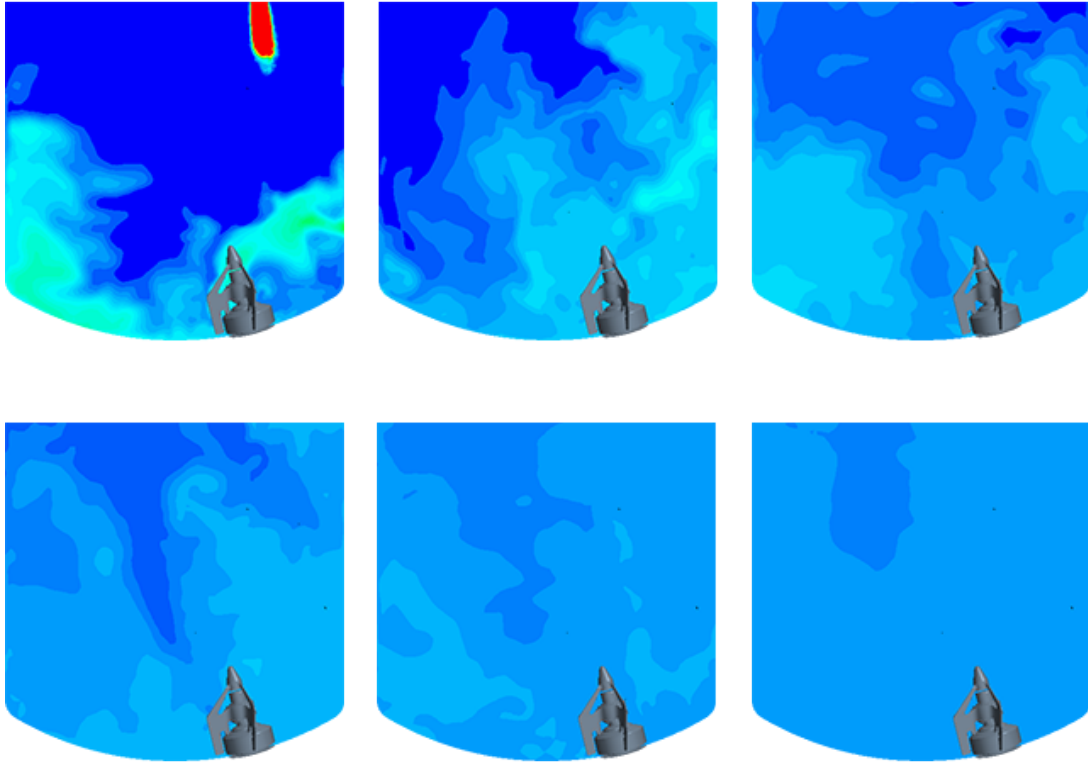




CHALMERS



CFD Simulations of Mixing using a Magnetically Driven Impeller

Method Development and Validation Study

Master's thesis in Applied Mechanics

CAROLINE OLOFSSON

EMMA SUNDELL

MASTER'S THESIS IN APPLIED MECHANICS

CFD Simulations of Mixing using a Magnetically Driven Impeller

Method Development and Validation Study

CAROLINE OLOFSSON
EMMA SUNDELL

Department of Mechanics and Maritime Sciences
Division of Fluid Dynamics
CHALMERS UNIVERSITY OF TECHNOLOGY
Göteborg, Sweden 2019

CFD Simulations of Mixing using a Magnetically Driven Impeller
Method Development and Validation Study
CAROLINE OLOFSSON
EMMA SUNDELL

© CAROLINE OLOFSSON , EMMA SUNDELL, 2019

Master's thesis 2018:98
Department of Mechanics and Maritime Sciences
Division of Fluid Dynamics
Chalmers University of Technology
SE-412 96 Göteborg
Sweden
Telephone: +46 (0)31-772 1000

Cover:

Pictures at every 6 seconds of tracer concentration for a mixing process from a simulation using LES as turbulence model.

Chalmers Reproservice
Göteborg, Sweden 2019

CFD Simulations of Mixing using a Magnetically Driven Impeller
Method Development and Validation Study
Master's thesis in Applied Mechanics
CAROLINE OLOFSSON
EMMA SUNDELL
Department of Mechanics and Maritime Sciences
Division of Fluid Dynamics
Chalmers University of Technology

ABSTRACT

Mixing with impellers is common in many industries. By using CFD methods, more knowledge about the mixing process can be gained since it is relatively difficult to examine experimentally. Two common turbulence models used for active mixing are the RANS and LES models. RANS methods have the advantage of being relatively cheap in terms of computational effort, whereas the more demanding LES method usually results in higher accuracy. FS Dynamics has performed CFD simulations of active mixing using a RANS method. In this study, the purpose was to improve and validate this existing method. The method has been extended by implementing LES as turbulence model. The LES was implemented together with wall functions to lower the computational demand. A tracer, inserted using two different methods, has been used for tracking the mixing processes. The first method replaces some water inside the tank with a fixed volume of tracer. The second method has an inlet of tracer to mimic pouring from physical tests, which were also conducted during this project. Both methods were used for the RANS simulations whereas only the second method was used for LES.

Using a fixed volume of tracer placed beneath the surface resulted in a mixing process starting with a higher concentration at the top, spreading downwards. Using an inlet of tracer resulted in a higher tracer concentration in the bottom of the tank, which was then mixed upwards. Regarding the mixing time, the LES gave results that correspond to the physical tests and the RANS model overpredicted the mixing time by 50%.

The robustness of the method using a fixed volume of tracer was evaluated by changing both the volume of tracer and its position and shape. Changing the volume from approximately 3 to 25 litres did not affect the mixing time substantially. Using different shapes and positions resulted in varying mixing time results. Changing the Schmidt number between 1 – 8000 or the dynamic viscosity between approximately $0.9 \cdot 10^{-3}$ – $1.7 \cdot 10^{-3}$ kg/ms did not affect the mixing times.

Keywords: Computational Fluid Dynamics (CFD), Reynolds-Averaged Navier Stokes (RANS), Large Eddy Simulation (LES), Simcenter STAR-CCM+, active mixing, magnetically driven impeller

PREFACE

This master's thesis has been performed during the fall of 2018 by Caroline Olofsson and Emma Sundell, students at the master's program Applied Mechanics at Chalmers University of Technology. The thesis was performed at FS Dynamics in collaboration with Metenova, where Metenova both provided the CAD geometries and helped with the physical testing. The project was supervised by Fredrik Carlsson and David Frisk at FS Dynamics and examined by Lars Davidson at the Division of Fluid Dynamics at Chalmers University of Technology.

ACKNOWLEDGEMENTS

We would like to thank our supervisors at FS Dynamics, Fredrik Carlsson and David Frisk, for their support and feedback during this project. Fredrik has supported us with his great expertise in fluid dynamics in general, and turbulence modelling in particular. David has been available during the whole process and helped us with all kinds troubles along the way. From Chalmers University of Technology, we would like to thank Lars Davidson for being our examiner. The knowledge that we have gained during his courses in fluid mechanics has been crucial to be able to accomplish this thesis. We would like to thank Alf Löfving and Therese Persson at Metenova for the collaboration in this thesis, and especially Therese for helping us with the physical testing and answering all our questions about the impeller. To our colleagues at FS Dynamics, and to our fellow thesis workers Filip Ljungström and Sofia Alexandersson, we would like to give a special thank you for making us feel welcome and for showing an interest in our project.

ABBREVIATIONS

CAD	Computer-Aided Design
CFD	Computational Fluid Dynamics
CFL	Courant–Friedrichs–Lewy
CP	Conductivity Point
CPU	Central Processing Unit
DES	Detached Eddy Simulation
FVM	Finite Volume Method
LES	Large Eddy Simulation
MRF	Moving Reference Frame
RANS	Reynolds-Averaged Navier Stokes
SM	Sliding Mesh

NOMENCLATURE

Greek Letters

γ_M	Compressibility modification	[kg/s ³ m]	l_ε	Length scale function in two-layer model	[m]
Δ	Grid filter size	[m]	N	Rotational speed in rounds per second	[1/s]
δ	Boundary layer thickness	[m]	N_Q	Pumping number	[-]
δ_{ij}	Kronecker delta	[-]	P	Shaft power	[kgm ² /s ³]
ε	Turbulent dissipation rate	[m ² /s ³]	p	Pressure	[kg/ms ²]
κ	Conductivity	[s ³ A ² /kgm ³]	P_0	Power number	[-]
$\bar{\kappa}_t$	Mean conductivity in tank	[s ³ A ² /kgm ³]	P_ε	Production term in the ε -equation	[kg/s ⁴ m]
μ	Dynamic viscosity	[kg/ms]	P^k	Production term in the k-equation	[kg/s ³ m]
μ_{sgs}	Subgrid turbulent dynamic viscosity	[m ² /s]	Q_p	Volumetric flow rate	[m ³ /s]
μ_t	Turbulent dynamic viscosity	[kg/ms]	Re	Reynolds number	[-]
ν	Kinematic viscosity	[m ² /s]	S_ε	Source term in the ε -equation	[kg/s ⁴ m]
ρ	Density	[kg/m ³]	Sc_s	Schmidt number for species s	[-]
$\sigma_k, \sigma_\varepsilon$	Turbulent Prandtl numbers	[-]	s_{ij}	Strain rate tensor	[1/s]
σ_t	Turbulent Schmidt number	[-]	S^k	Source term in the k-equation	[kg/s ³ m]
τ_{95}	Mixing time for 95% mixing	[s]	S_{Y_s}	Source term in the mass fraction transport equation for species s	[kg/sm ³]
τ_{ij}	Reynolds stress tensor	[m ² /s ²]	Δt	Time step size	[s]
τ_w	Wall shear stress	[kg/ms ²]	t	Time	[s]
Ω_{ij}	Vorticity tensor	[1/s]	T_{ij}	Viscous stress tensor	[m ² /s ²]

Roman Letters

c	Volume concentration	[-]	T_Q	Impeller torque	[Nm]
$c_{\varepsilon 1}, c_{\varepsilon 2}$	Constants in the modelled ε -equation	[-]	u	Wall parallel velocity	[m/s]
c_μ	Constant for k- ε models	[-]	u^*	Frictional velocity	[m/s]
CFL	Courant–Friedrichs–Lewy number	[-]	u^+	Non-dimensional wall parallel velocity	[-]
C_S	Coefficient in Smagorinsky model	[-]	V	Volume	[m ³]
\bar{c}_t	Mean volume concentration in tank	[-]	v	Velocity magnitude	[m/s]
CV	Coefficient of variance of tracer concentration	[-]	V_c	Cell volume	[m ³]
D	Impeller diameter	[m]	v_i	Velocity component i	[m/s]
$D_{s,m}$	Molecular diffusivity of species s	[m ² /s]	Δx_i	Cell size	[m]
f_2	Damping function in ε -equation	[-]	x_i	Position component i	[m]
f_μ	Damping function for μ_t	[-]	y	Wall normal distance	[m]
f_c	Curvature correction factor	[-]	y^+	Non-dimensional wall normal distance	[-]
f_i	Body force	[kg/m ² s ²]	Y_s	Mass fraction of species s	[-]
G^k	Turbulent production in k-equation	[kg/s ³ m]	Averaging notation		
k	Turbulent kinetic energy	[m ² /s ²]	$\langle \Phi \rangle$	Time-averaged quantity	
k_{sgs}	Subgrid turbulent kinetic energy	[m ² /s ²]	$\bar{\Phi}$	Filtered quantity	
\mathcal{L}_{ij}	Leonard stresses	[m ² /s ²]	Φ'	Time fluctuating quantity	
			Φ''	Spatially fluctuating quantity	

CONTENTS

Abstract	i
Preface	iii
Acknowledgements	iii
Abbreviations	v
Nomenclature	vii
Contents	ix
1 Introduction	1
1.1 Background	1
1.2 Purpose and Objectives	2
1.3 Delimitations	3
1.4 Report Structure	3
2 Theory	4
2.1 Computational Fluid Dynamics	4
2.1.1 Finite Volume Method	4
2.1.2 Reynolds-Averaged Navier Stokes Equations	5
2.1.3 Large Eddy Simulation	8
2.1.4 Transport of Species in a Mixture	9
2.1.5 Boundary Layer Flow	9
2.2 Mixing with Impellers	10
2.2.1 Metenova ZG5 Magnetic Mixer	10
2.2.2 Moving Reference Frame	11
2.2.3 Sliding Mesh	11
2.2.4 Impeller Reynolds Number	11
2.2.5 Power Number	11
2.2.6 Pumping Number	11
2.2.7 Mixing Time Definition	12
3 Physical Testing	13
3.1 Mixing Time using Conductivity Meters	13
3.2 Power Number from Experiments	15
4 Simulation Procedure	16
4.1 Computational Domain and Mesh	16
4.2 Simulation Start-up	17
4.3 Tracer Introduction	17
4.3.1 Method T1: Fixed Volume	17
4.3.2 Method T2: Pouring	17
4.4 Evaluation of Mixing Parameters	18
4.4.1 Mixing Time	18
4.4.2 Power Number	18
4.4.3 Pumping Number	19
4.5 Reynolds-Averaged Navier Stokes Simulations	19
4.6 Large Eddy Simulations	19
4.7 Existing Simulation Method	20

5 Meshes	21
5.1 Mesh Study for RANS Simulations	21
5.1.1 Flow Characteristics	21
5.1.2 Mixing	26
5.2 Final Meshes used for RANS Simulations	27
5.3 Mesh Study for LES	28
5.4 Final Meshes used for LES	29
6 Validation Study	33
6.1 Mixing Process	33
6.2 Mixing Time	34
6.3 Power Number	36
6.4 Pumping Number	37
6.5 Computational Requirements	37
7 Evaluation of Simulation Method	39
7.1 Volume of Tracer	39
7.2 Shape and Placement of Tracer	39
7.3 Influence of Schmidt Number and Viscosity	40
7.4 Evaluation of Mixing Time	41
7.5 Evaluation of Pumping Number	43
8 Conclusions and Future Work Recommendations	44
References	46
Appendices	47
A Conductivity curves from physical testing	48
A.1 105 rpm	48
A.2 135 rpm	49
A.3 170 rpm	50
A.4 210 rpm	51
B Results from physical testing using vertical alignment of conductivity probes	52
C Meshes	53
C.1 RANS - Mesh study	53
C.1.1 RANS - A: Rotational region	53
C.1.2 RANS - B: Stationary region	55
C.1.3 RANS - C: Boundary layer	57
C.2 RANS - Final meshes	58
C.3 LES - Mesh study	59
C.4 LES - Final mesh	61
D Mixing process at 105 rpm	62
D.1 RANS T1	62
D.2 RANS T2	63
D.3 LES T2	64
D.4 Normalized tracer concentration at conductivity points	65
E Mixing process for different tracer shapes and placements	66
E.1 S1	66
E.2 S2	67
E.3 S3	68
E.4 S4	69

1 Introduction

Mixing of different fluids using an impeller mounted inside a tank is common in many different industries, such as the oil and gas, plastic, chemical processing and biotechnology. Using active mixing, new substances and solutions can be made in a controlled and efficient manner. By examining the mixing process, knowledge can be gained on how to design both the tank and impeller to the specific mixing application and also how to efficiently perform the process in terms of rotational velocity of the impeller and amount of liquid. There are often several parameters to take into consideration when choosing the configuration of the setup. This could for example be to optimize the total mixing time for complete mixing of two different fluids, or decide how to perform the mixing in order to trigger some sort of reaction that creates new substances. Furthermore, for some applications it is important to limit the shear acting on the fluid, for example when mixing enzymes that can be damaged.

Performing experiments while developing new impellers and tank designs can be both time consuming and expensive. To make the development faster and more cost efficient, Computational Fluid Dynamics (CFD) can be used. By using CFD methods, a better understanding of the mixing process can be achieved, since it is often difficult to examine the process experimentally. Furthermore, some important parameters, such as the magnitude of shear forces, can also be difficult to obtain from physical tests. There are several different methods to use within CFD, some more appropriate for active mixing applications than others. It is often more computationally demanding to use a more accurate method than using a less accurate, which means that it is not always trivial how to choose the most appropriate method.

FS Dynamics, which is a consultancy company specializing in advanced simulations of fluid and structural dynamics, has performed CFD simulations for active mixing applications using a Reynolds-Averaged Navier Stokes (RANS) method. In RANS simulations, all turbulence is modelled statistically. The Moving Reference Frame (MRF) method has been used for modelling the rotation of the impeller. However, RANS models often fail to predict the behaviour of mixing, since it is known that mixing is usually governed by non-local large-scale dynamics. Hence, it is of interest to evaluate the mixing performance in active mixing applications of the RANS method with an MRF.

A method which usually is more accurate than the RANS model is to use the Large Eddy Simulation (LES) as turbulence model, which resolves the large-scale turbulence. Both RANS and LES simulations were performed in this study. These methods were then validated against physical tests, which also were conducted during the project. The LES model was used together with wall functions to save computational effort, which means that the whole boundary layer is not resolved as it should be in a pure LES. This is a simplified LES that often does not perform as good as a pure LES, but is expected to work well in this type of application. Since LES is a fully transient method the rotation is modelled with a transient method, in this case Sliding Mesh (SM). LES is usually a more computationally demanding method than RANS simulations, which often makes it unsuitable for industrial projects, but the accuracy is commonly higher. However, since the computational power keeps increasing, LES is becoming more feasible to use also in the industry.

Both the impeller and tank geometry for this project were provided by Metenova, which is a company that provides mixer solutions primarily to the pharmaceutical and biotech sector. The impeller is of model Metenova ZG5 Magnetic Mixer and was placed in a 300 litre tank. The commercial software Simcenter STAR-CCM+ v13.06.011 from Siemens PLM Software was used for the simulations. To investigate the mixing performance, four different rotational speeds of the impeller have been simulated with a tracer inserted into the computational domain. The tracer concentration was then tracked until fully mixed conditions were achieved.

1.1 Background

A literature study was performed during the project to gain knowledge of what has been done in the field of CFD simulations of mixing with impellers. A short overview of the outcome is presented here. All studies mentioned have used one or two radial impellers placed in the center of a tank.

For mixing simulations with impellers the most commonly used turbulence modeling approaches are the RANS and LES methods. The RANS method is often used with MRF, while LES simulations are applied

with SM. Mendoza-Escamilla et al.[16] have shown that the MRF approach delivers good approximations of both the power and pumping numbers. According to Delafosse et al.[7], both LES and RANS simulations are good at predicting the mean flow field, however RANS simulations do not predict turbulent quantities to such a satisfactory extent as LES. Li and Xu[15] also state that RANS methods can successfully predict the mean flow field and flow patterns, but do not capture the turbulent structures. Furthermore, they state that LES on the other hand is better at capturing turbulent fluctuations, but since it has high demands regarding cell size and time step size it requires more Central Processing Unit (CPU) time to simulate a mixing process than a RANS simulation. Because LES is more computationally demanding, Torotwa and Ji [21] conclude that the RANS models are the most suitable models to use for realistic economical studies of active mixing.

Haringa et al.[10] have in their study shown that RANS simulations with MRF, using both the realizable $k-\varepsilon$ turbulence model and the Reynolds stress model, overpredict the mixing time with around 60%. Furthermore they have also shown that an LES simulation slightly underpredicts the mixing time with about 13% when using a coarse mesh. Using a finer mesh, they achieved results that agreed with experimental results.

For RANS simulations, the choice of turbulence model can have an impact on the accuracy of the results. According to Li and Xu[15], the standard $k-\varepsilon$, the RNG $k-\varepsilon$ and the Reynolds stress model are commonly used turbulence models for active mixing that all have proven to successfully predict the patterns of the flow. Mendoza-Escamilla et al.[16] have in their evaluation of different turbulence models in an active mixing application shown that the realizable $k-\varepsilon$ is better at predicting turbulent quantities in the flow than the standard and RNG $k-\varepsilon$.

Apart from the RANS and LES models, Detached Eddy Simulation (DES) is a possible method to use for active mixing simulations. DES is a mixture of LES and RANS methods, where RANS equations are solved inside the boundary layer and LES is used elsewhere [6]. DES requires less CPU time than LES, since the boundary layer mesh does not need to be as fine, but the accuracy is more comparable with results from LES than RANS simulations[6]. Li and Xu[15] have shown that mixing times calculated using DES were close to experimental results. From comparing the flow in experiments with DES, Chara et al.[4] have shown that DES is good at predicting the turbulent flow in active mixing.

1.2 Purpose and Objectives

The purpose of this master's thesis is to improve and validate an existing method, based on the RANS equations, that FS Dynamics has been using for some of their CFD simulations of active mixing.

To fulfill this purpose, the following objectives have been set:

- Decide how to perform the CFD simulations of a mixing application using a magnetically driven impeller inside a tank. Specific consideration is given to the implementation of tracer into the simulations.
- Extend the method by implementing LES as turbulence model. Wall functions are used to lower the computational demand.
- Plan and perform physical tests at Metenova's test lab to use as validation for the CFD simulations.
- Compare the results from RANS simulations, LES simulations and physical tests.
- Perform a mesh sensitivity study to establish recommendations for mesh creation.
- Evaluate the robustness of the simulation models in terms of changing the Schmidt number of the mixture, the viscosity and density of the tracer, the amount of tracer and how the tracer is initiated.
- Determine how to evaluate mixing time and pumping number from simulation results.

1.3 Delimitations

The following delimitations have been set:

- One geometry of impeller and tank as well as one liquid level are used for all simulations and physical tests. 4 different rotational speeds are tested.
- The liquid surface is fixed, hence no vortex formation will be captured.
- The physical tests are only performed 2-3 times for each of the four rotational speeds. Since a relatively large distribution of results is achieved in these kinds of tests, the statistical basis used in this study is limited.
- The mixing process is evaluated by mixing saline into water.
- The mixed liquids are modelled with an assumption of constant density and viscosity.
- Due to computational limitations, the LES simulations make use of wall functions instead of resolving the whole boundary layer, which results in a less accurate solution than using a pure LES.

1.4 Report Structure

The structure of this report is as follows. In Chapter 2, theory regarding CFD simulations and mixing with impellers relevant for this master's thesis is given. Chapter 3 describes the physical testing and its results in terms of mixing time and pumping number. The simulation procedure is outlined in Chapter 4, by first presenting the steps in the creation of the computational domain, mesh and start-up of the simulations, then how the tracer is introduced and how some variables are evaluated. The chapter continues with defining model specific settings for the RANS and LES simulations respectively. Chapter 4 finishes by describing the existing simulation method that has been previously used at FS Dynamics. In Chapter 5, mesh sensitivity studies for both RANS and LES simulations are presented, together with the final meshes used in the rest of the simulations. The results from the validation study are given in Chapter 6. This includes comparisons of the mixing process, mixing times, power number and pumping number as well as the computational requirements. Chapter 7 starts by presenting and discussing the results from simulations with different tracer placements and tracer volumes, followed by an investigation of the influence of Schmidt number and viscosity. The chapter then finishes by discussing how the mixing time and pumping number should be evaluated from a CFD simulation, in terms of defining fully mixed conditions for the mixing time and how to define the impeller swept area for the Metenova ZG5 Magnetic Mixer for the pumping number. Finally, in Chapter 8 the conclusions from this master's thesis are given together with some recommendations for future work.

2 Theory

Theory regarding computational fluid dynamics is introduced in this chapter. Firstly the Finite Volume Method is introduced, followed by the turbulence models used in this study and some basic theory regarding boundary layer flow. The chapter then finishes by presenting some basic theory regarding CFD simulations of mixing with impellers, which includes information about the Metenova ZG5 Magnetic Mixer, modelling of rotation and how to calculate some important impeller performance numbers.

2.1 Computational Fluid Dynamics

A fluid flow is governed by three conservation equations: conservation of mass (the continuity equation), conservation of momentum and conservation of energy. For a closed system without any heat source, only the continuity and momentum equations need to be solved. The continuity equation reads

$$\frac{\partial \rho}{\partial t} + \frac{\partial \rho v_i}{\partial x_i} = 0, \quad (2.1)$$

where t is the time, x_i is the location in i -direction, ρ is the density of the fluid and v_i is the velocity in the i -direction. The momentum equation is defined as

$$\frac{\partial \rho v_i}{\partial t} + \frac{\partial \rho v_j v_i}{\partial x_j} = -\frac{\partial p}{\partial x_i} + \frac{\partial T_{ij}}{\partial x_j} + f_i, \quad (2.2)$$

where p is the pressure, T_{ij} is the viscous stress tensor and f_i are the body forces. The viscous stress tensor is given by

$$T_{ij} = 2\mu s_{ij} - \frac{2}{3}\mu \frac{\partial v_k}{\partial x_k} \delta_{ij}, \quad (2.3)$$

where μ is the dynamic viscosity, δ is the Kronecker's delta and $s_{ij} = \frac{1}{2} \left(\frac{\partial v_i}{\partial x_j} + \frac{\partial v_j}{\partial x_i} \right)$ is the strain rate tensor. [6]

2.1.1 Finite Volume Method

In a CFD-code, the most common way to solve the governing equations is to use the Finite Volume Method (FVM). FVM is a numerical method that transforms transport equations into a system of algebraic equations. A general transport equation for a variable ϕ is formulated as:

$$\underbrace{\frac{\partial(\rho\phi)}{\partial t}}_{\text{Accumulation}} + \underbrace{\frac{\partial(\rho\phi v_j)}{\partial x_j}}_{\text{Convection}} = \underbrace{\frac{\partial}{\partial x_j} \left(\Gamma \frac{\partial \phi}{\partial x_j} \right)}_{\text{Diffusion}} + \underbrace{S_\phi}_{\text{Source term}}, \quad (2.4)$$

where ρ is the density and Γ is the diffusion coefficient. The FVM is based on three steps:

1. The transport equations are integrated over a control volume and a time step. Gauss theorem is used to rewrite volume integrals to surface integrals $\left(\int_V \frac{\partial}{\partial x_j} (\alpha_j) dV = \int_A \alpha_j n_j dA \right)$. The integrated general transport equation can then be written as

$$\begin{aligned} \int_{CV} \left(\int_t^{t+\Delta t} \frac{\partial}{\partial t} (\rho\phi) dt \right) dV + \int_t^{t+\Delta t} \left(\int_A (\rho v_j \phi) n_j dA \right) dt = \\ = \int_t^{t+\Delta t} \left(\int_A \left(\Gamma \frac{\partial \phi}{\partial x_j} \right) n_j dA \right) dt + \int_t^{t+\Delta t} \int_{CV} S_\phi dV dt. \end{aligned} \quad (2.5)$$

2. The integrals are discretized into a linear system of algebraic equations ($Ax = b$). The discretization is done by using a discretization scheme. There are several different schemes to choose among with different accuracy, numerical stability and computational demand. The schemes used in this study are presented below.
3. The algebraic equations are solved using an iterative method. [22]

Discretization Schemes

Four different discretization schemes have been used in this project, two for spatial discretization and two for temporal discretization. The schemes used for spatial discretization are the second order upwind and the Bounded-Central. In the second order upwind scheme, the two first nodes upstream from the face are used to calculate the face value. This is done by assuming that the derivative between two nodes upwind is the same as the derivative between the face and the first node upwind [22]. The second order upwind scheme is second order accurate and does not have the same problems with numerical diffusion as the first order upwind scheme, but it is more unstable. The Bounded-Central scheme is based on the central differencing scheme but applies a boundedness criterion to make it more robust [18]. When the boundedness criterion is not satisfied the scheme turns into a first order upwind scheme, which is more stable than the central differencing scheme. The first order upwind uses the first node upwind to calculate the face value, whereas the central differencing scheme uses the two neighbouring nodes to calculate the face value [22]. The Bounded-Central scheme is a suitable scheme to use for LES simulations of complex turbulent flows, since it provides a good compromise of accuracy and robustness [18].

For temporal discretization, the first and second order implicit schemes have been used. The first order scheme uses the solutions at the current and one previous time step [18]. This scheme is first order accurate and robust so that relatively large time steps can be used without getting convergence issues. The second order scheme is second order accurate and uses the solutions at the current and two previous time steps [18]. This scheme usually requires a smaller time step than the first order, since it is less stable.

Courant–Friedrichs–Lewy Number

When using FVM, the choice of time step size depends on the mesh. The Courant–Friedrichs–Lewy (CFL) number defines how far information travels during one time step. The CFL number is given by

$$CFL = \max \left(v_1 \frac{\Delta t}{\Delta x_1}, v_2 \frac{\Delta t}{\Delta x_2}, v_3 \frac{\Delta t}{\Delta x_3} \right), \quad (2.6)$$

where Δt is the size of the time step and Δx_i the length of the cell in direction i . The CFL number is an important parameter for both stability and accuracy. The requirement of CFL number depends on the used model, for example it is desirable to have a CFL number below 1 for an LES simulation. [1]

2.1.2 Reynolds-Averaged Navier Stokes Equations

When the flow is turbulent, it is often convenient to decompose the quantities into one time-averaged part and one fluctuating part as

$$\Phi = \langle \Phi \rangle + \Phi'. \quad (2.7)$$

For turbulent flow, the governing equations can be time-averaged so that the continuity and momentum equations with constant temperature, with some terms neglected, become

$$\frac{\partial \langle \rho \rangle}{\partial t} + \frac{\partial \langle \rho \rangle \langle v_i \rangle}{\partial x_i} = 0, \quad (2.8)$$

$$\frac{\partial \langle \rho \rangle \langle v_i \rangle}{\partial t} + \frac{\partial}{\partial x_j} (\langle \rho \rangle \langle v_i \rangle \langle v_j \rangle) = -\frac{\partial \langle p \rangle}{\partial x_i} + \frac{\partial \langle T_{ij} \rangle}{\partial x_j} - \frac{\partial \langle \rho \rangle \tau_{ij}}{\partial x_j} + f_i, \quad (2.9)$$

where $\langle \rho \rangle$ is the time-averaged density of the fluid, $\langle v_i \rangle$ is the time-averaged velocity in i -direction, $\langle p \rangle$ is the time-averaged pressure, $\langle T_{ij} \rangle$ is the time-averaged viscous stress tensor and f_i are the body forces ($= \langle \rho \rangle g_i$ if only accounting for gravity, where g_i is the gravity in direction i). τ_{ij} is called Reynolds stress tensor and is written as

$$\tau_{ij} = \langle v'_i v'_j \rangle \quad (2.10)$$

(sometimes defined as $\tau_{ij} = \langle \rho \rangle \langle v'_i v'_j \rangle$), where v' is the fluctuating velocity. The Reynolds stress tensor is an unknown quantity that needs modelling in order to close the RANS equations. [6]

Boussinesq assumption

A common way to model the Reynolds stress tensor is to use the Boussinesq assumption,

$$\langle \rho \rangle \langle v'_i v'_j \rangle = -2\mu_t \langle s_{ij} \rangle + \frac{2}{3} \langle \rho \rangle \delta_{ij} k, \quad (2.11)$$

where $\langle s_{ij} \rangle = \frac{1}{2} (\langle \frac{\partial v_i}{\partial x_j} \rangle + \langle \frac{\partial v_j}{\partial x_i} \rangle)$ is the strain rate tensor, $k = \frac{1}{2} \langle v'_i v'_i \rangle$ is the turbulent kinetic energy and μ_t is the turbulent dynamic viscosity. For the standard k- ε model, the turbulent dynamic viscosity is modelled according to

$$\mu_t = c_\mu \langle \rho \rangle \frac{k^2}{\varepsilon}, \quad (2.12)$$

where ε is the turbulent dissipation rate and c_μ is a constant taken as 0.09.

Realizable k- ε Model

The realizable k- ε model is used for the RANS simulations in this project. In many cases, the realizable k- ε model has proven to be substantially better than the standard k- ε model. In general, it is at least as accurate as the standard model. A different transport equation for ε is solved and a damping function is added when calculating the turbulent viscosity, which is expressed as a function of the mean velocity and turbulence properties. Furthermore, it fulfills some realizability constraints which means that some unphysical phenomena, such as negative normal stresses, are circumvented. [18]

In the realizable k- ε model, the modelled transport equations for turbulent kinetic energy and turbulent dissipation rate are solved using the Boussinesq assumption with an added damping function. Hence, the turbulent viscosity is written as

$$\mu_t = c_\mu \langle \rho \rangle f_\mu \frac{k^2}{\varepsilon}. \quad (2.13)$$

f_μ is the damping function defined as

$$f_\mu = \frac{1}{c_\mu \left(4 + \sqrt{6} \cos \left(\frac{1}{3} \cos^{-1} \left(\sqrt{6} \frac{\langle s_{ij}^* \rangle^3}{\sqrt{\langle s_{ij}^* \rangle \langle s_{ij}^* \rangle^3}} \right) \right) \frac{k}{\varepsilon} \sqrt{\langle s_{ij} \rangle \langle s_{ij} \rangle + \langle \Omega_{ij} \rangle \langle \Omega_{ij} \rangle} \right)}, \quad (2.14)$$

where $\langle \Omega_{ij} \rangle = \frac{1}{2} (\langle \frac{\partial v_i}{\partial x_j} \rangle - \langle \frac{\partial v_j}{\partial x_i} \rangle)$ is the vorticity tensor and $\langle s_{ij}^* \rangle = \langle s_{ij} \rangle - \frac{1}{3} \langle \delta_{ij} s_{kk} \rangle$.

The modelled k-equation for constant temperature is

$$\frac{\partial(\langle \rho \rangle k)}{\partial t} + \frac{\partial(\langle \rho \rangle k \langle v_j \rangle)}{\partial x_j} = P^k - \langle \rho \rangle \varepsilon + \frac{\partial}{\partial x_j} \left[\left(\langle \mu \rangle + \frac{\mu_t}{\sigma_k} \right) \frac{\partial k}{\partial x_j} \right] + S^k, \quad (2.15)$$

where S^k is a source term and $\sigma_k = 1$ is a turbulent Prandtl number. P^k is the production term taken as

$$P^k = f_c G^k + \gamma_M, \quad (2.16)$$

where f_c is a curvature correction factor,

$$f_c = \min \left(C_{max}, \frac{1}{C_{r1} (|\eta| \eta) + \sqrt{1 - \min(C_{r2}, 0.99)}} \right). \quad (2.17)$$

$$\eta = T^2 (\langle s_{ij} \rangle \langle s_{ij} \rangle - \langle \Omega_{ij} \rangle \langle \Omega_{ij} \rangle), \quad (2.18)$$

where T is the timescale limited to $T = \max(T_1, T_3) = \max \left(\frac{\varepsilon}{k}, (T_1^{1.625} T_2)^{\frac{1}{1.625+1}} \right)$, $T_2 = 6\sqrt{\frac{\nu}{\varepsilon}}$ and C_{max} , C_{r1} , C_{r2} are model coefficients taken as (1.25, 0.04645, 0.25). The turbulent production, G^k is taken as

$$G^k = \mu_t \left(\frac{\partial \langle v_i \rangle}{\partial x_j} + \frac{\partial \langle v_j \rangle}{\partial x_i} \right) \frac{\partial \langle v_i \rangle}{\partial x_j} - \frac{2}{3} \langle \rho \rangle k \frac{\partial \langle v_i \rangle}{\partial x_i} - \frac{2}{3} \mu_t \left(\frac{\partial \langle v_i \rangle}{\partial x_i} \right)^2, \quad (2.19)$$

and the compressibility modification, γ_M , as

$$\gamma_M = \frac{C_M k \varepsilon}{c^2}, \quad (2.20)$$

where $C_M = 2$ is a model coefficient and c is the speed of sound.

The modelled ε -equation is

$$\frac{\partial(\langle \rho \rangle \varepsilon)}{\partial t} + \frac{\partial(\langle \rho \rangle \varepsilon \langle v_j \rangle)}{\partial x_j} = \frac{\varepsilon}{k} c_{\varepsilon 1} P_\varepsilon - c_{\varepsilon 2} f_2 \langle \rho \rangle \frac{\varepsilon^2}{k} \frac{\partial}{\partial x_j} \left[\left(\langle \mu \rangle + \frac{\mu_t}{\sigma_\varepsilon} \right) \frac{\partial \varepsilon}{\partial x_j} \right] + S_\varepsilon, \quad (2.21)$$

where S_ε is a source term, $c_{\varepsilon 1}$, $c_{\varepsilon 2}$, σ_ε are model coefficients taken as $(1.2, 1, \max(0.43, (\frac{|s|k/\varepsilon}{5+|s|k/\varepsilon})))$, 1.9) and f_2 is a damping function defined as

$$f_2 = \frac{k}{k + \sqrt{\nu \varepsilon}}, \quad (2.22)$$

where ν is the kinematic viscosity. P_ε is the production term defined as

$$P_\varepsilon = f_c |s| k, \quad (2.23)$$

where $|s|$ is the norm of the strain rate tensor $\langle s_{ij} \rangle$. [18]

Two-layer Model

One disadvantage of the k- ε models is that they do not predict the near-wall flow well [6]. Hence, wall functions should be used and the y^+ value of the first cell should be in the log-law regime. By using a two-layer approach, the k- ε model can be used in the viscous regime as well, which means that the model can account for both low and high y^+ values. The calculation regime is divided into two layers, one near the wall and one in the rest of the domain. Near the wall, ε and μ_t are prescribed algebraically depending on the distance to the wall. The values of ε near the wall are blended smoothly with the values calculated from the ε transport equation further away from the wall. The usual transport equation for k is solved in the whole domain. The results from using the two-layer model is often as good or better than those obtained using damping functions near the walls. [18]

In the near-wall region, the dissipation rate is computed as

$$\varepsilon = \frac{k^{3/2}}{l_\varepsilon}, \quad (2.24)$$

where l_ε is a length scale function. According to the model variant proposed by Wolfstein[23]

$$l_\varepsilon = c_l d \left[1 - \exp\left(-\frac{Re_d}{2c_l}\right) \right], \quad (2.25)$$

where $c_l = 0.42c_\mu^{-3/4}$, d is the distance to the wall and $Re_d = \frac{\sqrt{k}d}{\nu}$ is the wall distance Reynolds number.

The two-layer model is combined with the full two-equation model by blending the turbulent viscosity from the k- ε model, $\mu_t|_{k-\varepsilon}$,

$$\mu_t = \lambda \mu_t|_{k-\varepsilon} + (1 - \lambda) \langle \mu \rangle \left(\frac{\mu_t}{\langle \mu \rangle} \right)_{2layer}, \quad (2.26)$$

$$\left(\frac{\mu_t}{\langle \mu \rangle} \right)_{2layer} = 0.42 Re_d c_\mu^{1/4} \left[1 - \exp\left(-\frac{Re_d}{70}\right) \right], \quad (2.27)$$

$$\lambda = \frac{1}{2} \left[1 + \tanh\left(\frac{Re_d - Re_y^*}{A}\right) \right], \quad (2.28)$$

where $Re_y^* = 60$ is a model coefficient that defines the limit of applicability of the two-layer formulation and $A = \frac{|\Delta Re_y|}{\text{atanh}(0.98)}$, $|\Delta Re_y| = 10$ [18].

2.1.3 Large Eddy Simulation

LES is a transient method where most of the turbulence is resolved and only the smallest isotropic turbulence is modelled. The resolved scales are called grid scales (GS) and the modelled scales subgrid scales (SGS). LES is based on the continuity and momentum equations, but instead of time averaging as in the RANS equations they are spatially averaged. Spatial averaging can also be called filtering and a variable could be decomposed as

$$\Phi = \bar{\Phi} + \Phi'', \quad (2.29)$$

where $\bar{\Phi}$ is the filtered part and Φ'' is the fluctuating. The governing equations for LES can therefore be expressed, with some terms neglected, as

$$\frac{\partial \bar{\rho}}{\partial t} + \frac{\partial(\bar{\rho} \bar{v}_i)}{\partial x_i} = 0, \quad (2.30)$$

$$\frac{\partial(\bar{\rho} \bar{v}_i)}{\partial t} + \frac{\partial}{\partial x_j}(\bar{\rho} \bar{v}_i \bar{v}_j) = -\frac{\partial \bar{p}}{\partial x_i} + \frac{\partial \bar{T}_{ij}}{\partial x_j} - \frac{\partial \bar{\rho} \tau_{ij}}{\partial x_j} + f_i, \quad (2.31)$$

where \bar{v} is the filtered velocity, \bar{p} is the filtered pressure, $\bar{\rho}$ is the filtered density, \bar{T}_{ij} is the filtered viscous stress tensor, f_i is the body forces and τ_{ij} are the subgrid stresses. The subgrid stresses are given by

$$\tau_{ij} = (\bar{v}_i \bar{v}_j - \bar{v}_i \bar{v}_j), \quad (2.32)$$

and needs modelling in order to close the LES equations. [6]

Since LES can resolve much of the turbulence it is more accurate than a RANS simulation where all the turbulence is modelled, but it is also more computationally demanding. [6]

Smagorinsky Model

The simplest way to model the subgrid stresses is to use the Smagorinsky model which makes use of Boussinesq assumption,

$$\bar{\rho}(\bar{v}_i \bar{v}_j - \bar{v}_i \bar{v}_j) = -2\mu_{sgs} \bar{s}_{ij} + \frac{2}{3} \bar{\rho} \delta_{ij} k_{sgs}, \quad (2.33)$$

where k_{sgs} is the subgrid turbulent kinetic energy. The subgrid turbulent dynamic viscosity, μ_{sgs} , is given by

$$\mu_{sgs} = (C_S \Delta)^2 \bar{\rho} |\bar{s}|, \quad (2.34)$$

where $\Delta = V_c^{1/3}$ is the filter width taken from the local grid size, $|\bar{s}|$ is the norm of the strain rate tensor \bar{s}_{ij} and the value of the constant C_S is taken as 0.1 [6],[18]. One of the limitations of the Smagorinsky model is that C_S is taken as a constant, even though it is actually depending on the flow conditions and grid size [2].

Dynamic Smagorinsky Model

The dynamic Smagorinsky model is used for the LES simulations in this project. In this model, the subgrid viscosity is taken from the standard Smagorinsky model (Equation (2.34)), but with C_S computed dynamically from test filtered variables. C_S then becomes a local time-varying coefficient depending on the flow conditions. This gives better predictions of, for example, wall bounded flows without having to use damping functions. [18]

A test filtered value in a cell using a grid of twice the size of the computational grid is defined as

$$\hat{\Phi} = \frac{1}{\sum_{n=0}^N V_n} \sum_{n=1}^N \bar{\Phi}_n V_n, \quad (2.35)$$

where V_n is the cell volume, $\hat{\cdot}$ denotes a test filtered value, subscript n denotes cell number, cell 0 is the current cell and cells 1-N are face neighbours of cell 0. The subgrid stresses on grid level, test level and intermediate level (Leonard stresses) are defined as

$$\tau_{ij} = \bar{v}_i \bar{v}_j - \bar{v}_i \bar{v}_j, \quad (2.36)$$

$$\tau_{ij,test} = \widehat{v_i v_j} - \widehat{v_i} \widehat{v_j}, \quad (2.37)$$

$$\mathcal{L}_{ij} = \tau_{ij,test} - \widehat{\tau}_{ij} = \widehat{v_i v_j} - \widehat{v_i} \widehat{v_j}. \quad (2.38)$$

C_S is calculated from

$$C_S = -\frac{1}{2} \frac{\mathcal{L}_{ij} M_{ij}}{M_{ij} M_{ij}}, \quad (2.39)$$

with M_{ij} defined as

$$M_{ij} = \widehat{\Delta^2 |\widehat{s}| \widehat{s}_{ij}} - \Delta^2 \widehat{|\widehat{s}| \widehat{s}_{ij}}. \quad (2.40)$$

To enhance stability, C_S is often spatially averaged, preferably in a homogeneous direction (if such is present) [6],[18]. Furthermore, C_S is limited to a minimum value of 0 and a maximum value of 1 000 000 in STAR-CCM+ [18].

2.1.4 Transport of Species in a Mixture

To simulate the transport of different species in a mixture of liquids, a transport equation for the mass fraction for each species is solved. The transport equation is defined as

$$\frac{\partial(\rho Y_s)}{\partial t} + \frac{\partial(\rho Y_s v_j)}{\partial x_j} = \frac{\partial}{\partial x_j} \left(\left(\rho D_{s,m} + \frac{\mu_t}{\sigma_t} \right) \frac{\partial Y_s}{\partial x_j} \right) + S_{Y_s}, \quad (2.41)$$

where ρ is the overall density, Y_s is the mass fraction of species s , $D_{s,m}$ is the molecular diffusivity of species s , μ_t is the turbulent dynamic viscosity, σ_t is the turbulent Schmidt number and S_{Y_s} is a source term. The molecular diffusivity is calculated as

$$D_{s,m} = \frac{\nu}{Sc_s}, \quad (2.42)$$

where Sc_s is the Schmidt number and ν is the kinematic viscosity.

For the material properties of the mixture, a mass-weighted method is used in this project. A mixture property is then calculated as

$$\phi_{mix} = \sum_{s=1}^N Y_s \phi_s, \quad (2.43)$$

where ϕ is a material property and subscript s denotes the different components. [18]

2.1.5 Boundary Layer Flow

The relative velocity between a fluid and a solid wall is zero. The region between the wall and the free-stream flow is called boundary layer. A boundary layer can be either laminar or turbulent, depending on the Reynolds number. For turbulent boundary layers, a boundary layer of thickness δ can be divided into two regions:

- **Inner region:** $0 < y < 0.2\delta$
- **Outer region:** $0.2\delta < y < \delta$

To characterize certain regimes in the inner region of the boundary layer, non-dimensional parameters y^+ and u^+ are often used for wall distance and velocity. These are defined as

$$y^+ = \frac{y u^*}{\nu}, \quad (2.44)$$

$$u^+ = \frac{u}{u^*}, \quad (2.45)$$

where y is the normal distance from the wall-cell centroid to the wall, ν is the kinematic viscosity and u is the component of the wall-cell velocity parallel to the wall. $u^* = \sqrt{\tau_w/\rho}$ is the frictional velocity where τ_w is the wall shear stress and ρ is the density of the fluid [2]. The inner region of the boundary layer has the same characteristics for all turbulent boundary layers when described in terms of y^+ and u^+ . It can be divided into the following three subregions:

- **Viscous sublayer**, $0 < y^+ < 5$: dominated by viscous effects and is almost completely laminar. Linear relationship between u^+ and y^+ .
- **Log-law region**, $30 < y^+ < 500$: dominated by both viscous and turbulent effects. Logarithmic relationship between u^+ and y^+ .
- **Buffer layer**, $5 < y^+ < 30$: transitional region between the viscous sublayer and the log-law region.

In CFD-codes, wall functions are often used to account for the effects of the near-wall flows when it is too computationally expensive to resolve the whole boundary layer or when a turbulence model which does not perform well near the wall is used. There are three different wall treatments available in STAR-CCM+: low y^+ , high y^+ and all y^+ wall treatment. The low y^+ wall treatment resolves the whole boundary layer, including the viscous sublayer, and needs a y^+ value around 1 to be accurate. High y^+ wall treatment does not resolve the viscous sublayer and uses wall functions to obtain the boundary conditions needed in the governing equations. The wall shear stress, turbulent production and turbulent dissipation are derived from the equilibrium turbulent boundary layer theory. The centroid of the first cell needs to be located inside the log-law region ($y^+ > 30$) to get a good solution when using this wall treatment. The all y^+ wall treatment is a hybrid approach that acts as the low y^+ wall treatment for fine meshes and as high y^+ wall treatment for coarser meshes. It also gives reasonable results for y^+ values located in the buffer region, where it uses a blending function for calculating turbulence quantities. For this project, the all y^+ wall treatment is used. However, the value of y^+ is not the only important parameter when creating the boundary layer mesh. It is also necessary to have enough cells in the whole boundary layer to capture the flow accurately. [18]

2.2 Mixing with Impellers

Impellers are used to mix liquids, gases and particles in tanks. There are different types of impellers and the two main categories are radial and axial impellers. A radial impeller gives, as the name indicates, a radial flow out from the impeller, while an axial creates an axial flow. If the impeller is placed in the center of the tank, baffles are often used on the tank walls to prevent swirling. Baffles are long plates placed vertically on the tank walls, which will cause the flow to move in vertical direction as well. Evaluation of an impeller and tank configuration often includes looking at parameters such as the power number, pumping number and mixing time.

2.2.1 Metenova ZG5 Magnetic Mixer

The ZG5 magnetic mixer from Metenova, seen in Figure 2.1, has a diameter of 148 mm. It uses magnetic drives and is mounted at the bottom of the tank. The stationary part of the impeller is welded into the bottom of the tank, and the rotational part is placed on top of it inside the tank. The rotation of the impeller is driven by a magnetic coupling between the external rotating drive source and the internal impeller. Since the mixer is placed at the bottom of the tank, it is easier to keep the tank completely sterile which is important in the pharmaceutical industry. The mixer is placed at an offset from the middle, and therefore there is no need for baffles in the tank. [12]



Figure 2.1: *Metenova ZG5 Magnetic Mixer.*

2.2.2 Moving Reference Frame

The MRF approach is commonly used when performing CFD simulations of active mixing applications. The mesh is divided into two or more regions. A rotating reference frame is applied to the mesh region containing the impeller, while a stationary reference frame is used for the rest of the domain. The impeller rotates at the same speed as the rotating reference frame, which means that no mesh motion is needed [12]. The Coriolis force and centrifugal forces are added to the momentum equations in the rotating region [5]. Since there are no real motions during the simulation, the solution can be interpreted as a snapshot of the flow with the impeller at a specific location. The MRF method assumes a weak interaction between the rotating region and the surrounding, stationary region [19]. Since there is no mesh motion, the transient flow effects due to the position change of a rotating impeller are neglected [18].

2.2.3 Sliding Mesh

SM is a method used in transient simulations to simulate the real motion. The basic idea is to move the mesh together with the moving part. The approach when using sliding mesh in mixing is to move the grid around the impeller along with the impeller as it rotates. This is implemented by creating a rotationally symmetrical zone around the impeller, and then rotate the whole zone together with the impeller. The boundaries of the SM zone then "slides" along the mesh of the stationary region.

At every time step, the SM zone moves a step and the equations are solved. The motion is therefore not continuous. At each iteration, information is passed back and forth at the interface between the SM zone and the rest of the tank. For this to work, the interface must consist of two superimposed surfaces. Since the cells at the interface will not line up exactly at most time steps, the information passed back and forth is interpolated. [12]

2.2.4 Impeller Reynolds Number

The Reynolds number is a non-dimensional quantity which is commonly used in fluid mechanics. It is defined as a ratio of the inertial forces to the viscous forces. Therefore, it is often used to judge if the flow is turbulent or laminar, since a turbulent flow is governed more by inertial forces and laminar flow by viscous forces. For an impeller, the Reynolds number is given by

$$Re = \frac{\rho ND^2}{\mu}, \quad (2.46)$$

where ρ is the density of the fluid, N is the rotational speed in rounds per second, D is the diameter of the impeller and μ is the dynamic viscosity. For mixing in tanks, the transition between laminar and turbulent regime usually occurs somewhere in the range of $Re = 50$ to $Re = 5000$. [12]

2.2.5 Power Number

Power number is a non-dimensional number used for calculating shaft power and it is unique for each type of impeller. It is also a function of the Reynolds number, but at fully turbulent flow the power number is assumed to be constant [8]. The power number is calculated as

$$P_0 = \frac{P}{\rho N^3 D^5}, \quad (2.47)$$

where P is the shaft power, D is the diameter of the impeller, N is the rotational speed of the impeller and ρ is the density of the fluid. The shaft power can be calculated from

$$P = 2\pi NT_Q, \quad (2.48)$$

where T_Q is the impeller torque. [12]

2.2.6 Pumping Number

Pumping number (also called Flow number) is a non-dimensional measure of the impellers pumping capacity. It is calculated as

$$N_Q = \frac{Q_p}{ND^3}, \quad (2.49)$$

where N is the rotational speed of the impeller, D the impeller diameter and Q_p is the volumetric flow rate leaving the discharge side of the impeller. The volumetric flow rate is calculated by performing an area integration of the normal velocity over the impeller swept area. There are two ways of defining the impeller swept area depending on if the impeller is a radial or axial impeller. For an axial impeller, which creates an axial flow through the impeller, the area is a circular plane with the diameter D . For a radial flow impeller, a cylinder around the impeller with radius D and the same height as the impeller is used as the impeller swept area. [12]

2.2.7 Mixing Time Definition

The mixing time is defined as the time it takes to get to a certain homogeneity of, for example, concentration of species in the tank. The homogeneity is often taken as 95% and the time corresponding to this is denoted as τ_{95} . The mixing time can be measured both locally and globally. A local mixing time is evaluated from measurements at a specific point in the tank. The concentration at the point is tracked, and the time it takes for the concentration reach a value between $0.95 \cdot \bar{c}_t$ and $1.05 \cdot \bar{c}_t$, where \bar{c}_t denotes the average concentration in the tank, gives τ_{95} . It should be noted that different points often gives different mixing times, even though they are measured during the same test [15]. Hence, if 95% mixing is reached at one location, it does not necessary mean that the tank is fully mixed. This method can be used by inserting a probe in the tank, for example a conductivity meter. However, using a probe is an intrusive method where the presence of the probe affects the flow [3],[12].

There are several ways of measuring the global mixing time. One way is to track the maximum and minimum concentrations in the tank. τ_{95} is then taken as the time it takes for both the minimum point to reach above $0.95 \cdot \bar{c}_t$ and for the maximum to reach below $1.05 \cdot \bar{c}_t$. This method was first proposed by Yeoh et al.[24], but have also been used by Li and Xu[15].

Another way to measure the global mixing time is to use the Coefficient of Variance (CV) of the concentration in the tank. The CV is the standard deviation of the concentration normalized with the average concentration in the tank. For a CFD simulation with varying cell sizes, the CV is computed as

$$CV = \frac{1}{\bar{c}_t} \frac{\sqrt{\sum (c - \bar{c}_t)^2 V_c}}{\sqrt{\sum V_c}}, \quad (2.50)$$

where c is the concentration in the cell and V_c is the volume of the cell. Kukukova et al.[13] defines 95% mixing from $CV = 0.05$, while Hartmann et al.[11] have by means of a numerical experiment determined that 95% mixing occurs at $CV = 0.0283$ in their study of a Rushton turbine agitated tank (also used by Haringa et al.[9], Li and Xu[15]). The numerical experiments performed by Hartmann et al.[11] consisted of taking 32 statistically independent values between 0.95 and 1.05 and then calculating the CV . This was then repeated several times with new sets of statistically independent values. The calculated CV 's were then averaged, which gave the value of 0.0283.

3 Physical Testing

Physical testing was performed to get validation data for both the RANS and LES simulations. The tests were performed at Metenova’s test lab using their equipment. The experiments were conducted using a 300 litre tank, with a diameter of 670 mm, and the Metenova ZG5 Magnetic Mixer placed in the bottom of the tank. The tank was filled with water at 22°C, same as the room temperature, to a height of 670 mm. Tests were performed at four different rotational speeds, 105, 135, 170 and 210 rpm. This height and these speeds were chosen based on the desire to have fully turbulent flow while not having a vortex formation, which is a common phenomena in mixing with impellers.

3.1 Mixing Time using Conductivity Meters

For each test saline was added after the flow was fully developed, which was when the effects of the start-up of the rotation were considered to be negligible. The saline was created from adding 1 kg of NaCl to 3 litre of water (resulting in a solution with approximately 25% mass concentration of salt). The saline was poured into the tank from a height of around 0.1 m above the water surface during approximately 6 s. This was done at a location above the impeller, as indicated in Figure 3.1. Conductivity was measured at two points, denoted as the Conductivity Points (CP) seen in Figure 3.1, using probes until the fluid was completely mixed. The measurement points are located a few centimeters from the tank walls, since it was not possible to place them further away from the walls without using different equipment. The probes were mounted from above, making CP1 the lowest reachable point.

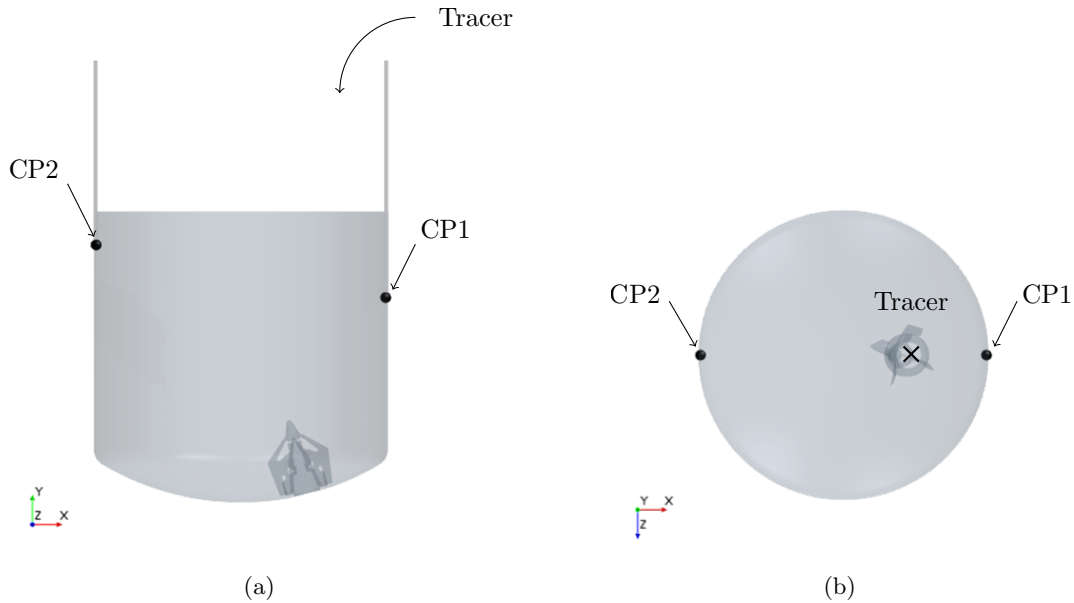


Figure 3.1: Placement of the conductivity points and location where the tracer was added, displayed in a view from (a) the side and (b) the top.

The conductivity probes were of model Hanna Instruments HI8733, which is a four electrode probe, see Figure 3.2. The probes work by measuring the conductivity on the small volume of liquid located inside the cover. There is an opening in the bottom part and four small holes in the middle part of the cover which allows the fluid to flow into the probe to where the conductivity is measured. The probes were placed horizontally with the bottom aligned against the flow, to allow the fluid to flow into the bottom opening and out through the small holes.

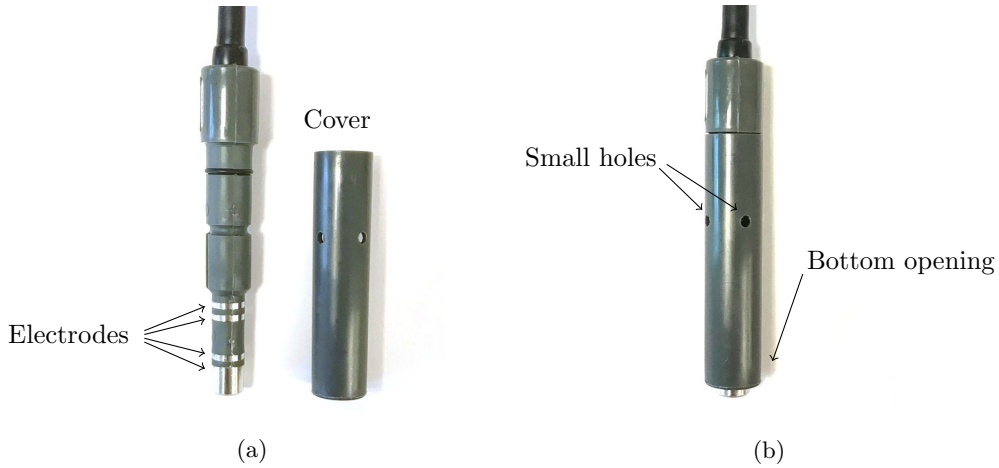


Figure 3.2: Conductivity probe used in the physical testing (a) without cover and (b) with cover.

9 tests were performed in total, 3 at 105 rpm and 2 for each of the other rotational speeds. Curves of the conductivity at the measurement points versus time were plotted. The conductivity curves for CP1 at 105 rpm are presented in Figure 3.3, for curves of CP2 and the other rotational speeds see Appendix A. The mixing times for 95% mixing, τ_{95} , were evaluated from the time it took for the conductivity to reach within 5% of the mean conductivity in the tank. This corresponds to when the concentration of the saline is between $0.95 \cdot \bar{c}_t$ and $1.05 \cdot \bar{c}_t$. The resulting mixing times from the physical tests are presented in Figure 3.4.

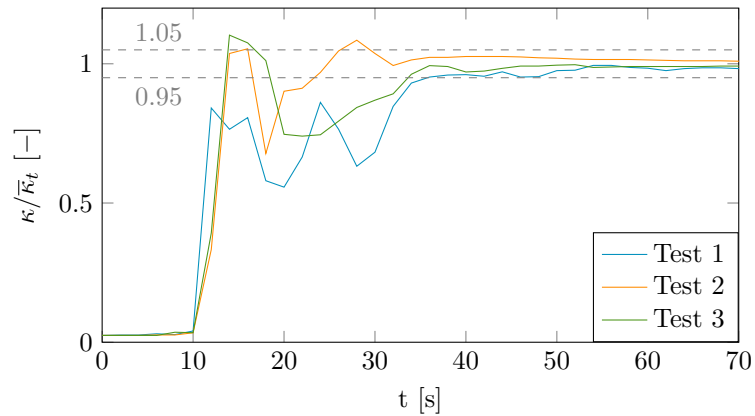


Figure 3.3: Normalized conductivity curves from CP1 at 105 rpm.

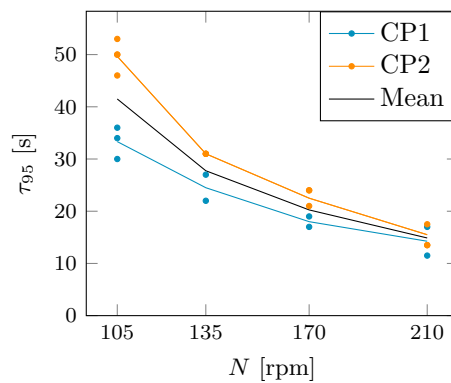


Figure 3.4: Mixing times for the four rotational speeds from the physical testing. Note that one dot corresponds to one performed test. The mean results are presented as lines, where both means of CP1, CP2 and a global mean calculated from the two conductivity points are included.

Tests have also been performed with the probes mounted vertically at the tank wall. This alignment gave results that varied over a large interval and were not in the same range as the results from the simulations and physical tests with horizontal alignment. This indicates that a vertical alignment with this kind of probe is not suitable, since the fluid does not seem to enter the probe correctly. For results from this configuration, see Appendix B.

3.2 Power Number from Experiments

The maximum impeller torque that the impeller can sustain without losing the connection between the stationary and rotational part was measured using a torque wrench to 7.25 Nm. The rotational speed of the impeller was then increased to 630 rpm, where the rotational part of the impeller lost connection to the stationary part. Hence, the previously measured torque was reached at this rotational speed. The power number was then calculated from these measured values, using Equations (2.47) and (2.48), to 5.8.

4 Simulation Procedure

The simulation procedure used in this project is presented in this chapter. At first the general procedure, which applies for both the RANS and LES simulations, is presented. This includes setting up the computational domain and mesh, start-up of the simulations and the introduction of tracer. The methodology for how some of the important parameters were evaluated from the simulation results is given. Settings and other specific information for the RANS and LES simulations are then given separately. The chapter finishes by giving a short description of the existing method that has been previously used at FS Dynamics.

4.1 Computational Domain and Mesh

The geometries used in the simulations consist of the Metenova ZG5 Magnetic Mixer, which has a diameter of 148 mm and is described more comprehensively in Section 2.2.1, and a 300 litre tank with a diameter of 670 mm. The Computer-Aided Design (CAD) model of the impeller and tank geometries, provided by Metenova, was first prepared for CFD simulations in ANSYS SpaceClaim v2018 from ANSYS Inc. The preparation consisted of removing gaps between the rotating and stationary parts of the impeller and repairing other discontinuities in the geometry, which could have caused problem when meshing. A cylindrical region was created which was used to model the rotation of the impeller. It has a diameter of 300 mm, with the central axis of the impeller in the middle, and a height of 200 mm. The computational domain was divided into two regions: the rotational region consisting of the created cylinder with the impeller and the stationary region containing the rest of the domain with the rotational region cut out, these are shown in Figure 4.1.

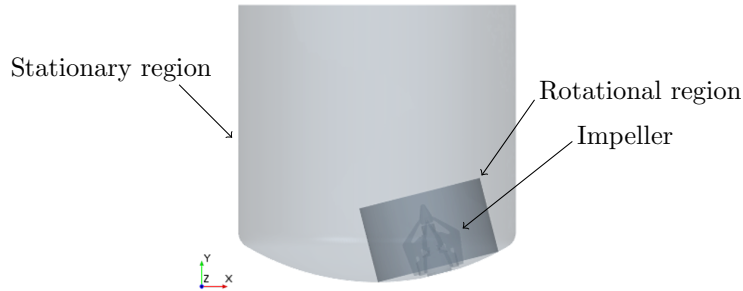


Figure 4.1: *The computational domain, where the rotational region goes all the way down to the tank bottom.*

The boundary conditions for the tank walls, tank bottom and the stationary part of the impeller were specified as stationary walls with a no-slip condition. The top of the tank was set to a wall with a free-slip condition, since it is a free surface. The rotational part of the impeller was set to a rotating wall with a no-slip condition. The rotating and stationary parts of the impeller are designated in Figure 4.2. An interface between the rotational region and the stationary region was created. A rotating motion was set to the whole rotational region. The modelling of the rotation was defined by using an MRF for the RANS simulations and SM for the LES.

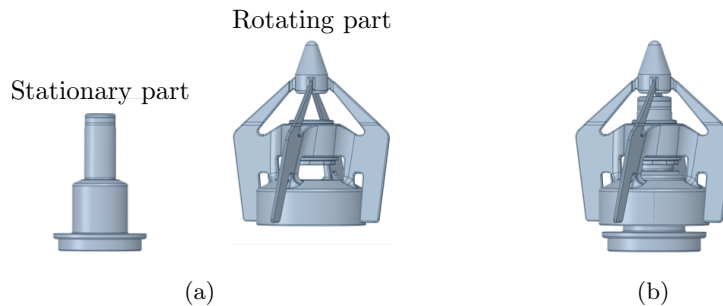


Figure 4.2: *CAD model of (a) the impeller divided into two parts and (b) the whole impeller.*

A polyhedral mesh was created in STAR-CCM+. The mesh density was mainly controlled by setting cell sizes on surfaces of the domain, and then letting the program create a volume mesh with cell sizes that smoothly adapts between the assigned sizes set at the surfaces. Prism layers were used on the boundaries specified as walls (except the top of the tank), where boundary layers were present. Several meshes have been used during this project, more information about these is presented in Sections 5.2 and 5.4.

4.2 Simulation Start-up

To fully develop the flow before adding the tracer, the tank was simulated filled with water to a height of 670 mm, with a constant density of $997,76 \text{ kg/m}^3$ which corresponds to 22°C [17]. Simulations were performed at four rotational speeds according to Table 4.1. The height and speeds were chosen based on the desire to not have a vortex formation in the tank, but still have the flow fully turbulent. The resulting Reynolds numbers indicates that all simulations were performed in the fully turbulent region.

Table 4.1: *Rotational speeds and Reynolds numbers for the performed simulations.*

Rotational speed [rpm]	Reynolds number [-]
105	39 000
135	50 000
170	62 000
210	77 000

4.3 Tracer Introduction

To evaluate the mixing time in the simulations, a tracer was added when the flow was fully developed. For the RANS simulations, a converged steady state solution was used, whereas for LES the flow was considered fully developed when the effects of the start-up of the rotation were assumed negligible. Two different strategies were developed for the introduction of tracer. The first method, denoted as T1, was to replace some of the water inside the tank with the tracer. The other method, denoted as T2, was to mimic the pouring of tracer from the physical tests by creating an inlet at the top boundary of the tank.

Both methods used the "Multi-component liquid" model in STAR-CCM+. Two components were defined, water and tracer. The amount of tracer was approximated to correspond to the same volume as the physical tests. In the experiments, saline created from dissolving 1 kg NaCl in 3 litres of water, was used as the tracer. Taking the density as 1192.4 kg/m^3 [14], which corresponds to 25% mass concentration of salt and the total mass as 1 kg NaCl + 2.991 kg water, the volume of the tracer was calculated to 3.3 litres.

4.3.1 Method T1: Fixed Volume

When using a fixed volume of tracer, 3.3 litres of the water inside the tank was replaced with a tracer. This was done by mapping the fully developed solution containing only water and then initializing a new solution with the mapped velocity, pressure and turbulent quantities. At this initialization step, the tracer was introduced by making use of the Field Functions in STAR-CCM+, where a function was used to describe where in the domain the tracer should be placed.

Using this method, the tracer was simulated with the same properties as water, even though the saline used in the physical tests has a higher density. This simplification was needed since nonphysical velocities appeared if the density was changed.

4.3.2 Method T2: Pouring

To mimic the pouring from the physical tests, an inlet was created at the top of the tank. The inlet has a radius of 11.26 mm and was placed directly over the impeller, in between the center of the tank and the tank

wall. The rest of the tank top was simulated as an outlet of water, to keep the liquid volume constant. This configuration is presented in Figure 4.3.

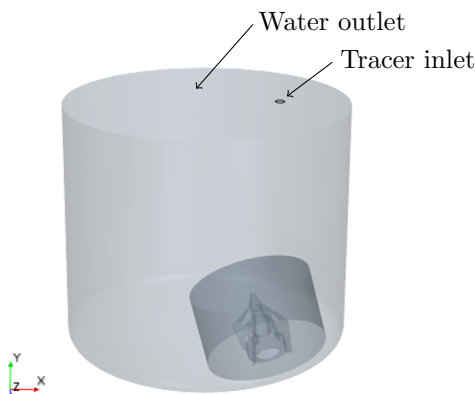


Figure 4.3: *The computational domain with the tracer inlet and water outlet boundaries at the top of the tank.*

The boundary conditions for both the inlet and outlet were set to Velocity inlet. The velocity at the inlet was set to 1.4 m/s, estimated from the physical testing where the saline was poured into the domain at a height of approximately 0.1 m. For the outlet the velocity was -0.00158 m/s, giving a zero net flux of volume into the tank. The boundaries were also specified such that only tracer was added through the inlet and only water was removed at the outlet. The inlet and outlet boundaries were active during 6 s, giving a tracer volume of approximately 3.2 litres. After these 6 s, both the inlet and outlet boundaries were defined as free-slip walls again.

Using this method, it was possible to change the density of the tracer to correspond to the saline used in the physical tests. The saline contained approximately 25% mass concentration of salt, which corresponds to a density of 1192.4 kg/m³[14]. Due to this density change, gravity was added to the governing equations in the solver to account for buoyancy forces.

4.4 Evaluation of Mixing Parameters

For mixing with impellers, it is often of interest to evaluate the mixing time, power number and pumping number of the impeller. Hence, the methods used for evaluating these parameters are presented here.

4.4.1 Mixing Time

The global mixing time was evaluated from the coefficient of variance of the tracer concentration in the tank. According to the theory presented in Section 2.2.7, it is not completely known how to estimate 95% of fully mixed conditions. The results from the simulations in this project apply the limit of Kukukova et al., where 95% mixing is determined from $CV = 0.05$. However, all three methods of evaluating global mixing time described in Section 2.2.7 are further discussed in Section 7.4.

4.4.2 Power Number

The torque at the rotating part of the impeller, coming from both shear stress and pressure, was extracted from the simulation results. The power number was then calculated using Equations (2.47) and (2.48). The evaluation of power number was done before adding the tracer into the simulations, hence the resulting values are based on only water inside the tank. For the RANS simulations, the torque was extracted from the converged steady-state simulations. For the LES, the torque was sampled at each time step and then the time-averaged value was used to calculate the power number.

4.4.3 Pumping Number

The pumping number was calculated with Equation (2.49), using the rotational speed, impeller diameter and the volumetric flow rate leaving the discharge side of the impeller. The volumetric flow rate was calculated from integrating the normal velocity over the impeller swept area. This impeller swept area consists of a cylinder without any top or bottom. The cylinder has a radius of 80 mm and a height of 60 mm, seen in Figure 4.4. More information on how the impeller swept area was chosen is presented in Section 7.5.

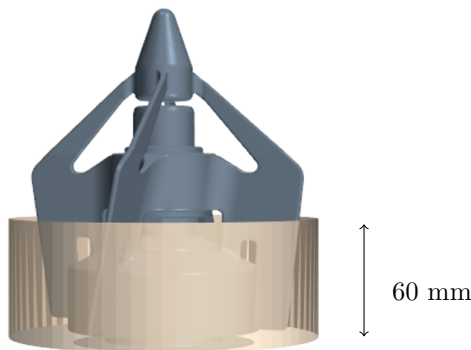


Figure 4.4: *Impeller and the impeller swept area used for calculating pumping number.*

The evaluation of pumping number was, precisely as in the evaluation of power number, performed while having only water inside the tank. Furthermore, the pumping number was extracted from converged steady-state simulations for the RANS simulations, whereas sampled data was time-averaged and used for the LES.

4.5 Reynolds-Averaged Navier Stokes Simulations

The RANS solver was used with the realizable $k-\varepsilon$ two-layer turbulence model. Since a wide range of y^+ values was present due to the complexity of the geometry, the all y^+ wall treatment model was used. All RANS simulations started with a steady-state solution, which was used to evaluate power and pumping number as well as initialization for the transient mixing simulations. Both methods of introducing a tracer have been used in the RANS simulations.

When using a fixed volume of tracer, method T1 explained in Section 4.3.1, the solvers concerning velocities, pressure, turbulent kinetic energy and turbulent dissipation rate were frozen after the steady-state simulation had converged. Hence, only the equations concerning the mixture of the liquid components were solved in the transient simulation. The frozen solvers make this approach the simplest and fastest of all performed simulations. The other method, T2 described in Section 4.3.2, which mimic the pouring of the tracer, was simulated while having all solvers active.

A segregated solver was used with a second order spatial discretization. The transient simulations were solved implicitly with a time step of 0.01 s and a first order temporal discretization to ensure stability. The MRF method was used to model the rotation of the impeller for both the steady and transient simulations.

4.6 Large Eddy Simulations

The dynamic Smagorinsky model was used for modelling the subgrid stresses. LES is capable of resolving the whole boundary layer, but needs a very fine mesh to do that accurately. Having such a fine mesh was not applicable in this study, instead the all y^+ wall treatment was used, making it possible to get reasonable results without resolving the whole boundary layer. Not resolving the boundary layer when performing an LES simulation is a simplification and the results should not be considered to be as good as a pure LES simulation. For this application however, this simplification was considered to be valid since the flow governed by the

rotating impeller was expected to be pressure driven and not as dependent on the boundary layer as many other applications. All LES simulations used method T2, which pours the tracer into the domain, when evaluating the mixing time.

A segregated solver was used with the Bounded-Central scheme used for spatial discretization. The equations were solved implicitly. The temporal discretization was of second order to ensure accuracy. The time step was set depending on the mesh and rotational speed. Two parameters were investigated in order to choose an appropriate time step, CFL number and the relative mesh motion of the rotational region. For an LES simulation, the CFL number should be less than one. Since the SM method was used, it was desired that the relative motion of the stationary and rotational regions should not move further than half a cell per time step at the interface. This gave time steps in the order of 10^{-3} s, the exact time step for each rotational speed is presented in Table 4.2.

Table 4.2: *Time step sizes used in the LES simulations.*

Rotational speed [rpm]	Time step size [s]
105	0.002
135	0.0015
170	0.0012
210	0.001

Since LES is a transient method, some of the results needed to be sampled at each time step and then averaged to get results comparable with the RANS simulations. The data was sampled for approximately 23 000 time steps, which correspond to around 80 impeller rotations. Sampled data was used for calculating power and pumping numbers. Furthermore, sampled data was used to evaluate the resolution of the turbulence for the LES. Two parameters were used for this evaluation, the ratio between the modelled turbulent kinetic energy and the resolved turbulent kinetic energy, and energy spectra of the velocity at three different locations. The variance of the filtered velocities, $\langle \bar{v}_i'^2 \rangle$, were used to calculate the time-averaged resolved kinetic energy, $k_{res} = 0.5 \langle \bar{v}_i' \bar{v}_i' \rangle$ [6]. The modelled turbulent kinetic energy, $k_{sgs} = 3.5 \mu_{sgs} |\bar{s}| / \rho$ [18], was sampled and time-averaged before used for calculating the ratio $k_{sgs} / k_{tot} = k_{sgs} / (k_{res} + k_{sgs})$. To create energy spectrum, the sampled velocity magnitude time series was Fourier transformed. This was done to three equally sized segments of the sampled velocity and then the spectrum was averaged over all three segments. The resulting spectrum was then examined to see if the -5/3 decay was followed by the resolved turbulence, since the main part of an ideal energy spectrum has this slope.

4.7 Existing Simulation Method

The method that has been previously used at FS Dynamics has the same general procedure for mesh creation and simulation start-up as described in this section. It has only been used with the RANS turbulence model and method T1 for tracer introduction, with the same settings as described above. However, 10% of the total volume in the tank has been used as the tracer volume. The mixing time has been evaluated from studying the standard deviation instead of the coefficient of variance. The power number has been evaluated as described in this section. The existing method does not have a general procedure for evaluating the pumping number. Results from using 10% of the total tank volume as the volume of tracer are presented in Section 7.1, but other differences between this existing method and the methods described earlier in this section will not be further discussed in this report.

5 Meshes

In this chapter, both mesh sensitivity studies and descriptions of the final meshes for the RANS and LES simulations are presented. The chapter starts with the mesh study for RANS simulations, followed by the final mesh used in the RANS simulations. Then the corresponding sections for LES are given.

5.1 Mesh Study for RANS Simulations

A mesh study for the RANS simulations was performed to be able to choose an appropriate mesh for the simulations and to be able to provide recommendations for mesh creation in similar cases. The study is divided into two parts. The first part concerns some the important flow characteristics, which are the velocity, power number and pumping number. The second part concerns mixing time.

5.1.1 Flow Characteristics

A mesh study for evaluating velocity, power number and pumping number was conducted, since these are important flow characteristics in applications for mixing with impellers. The rotational speed and the liquid level were set to 340 rpm and 815 mm respectively, which is different than in the rest of this study. However, the higher velocity used in this part of the mesh study makes it conservative, since higher velocities usually require finer cells in the volume mesh.

The mesh study concerning flow characteristics is divided into three parts. The first part focuses on the cell sizes in the rotational region, the second on the cell sizes in the stationary region and the last part focuses on the cells inside the boundary layers.

Rotational Region

As described in Section 4.1, the volume cell sizes were determined by defining surface cell sizes on the boundaries. To change the size of the cells in the rotational region, the target size of the cells on the surface of the impeller and on the interface towards the stationary region were prescribed. A minimum surface cell size was also defined on the impeller to restrict the cells from becoming too small. The meshing tool in STAR-CCM+ then built the volume mesh smoothly between the two surface meshes. Note that by changing the surface cell size on the interface between the two regions, the mesh outside of the rotational region was affected as well. Six different meshes were created and evaluated with the number of cells ranging from 338 000 to 4 844 000. The cell size settings for these meshes are presented in Table 5.1 and pictures of meshes A1, A2 and A5 are found in Appendix C.1.1. The surface cell size on the tank walls was held constant at 10.4 mm. The prism layer meshes at the impeller and tank walls were held constant at y^+ values of around 25 and 13 respectively.

Table 5.1: *Cell size settings for evaluation of flow characteristics in the mesh study for RANS simulations, for the rotational region.*

Mesh	Number of cells	Number of cells in the rotational region	Cell size impeller [mm]	Minimum cell size impeller [mm]	Cell size interface [mm]
A1	4 844 000	3 947 000	0.8	0.8	2.8
A2	1 886 000	1 299 000	2.4	0.8	4.0
A3	713 000	352 000	4.8	1.6	6.4
A4	488 000	165 000	4.8	3.2	8.0
A5	402 000	91 000	6.4	5.6	8.0
A6	338 000	53 000	9.6	9.6	9.6

Velocities at four points defined in Figure 5.1, power number and pumping number were compared for all meshes to evaluate when mesh convergence was reached. This was done by creating plots of the mentioned parameters versus the total number of cells for the evaluated meshes, see Figure 5.2. The plots show that the velocity at points 1, 2 and 4 as well as the power and pumping numbers are constant for all meshes up to the

mesh containing 488 000 cells (A4), where they start to diverge slightly. The velocity at point 3 differs slightly between all meshes, but starts to diverge more drastically than the others for the mesh containing 488 000 cells (A4).

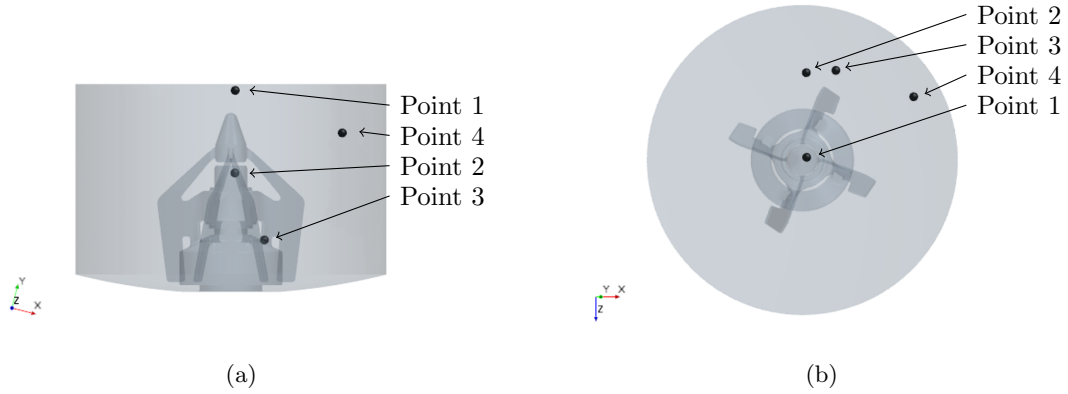


Figure 5.1: Positions for points 1-4 displayed in a view from (a) the side and (b) the top. Note that only the rotational region is seen, and that it is slightly distorted from the global coordinate system.

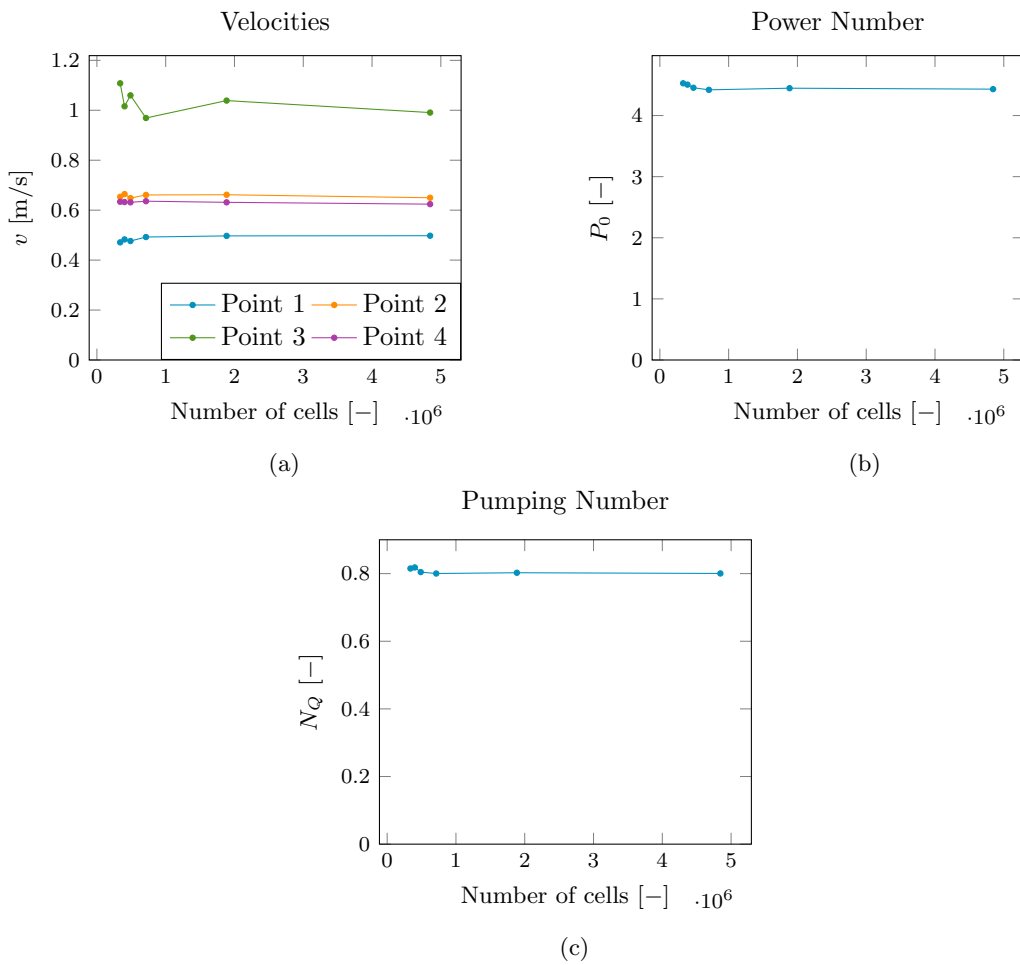


Figure 5.2: (a) Velocities, (b) power number and (c) pumping number for meshes A1-A6 described in Table 5.1.

Stationary Region

The cell sizes in the stationary region were changed by defining the surface cell size on the tank walls. The surface cell sizes on the impeller and the interface were kept constant at 2.4 mm (minimum 0.8 mm) and 4 mm respectively, which gave approximately 1.3 million cells inside the rotational region for all meshes. Five different meshes were evaluated, with a number of cells ranging from 101 000 to 893 000 in the stationary region, whose settings are presented in Table 5.2. Pictures of meshes B1, B2 and B4 are shown in Appendix C.1.2.

Table 5.2: Cell size settings for evaluation of flow characteristics in the mesh study for RANS simulations, for the stationary region.

Mesh	Number of cells	Number of cells in the stationary region	Cell size tank walls [mm]
B1	2 200 000	893 000	8.0
B2	1 886 000	586 000	10.4
B3	1 625 000	323 000	20.0
B4	1 438 000	136 000	48.0
B5	1 333 000	101 000	80.0

Velocities at points 5-8, presented in Figure 5.3, power number and pumping number were compared for meshes B1-B5, and are plotted against the number of cells outside the rotational region in Figure 5.4. It is seen that the meshes containing 323 000 cells in the stationary region (B3) and more (B1-B2) give no major changes to the results.

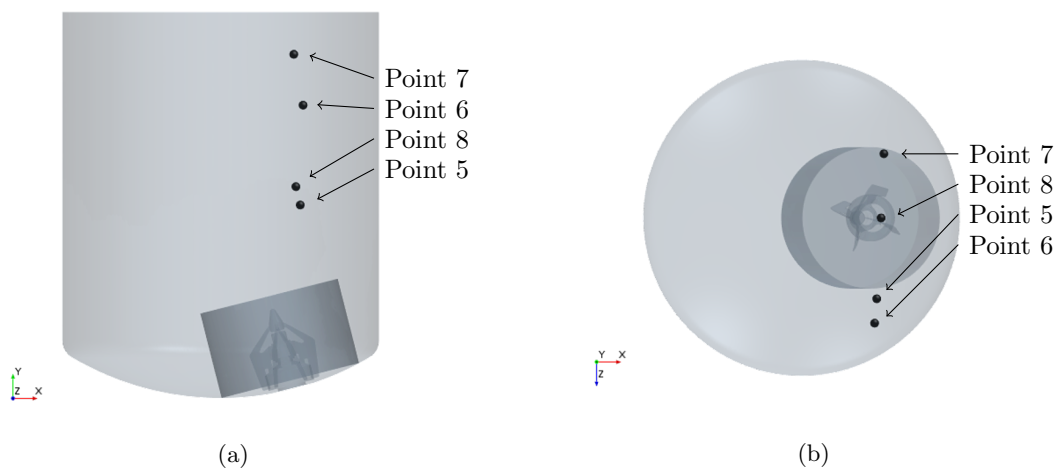


Figure 5.3: Positions for points 5-8 displayed in a view from (a) the side and (b) the top.

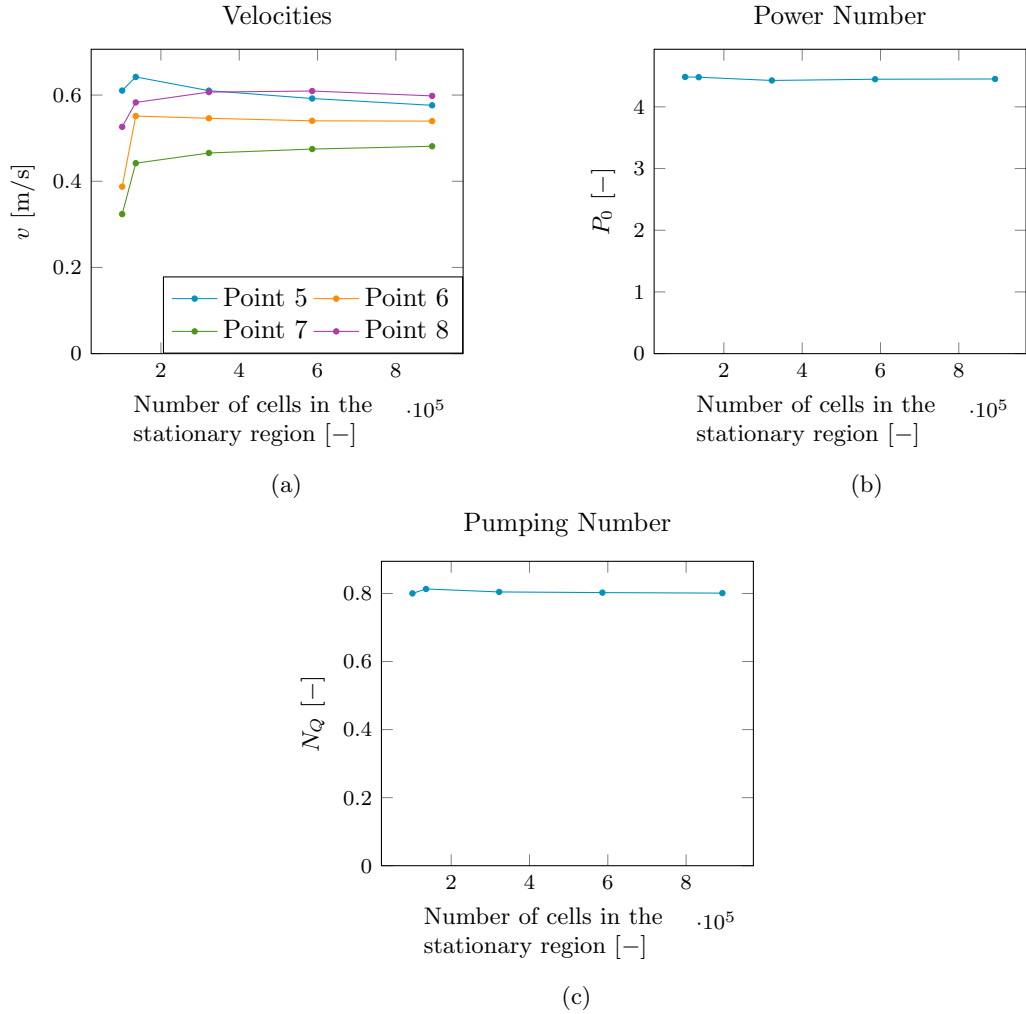


Figure 5.4: (a) Velocities, (b) power number and (c) pumping number for meshes B1-B5 described in Table 5.2.

Boundary Layers

The all y^+ wall treatment is supposed to give reasonable results for a wide range of y^+ values, as discussed in Section 2.1.5. However, since it uses different methods to account for y^+ values in the viscous sublayer, buffer region and log-law region, it is still of interest to investigate if different y^+ values will give varying results. Different boundary layer meshes were achieved by varying the number of prism layers, the stretching of the prism layers and the total thickness of the prism layers. Since not only y^+ is important when creating the boundary layer mesh, the number of prism layers were held between 4 and 6 to have enough cells to get an accurate solution. The evaluation of the effect of y^+ value on the flow characteristics was done while keeping the rest of the mesh relatively constant with the mesh settings defined by mesh A2 and B2 in tables 5.1 and 5.2. The prism layer meshes were then changed at the impeller and tank separately while keeping the other one constant.

Five meshes, with the average y^+ value on the rotating part of the impeller ranging from 4.5 up to 40, were evaluated while keeping the average y^+ on the tank walls at 13. The prism layer settings for these meshes are found in Table 5.3. For validation purposes, a prism layer mesh containing 30 cells using a stretching of 1.2 and a thickness of 3.2 mm was created. This mesh gave an average y^+ value of 0.72 at the impeller. Since the first cell was located inside the viscous sublayer and 30 prism layers were used, this mesh is assumed to resolve the boundary layer and thus give the most accurate results. Pictures of the fully resolved boundary layer mesh and mesh C4 are found in Appendix C.1.3.

Table 5.3: *Prism layer settings at the impeller for evaluation of flow characteristics in the mesh study for RANS simulations.*

Mesh	Average y^+	Number of layers	Stretching	Thickness [mm]
C1	4.5	6	1.6	1.84
C2	8.3	5	1.6	1.84
C3	15.0	5	1.5	2.66
C4	27.7	5	1.2	2.66
C5	39.4	4	1.2	2.66

Figure 5.5 displays velocities at points 1-4, power number and pumping number plotted against y^+ values for meshes C1-C5. The results from the mesh resolving the boundary layer are plotted as dashed lines. All variables are fairly constant over the interval of y^+ values, except velocity point 3 where y^+ values of around 5-15 give a slightly higher velocity. Hence, it is seen that it is probably desirable to have a y^+ value higher than 15 if it is not possible to resolve the whole boundary layer.

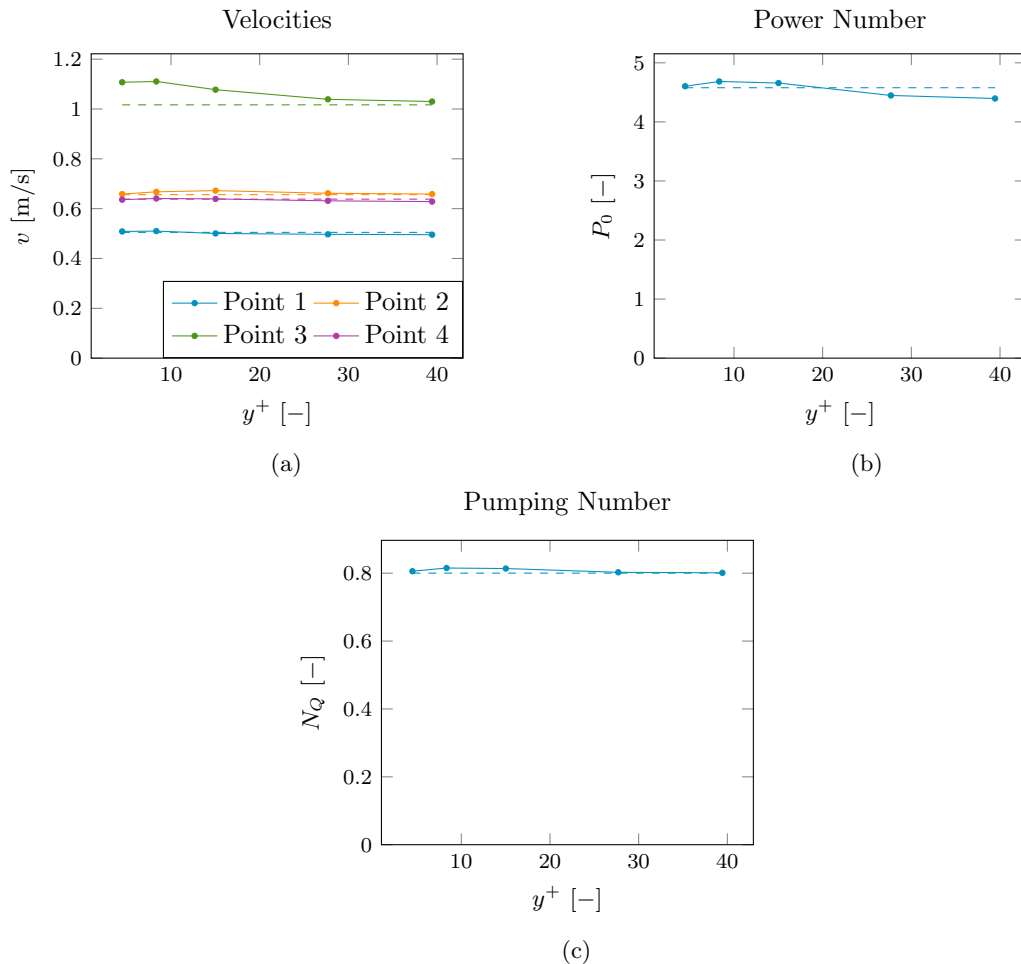


Figure 5.5: (a) Velocities, (b) power number and (c) pumping number for meshes C1-C5 described in Table 5.3. Dashed lines correspond to the simulation with a resolved boundary layer.

Since the majority of the turbulence is created at the impeller, the prism layers at the tank walls were not expected to have much impact on the solution. Hence, only three different meshes were evaluated, with settings presented in Table 5.4, giving averaged y^+ values on the tank walls of 12.5, 19.3 and 31.3. All these meshes gave the same results in terms of velocities, power number and pumping number.

Table 5.4: *Prism layer settings at the tank walls for evaluation of flow characteristics in the mesh study for RANS simulations.*

Mesh	Average y^+	Number of layers	Stretching	Thickness [mm]
D1	12.5	5	1.2	4
D2	19.3	5	1.2	6
D3	31.3	4	1.2	6.8

5.1.2 Mixing

The simulations for the mesh study regarding mixing time were set up to match one of the set ups used in the physical testing, with a water level of 670 mm and the rotational speed set to 105 rpm. For this study, a base mesh was picked from the mesh study concerning flow characteristics by combining meshes A2, B2, C4 and D1 in Tables 5.1-5.4. This mesh was first compared to a mesh with different cell sizes and then to a mesh with a different boundary layer mesh.

To evaluate if the chosen mesh size was sufficiently fine, a slightly coarser mesh was created with the same boundary layer settings. The mesh size settings for the two meshes are presented in Table 5.5 together with their resulting mixing times. The mixing time was evaluated using method T1, where the solvers for velocity, pressure and turbulent quantities are frozen, with the tracer placed just below the free surface. The amount of tracer was 24.6 litres. The resulting mixing times are 63.4 s and 63.1 s for the chosen mesh and the coarser respectively. Hence, there is no significant difference between these two meshes concerning mixing time.

Table 5.5: *Cell size settings for evaluation of mixing time in the mesh study for RANS simulations.*

Mesh	Number of cells	Cell size impeller [mm]	Minimum cell size impeller [mm]	Cell size interface [mm]	Cell size tank [mm]	Mixing time [s]
A2, B2, C4, D1	1 591 000	2.4	0.8	4.0	10.4	63.4
-, -, C4, D1	1 186 000	4.0	0.8	6.4	12.0	63.1

In the mesh study concerning flow characteristics it was concluded that an average y^+ value above 15 is desired if it is not possible to resolve the whole boundary layer. For a rotational speed of 340 rpm, the chosen base mesh gave y^+ values in the desired range. However, when the rotational speed was lowered to 105 rpm the y^+ values got as low as 8.2 at the impeller and 2.4 at the tank walls. Therefore, a second mesh was created with higher y^+ values. The settings and y^+ values for these two meshes are shown in Table 5.6.

Table 5.6: *Prism layer settings for evaluation of mixing time in the mesh study for RANS simulations. Note that the y^+ values are surface averaged.*

Mesh	Impeller				Tank walls			
	y^+	Thickness [mm]	Stretching	Number of layers	y^+	Thickness [mm]	Stretching	Number of layers
A2, B2, C4, D1	8.2	2.7	1.2	5	2.4	4.0	1.2	5
A2, B2, -, -	24.0	5.6	1.2	4	26.6	10.8	1.2	3

The boundary layer meshes in Table 5.6 were evaluated using both of the different strategies of tracer introduction, presented in Section 4.3, to verify that any change in mixing time from changing the boundary layer mesh applies to both methods. Method T1 uses a fixed volume of tracer placed in the top of the domain

while freezing all solvers except the one regarding the species transport. Method T2 uses an inlet to mimic pouring of the tracer. The amount of tracer was set to correspond to the physical tests of 3.3 litres. The mixing time results are shown in Figure 5.6. It is evident from the results that the boundary layer mesh has an influence on the mixing time and that an inadequate prism layer mesh with too low y^+ while using wall functions will give a shorter mixing time.

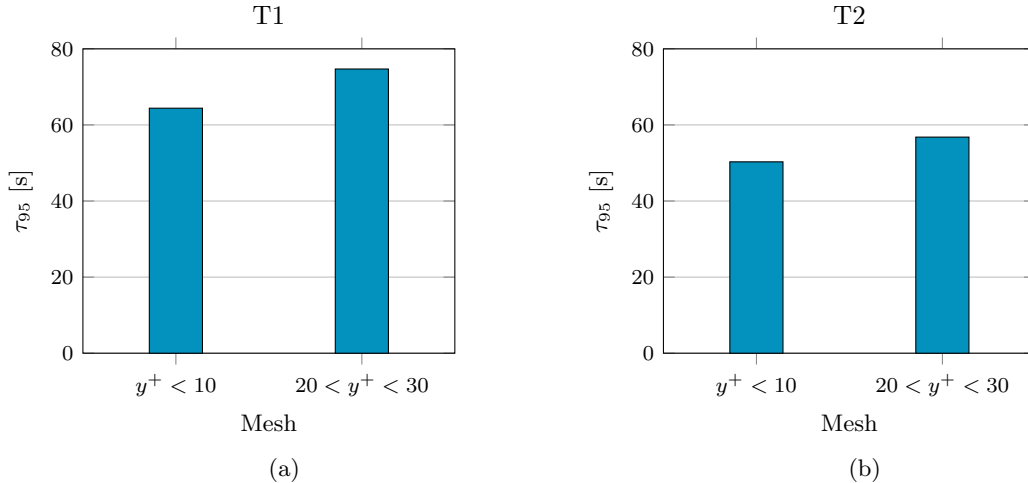


Figure 5.6: *Mixing time for the meshes in Table 5.6, for simulations where the tracer is introduced (a) using method T1 and (b) using method T2.*

5.2 Final Meshes used for RANS Simulations

From the mesh study for RANS simulations, it can be concluded that a mesh containing around 1 million cells is sufficient to capture both the investigated flow characteristics as well as the mixing time. The cells should be distributed such that the mesh is denser close to the impeller, while still having at least 300 000 cells in the stationary region. Using these guidelines, two meshes were created for the following RANS simulations. Different meshes were needed for the two methods of introducing a tracer explained in section 4.3. When mimicking the pouring of tracer, method T2, a finer mesh was needed in the region around the inlet in order to capture the velocity gradients in that area. A cylinder of radius 22 mm was created at the location of the inlet, which was extracted 70 mm into the domain. The volume cell size inside this cylinder was set to 6 mm. Except for this refinement zone, the mesh settings for the RANS simulations are the same for both methods of introducing a tracer. The cell size settings are presented in Table 5.7, where 60-65% of the total number of cells is located inside the rotational region for all meshes. For pictures of the two final meshes see Appendix C.2.

Table 5.7: *Cell size settings for meshes used in RANS simulations.*

Tracer introduction	Number of cells (approximately)	Cell size impeller [mm]	Minimum cell size impeller [mm]	Cell size interface [mm]	Cell size tank [mm]
T1	1 350 000	2.4	0.8	5.6	10.4
T2	1 400 000	2.4	0.8	5.6	10.4

The investigation of the boundary layer mesh showed that some differences in results for both flow characteristics and mixing time occur at approximately $4 < y^+ < 10-15$. Since it would be too computationally demanding to resolve the whole boundary layer for the simulations in this project, it was desired to keep the average y^+ values above 15 for both the impeller and the tank. Since the y^+ value depends on velocity, the boundary layer mesh needed to be changed when the rotational speed of the impeller was changed. The prism layer settings for the different velocities are presented in Table 5.8. Note that it was possible to have the same settings for 170 and 210 rpm while still having a y^+ value above 15.

Table 5.8: *Prism layer settings for meshes used in RANS simulations. Note that the y^+ values are surface averaged.*

Speed [rpm]	Impeller				Tank walls			
	y^+	Thickness [mm]	Stretching	Number of layers	y^+	Thickness [mm]	Stretching	Number of layers
105	24.3	5.6	1.2	4	27.0	10.8	1.2	3
135	23.4	4.0	1.2	4	22.2	7.2	1.2	3
170	20.8	3.2	1.3	4	16.4	4.8	1.3	3
210	25.4	3.2	1.3	4	20.1	4.8	1.3	3

The CFL numbers were evaluated for the simulation at 210 rpm using method T2, since this speed together with a smaller mesh around the inlet gave the highest CFL numbers. The average CFL number for this simulation is 0.97 for the whole tank and 6.8 for the rotational region. A contour plot of the CFL number is seen in Figure 5.7. The CFL number is higher in the rotational region where the smallest cells and the highest velocities are located.

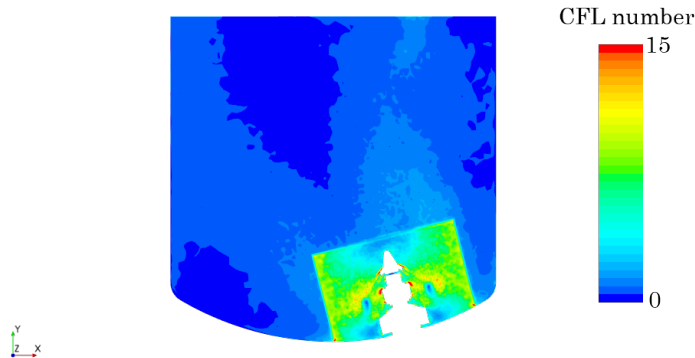


Figure 5.7: *CFL number from a RANS simulation at 210 rpm on a plane going through the center of both the tank and the impeller.*

5.3 Mesh Study for LES

From the mesh study for the RANS simulations, it can be concluded that the mixing time results are more sensitive to the mesh size than the other flow characteristics. Hence, the only the mixing time was examined in the mesh study for LES.

A base mesh was created based on the results from the mesh study for RANS simulations. To evaluate the performance of this mesh a finer mesh was created by dividing the cell size in half, giving 5-6 times more cells, and a coarser mesh was created by decreasing the total number of cells to half the amount. For all three meshes, the time step was selected to limit the rotation at the interface between the rotational region and the outer to half a cell. Hence, not only was the finer mesh heavier per iteration in terms of computational efforts, but it required more time steps to achieve the same physical time in the solution. The main settings changed between the meshes and the time step sizes are presented in Table 5.9 and pictures of these three meshes are found in Appendix C.3. For this evaluation, the boundary layer mesh was held fairly constant and gave an average y^+ value of around 10 for the impeller and 6 for the tank walls.

Table 5.9: *Cell size settings for evaluation of mixing time in the mesh study for LES.*

Mesh	Number of cells	Cell size impeller [mm]	Minimum cell size impeller [mm]	Cell size interface [mm]	Cell size tank [mm]	Time step [s]
Coarse	326 000	3.6	2.4	9.6	13.6	0.0027
Base	647 000	2.4	1.6	6.4	10.4	0.002
Fine	3 539 000	1.2	0.8	3.2	5.2	0.001

The resulting mixing times from the meshes presented in Table 5.9 are plotted in Figure 5.8 against the total number of cells. The mixing time is distinctly lower for the coarse mesh and almost the same for the other two. Hence, the base mesh created is considered to be sufficiently fine but the cell size should not be increased much further.

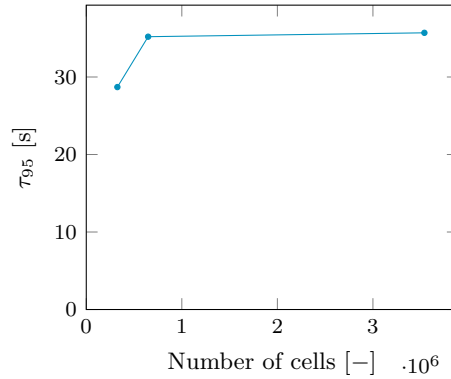


Figure 5.8: *Mixing time for the meshes presented in Table 5.9.*

5.4 Final Meshes used for LES

It was concluded in the mesh study for LES that a mesh of approximately 600 000 cells was enough to reach mesh convergence. Hence, the final meshes used for the LES simulations have the same settings as the base mesh in Section 5.3, and these are presented again in Table 5.10. The tracer was poured into the domain using an inlet (method T2) for all LES simulations. The mesh around the inlet was constructed in the same way as for the RANS simulations described in Section 5.2, except that the volume cell size was set to 4.8 mm which is slightly finer than the RANS simulations. Pictures of the final LES mesh is shown in Appendix C.4.

Table 5.10: *Cell size settings for meshes used in LES simulations.*

Number of cells (approximately)	Cell size impeller [mm]	Minimum cell size impeller [mm]	Cell size interface [mm]	Cell size tank [mm]
575 000	2.4	1.6	6.4	10.4

Since the LES simulations were conducted using the all y^+ wall treatment, the same guidelines as in the RANS simulations, with $y^+ > 15$, were followed also for the LES simulations to get accurate approximations from the wall functions. Two meshes were created with slightly different prism layer settings. One mesh was used for 105 and 135 rpm, and the other mesh was used for 170 and 210 rpm. The prism layer settings of these two meshes are presented in Table 5.11. Note that the y^+ value at the tank wall for 170 rpm, which is 14.8, is slightly lower than desired. However, this is considered tolerable since the guidelines were concluded from the boundary layer mesh study of the impeller which is more important than the tank, and the mesh study for the tank walls did not show any differences in results for y^+ values as low as 12.5.

Table 5.11: *Prism layer settings for meshes used in LES simulations. Note that the y^+ values are surface averaged.*

Speed [rpm]	Impeller				Tank walls			
	y^+	Thickness [mm]	Stretching	Number of layers	y^+	Thickness [mm]	Stretching	Number of layers
105	18.2	7.2	1.2	4	21.2	12	1.2	3
135	22.2	7.2	1.2	4	26.5	12	1.2	3
170	20.5	5.6	1.2	4	14.8	6.4	1.3	3
210	24.3	5.6	1.2	4	27.7	6.4	1.3	3

The time steps were chosen such that for each time step, the relative motion of the regions at the interface did not exceed the length of half a cell. Hence, the time step was based on both the mesh and the rotational speed of the impeller, and a higher speed required a smaller time step. The time steps for the four rotational speeds are presented in Table 5.12. The CFL numbers also needed consideration when choosing the time step, hence they are presented in the same table. A contour plot of the CFL numbers for 210 rpm is presented in Figure 5.9. There are some regions near the impeller which have a CFL number of 1 or higher, as indicated by the red regions. However, since the CFL numbers are lower than 1 in almost the entire tank, the overall CFL numbers are considered acceptable.

Table 5.12: *Time step sizes and CFL numbers for LES simulations.*

Speed [rpm]	Time step size [s]	Average CFL number	Average CFL number in rotational region
105	0.002	0.077	0.48
135	0.0015	0.075	0.46
170	0.0012	0.076	0.46
210	0.001	0.078	0.48

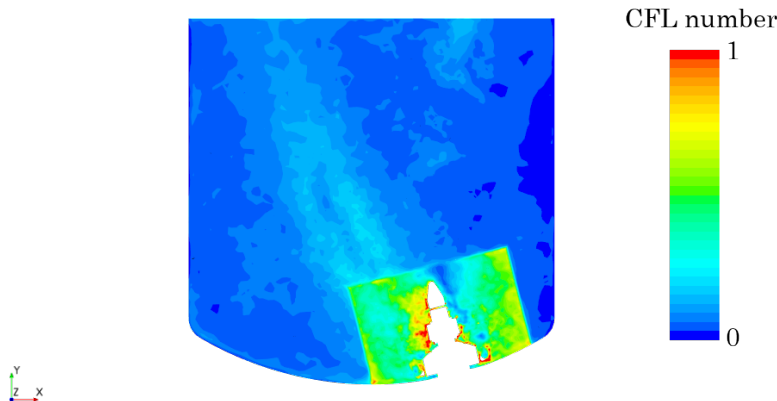


Figure 5.9: *CFL number from a LES simulation at 210 rpm on a plane going through the center of both the tank and the impeller.*

The resolution of turbulence for the LES simulations were evaluated by examining the ratio of time-averaged modelled turbulent kinetic energy to the total turbulent kinetic energy and examining the energy spectra created from sampled velocity magnitude time series at three points inside the domain. Only the results from the lowest rotational speed, 105 rpm, and the highest, 210 rpm, are presented.

The average ratio of the turbulent kinetic energy, k_{sgs}/k_{tot} , was evaluated by taking the volume mean value of the entire tank. For all rotational speeds, around 95% of the turbulent kinetic energy is resolved and only 5% modelled. A contour plot of the turbulent kinetic energy ratio is presented in Figure 5.10 to show the regions of high and low resolution. The scale is set at a maximum of 0.1, which means that a red area has a ratio of 0.1 or higher. In almost the entire plane the ratio is below 0.1, which means that less than 10% of the turbulence is modelled. The least resolved areas are located in the bottom of the tank outside the rotational region and in the top corners. These are regions containing the largest cells in the domain, hence the smaller scales are not captured by the mesh. There is a clear distinction between the rotating and stationary regions. This is due to the fact that the time averaging is performed at each cell, and the cells in the rotational region move during the simulation.

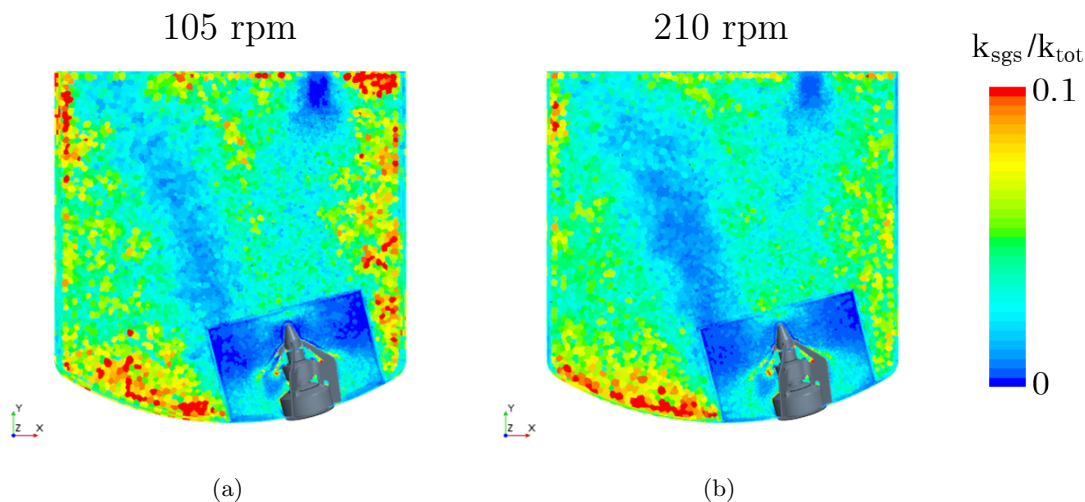


Figure 5.10: *The ratio between the modelled turbulent kinetic energy and the total turbulent kinetic energy plotted on a plane through the center of the impeller and tank, for LES simulations at (a) 105 rpm and (b) 210 rpm.*

The three points used to create energy spectra are all located outside the rotational region, but in areas where a lot of turbulence is believed to exist, for placements see Figure 5.11. At all points, the energy spectra for both 105 rpm and 210 rpm behave similarly and the curves for 105 rpm lie below the curves for 210 rpm, see Figure 5.12. All the points have $-5/3$ ranges, some longer than others. This indicates that the turbulence is well resolved. The spectra were only averaged over three time segments which is not enough to get a smooth spectra, but sufficient to see the overall trend.

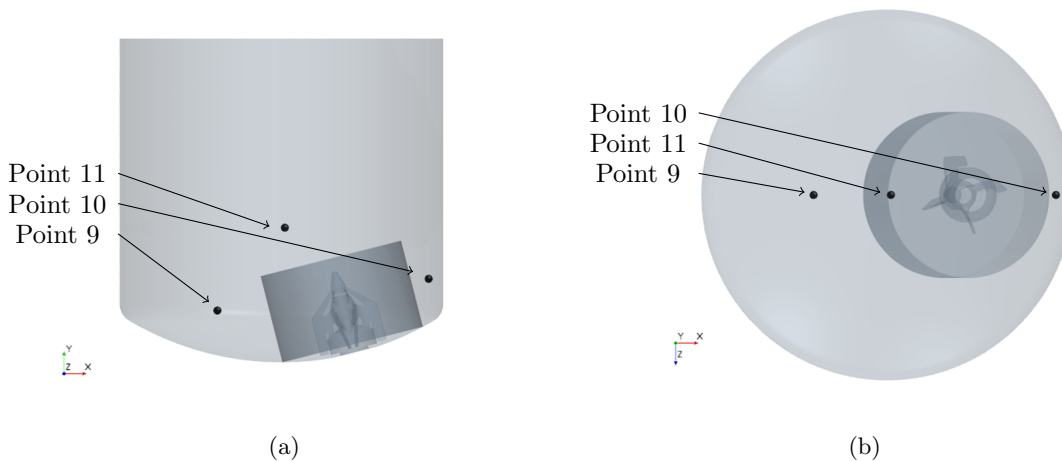


Figure 5.11: *Placement of points 9-11 displayed in a view from (a) the side and (b) the top.*

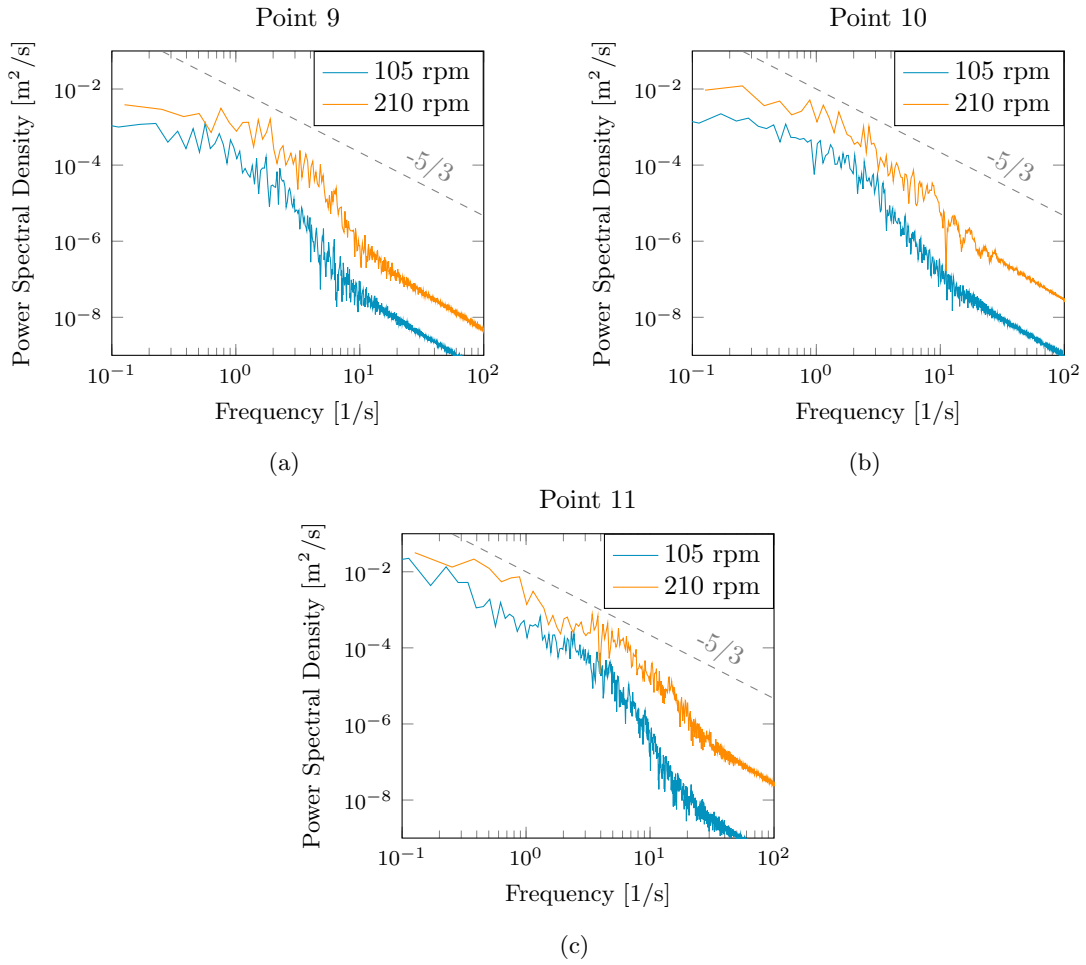


Figure 5.12: Energy spectra created from the velocities for 105 rpm and 210 rpm, plotted together with a line representing a decay of $-5/3$, at (a) point 9, (b) point 10 and (c) point 11.

6 Validation Study

In this chapter, comparisons between the RANS simulations, LES simulations and physical tests are presented. The chapter starts by examining the mixing process for the performed simulations at 105 rpm. The mixing times for all rotational speeds are then compared and discussed followed by comparisons of power and pumping numbers. The chapter finishes by comparing the computational requirements of the different simulation methods.

6.1 Mixing Process

Pictures from the mixing process at 105 rpm are presented in Figure 6.1, for snapshots at every 6 seconds, see Appendix D.1-D.3. It is clear that there are some differences in the mixing process between the methods. Firstly, the effect of the inlet of tracer to mimic pouring together with a higher density of the tracer for method T2 gives a higher concentration of tracer in the bottom of the tank during the mixing process. For method T1, where the tracer is initiated using a fixed volume, the concentration is higher at the top where the tracer was initiated, and the tracer is then mixed downwards. The mixing process looks similar for both the RANS T2 and LES methods in the beginning, but it is seen that the LES mixes faster after a while. This is also seen when examining the coefficient of variance, plotted in Figure 6.2. The curves for the RANS and LES simulations using method T2 follow each other well until around 20 s, where the curve from the LES drops faster than the curve from the RANS simulation. The curve for RANS T1 is less steep, which means that the mixing process is slower using this method. Furthermore, it is seen in Figure 6.1 that the LES has more fluctuating results of tracer concentration compared to the RANS simulations, which is expected since it resolves some of the turbulence that transports the tracer.

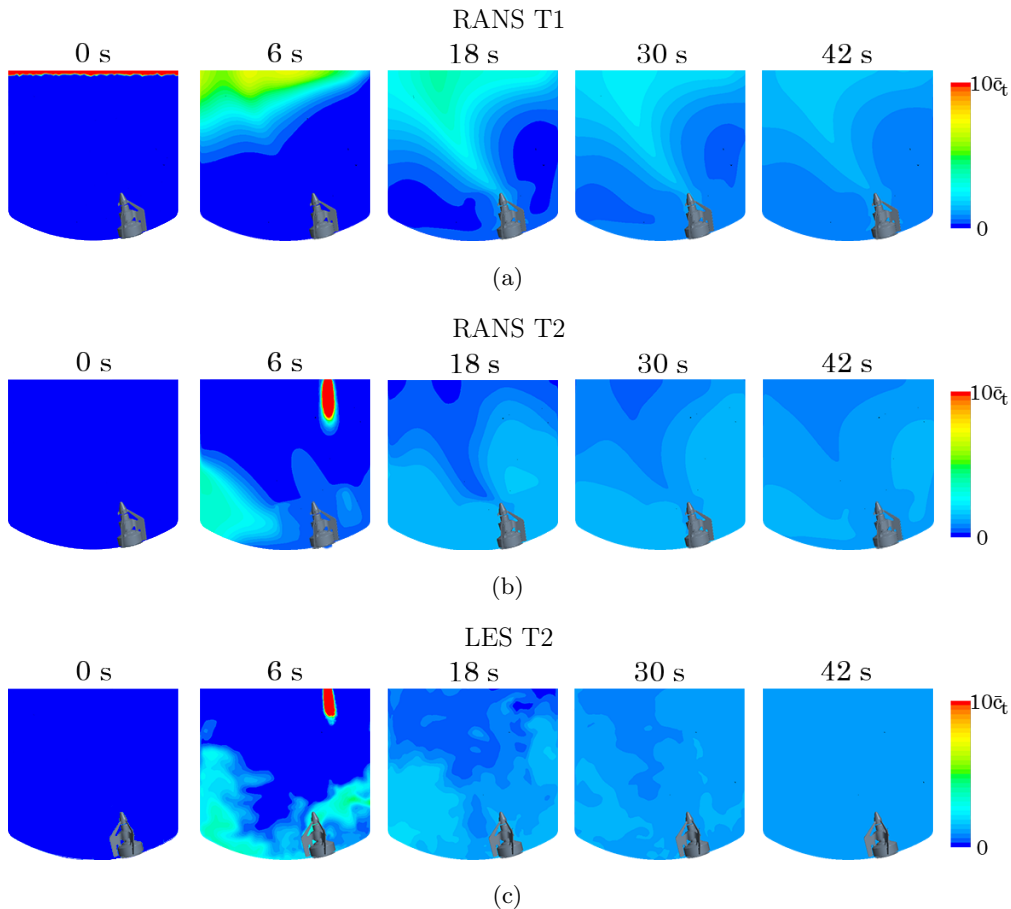


Figure 6.1: Pictures from the mixing process at 105 rpm for (a) RANS T1, (b) RANS T2 and (c) LES T2, on a plane going through the center of the tank and the impeller.

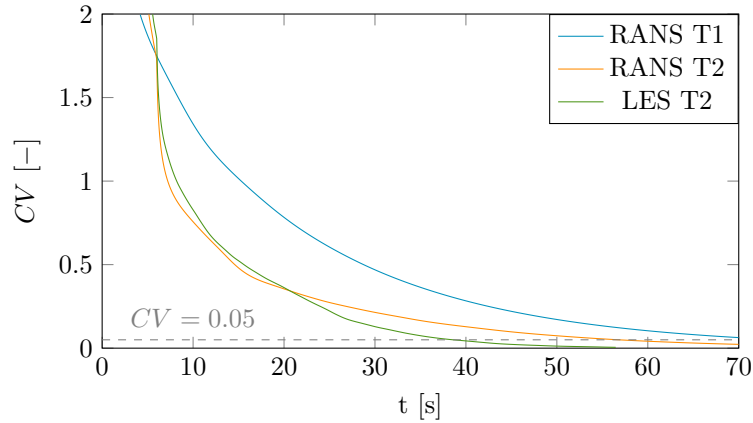


Figure 6.2: *Coefficient of variance during the mixing process at 105 rpm.*

The difference in fluctuating concentration of tracer is also seen when tracking the tracer concentration at the conductivity points, seen in Figure 6.3 and Appendix D.4. For the RANS T1 method, the curve does not fluctuate at all. The RANS T2 method captures some large fluctuations. The difference in fluctuations between the two RANS methods may be caused by the different mixing processes. The LES simulations captures both large and small fluctuations.

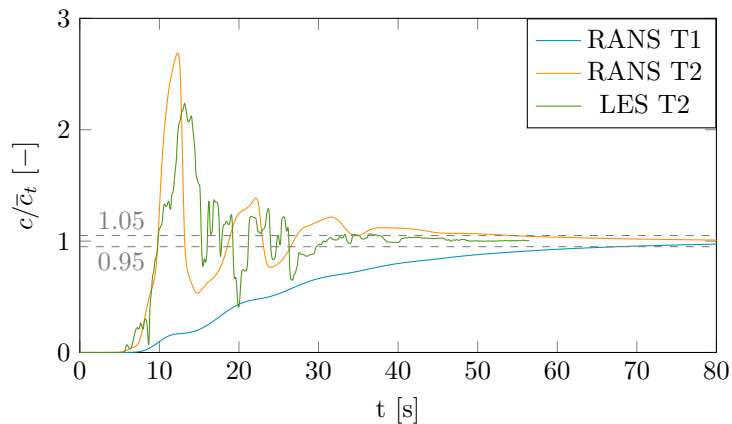


Figure 6.3: *Normalized tracer concentration at CP1.*

6.2 Mixing Time

For the mixing times, both local and global times were compared since the physical tests were only evaluated locally. The global mixing times from the physical testing are based on the mean of the two local mixing times. Care should be taken since only two points are probably not enough to successfully evaluate the correct global mixing time. Therefore, local mixing times are presented as well when comparing the simulations with the physical tests, even though a local mixing time is not as representative for the mixing in the whole tank as evaluating the mixing time globally. The mixing times from RANS simulations using a fixed volume of tracer (method T1), RANS simulations mimicking the pouring of saline (method T2), LES simulations using method T2 and results from the physical testing are plotted against the four different rotational speeds in Figure 6.4. As expected, the results from the LES simulations are closest to the physical tests. The RANS T2 simulations overpredict the mixing time by an average of 50%. This agrees with the study performed by Haringa et al.[10], mentioned in Section 1.1, which resulted in a 60% overprediction using a RANS method. However, if the mixing time at 210 is neglected, the RANS T2 method overpredicts by 30%. The RANS T1 method overpredicts by 120%, but it should be noted that this method does not agree with set up from the physical testing.

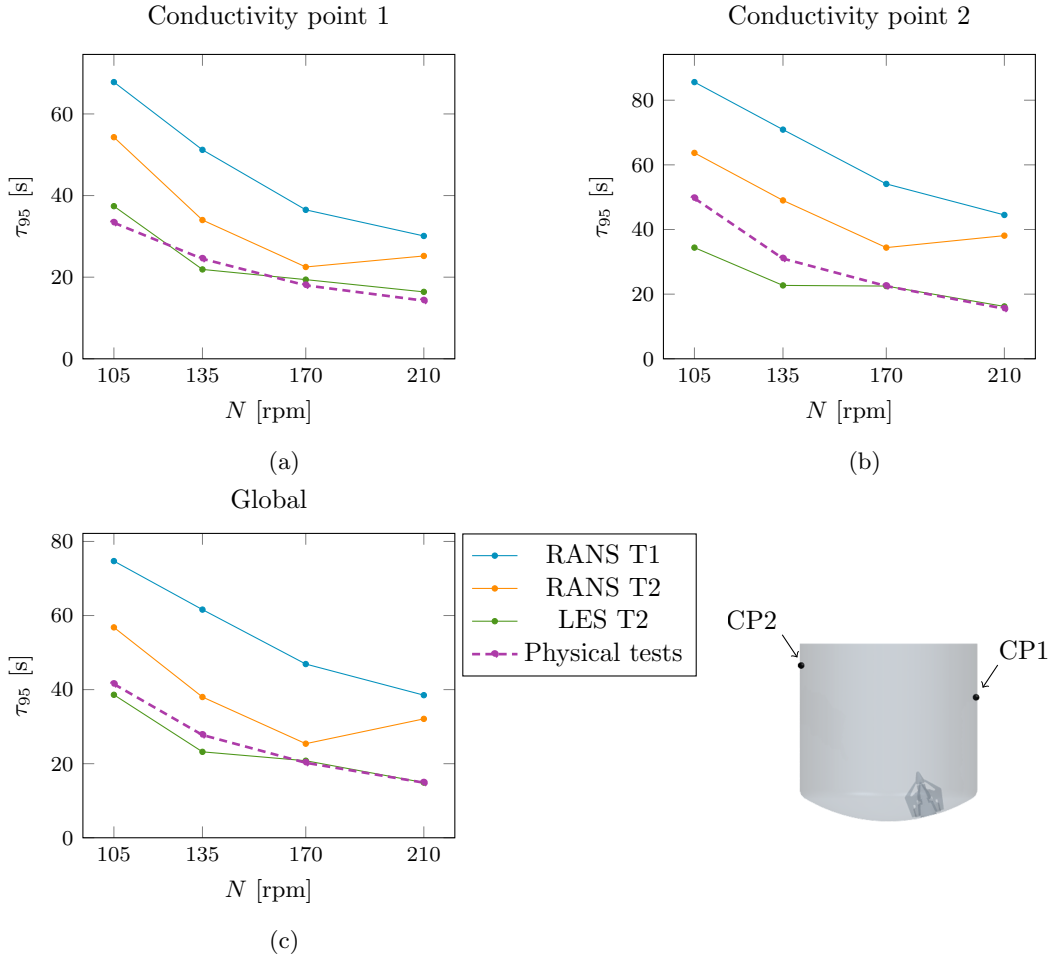


Figure 6.4: Local mixing time at (a) CP1, (b) CP2 and (c) global mixing time, for RANS simulations, LES simulations and physical tests. Results presented for rotational speeds of 105, 135, 170 and 210 rpm.

When examining the mixing times results, an interesting point is seen at 210 rpm for RANS simulations using method T2. Using this method, the mixing time of 210 rpm does not follow the trend with faster mixing at faster velocities. To investigate this, curves of CV versus time were compared for 170 and 210 rpm, see Figure 6.5. The two speeds have similar curves until approximately 10 s into the simulation (4 s after closing the inlet). After that, the slope of the CV from 170 rpm gets steeper than that of 210 rpm. Therefore, the CV drops much faster and fully mixed conditions are reached earlier.

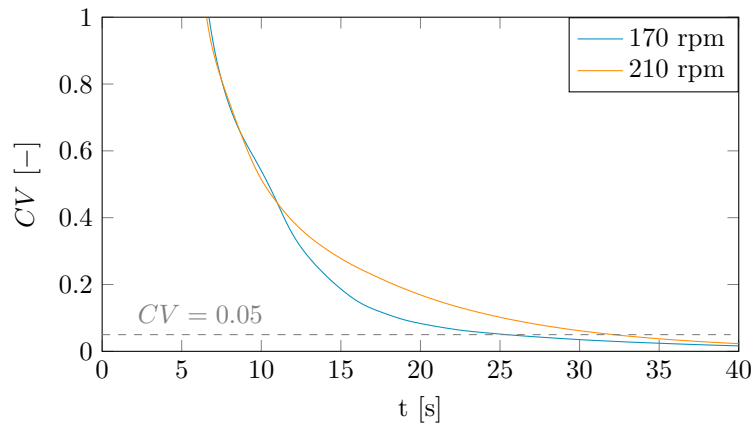


Figure 6.5: CV for rotational velocities at 170 and 210 rpm for RANS simulations using method T2.

Pictures at every 6 seconds of the mixing process for 170 and 210 rpm are given in Figure 6.6. At 6 s, it is seen that the tracer has moved further into the domain for 210 rpm, due to the faster speed. However, at 18 and 24 s it is clear that the tracer is mixed better at 170 than 210 rpm. It seems that a higher concentration of the tracer is caught in the center of the tank.

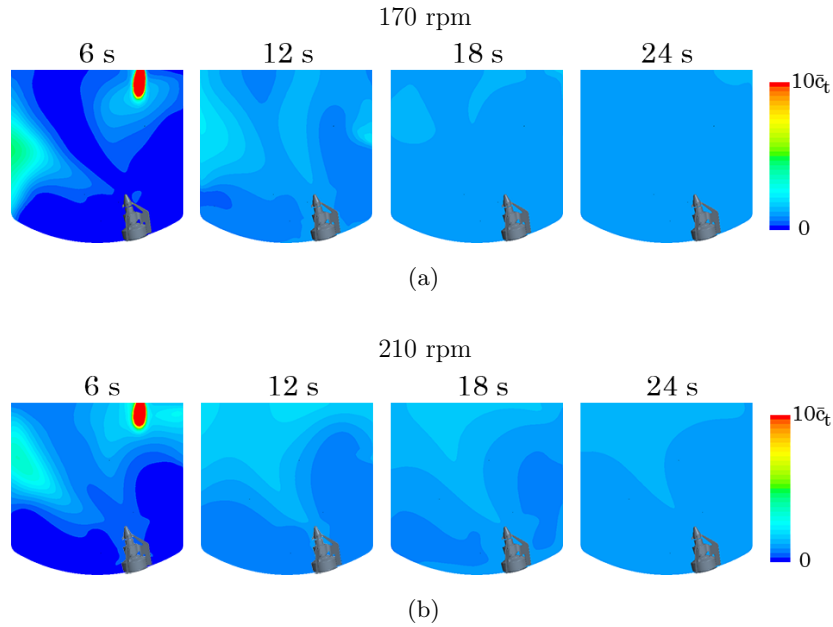


Figure 6.6: Pictures of the mixing process, on a plane going through the center of both the tank and the impeller, at every 6 seconds for RANS simulations using method T2 at (a) 170 rpm and (b) 210 rpm.

Another interesting finding during the study of mixing times is that the LES simulations differ from one run to another using the exact same settings. Three different simulations have been performed with the same setup at 170 rpm, starting directly after closing the inlet of tracer after 6 s. The maximum difference in global mixing time between these three simulations is about 10%. For the local mixing times it is even greater, which is expected due to that the local variations are more affected by the modelling.

6.3 Power Number

Power number results from all four rotational speeds are presented in Figure 6.7. The results are plotted together with the results from physical tests performed at 630 rpm, which gave a power number of 5.8. It was not possible to get results from other rotational speeds from the physical tests, due to the method of calculating the power number by measuring the torque and speed at which the rotational part of the impeller lost connection to the stationary part. Therefore, a RANS simulation at 630 rpm was performed as well, giving a power number of 4.6, which is in the same range as those of the other RANS simulations at lower speeds. Due to the limitation of the time step in an LES simulation, it was decided that it would be too computationally demanding to run a simulation at 630 rpm. The results from the simulations are fairly constant for all velocities, which agrees with the theory saying that the power number is constant in the fully turbulent region. However, the results from both LES and RANS simulations underpredict the power number, where LES underpredicts by 15% and RANS simulations underpredict by 20%.

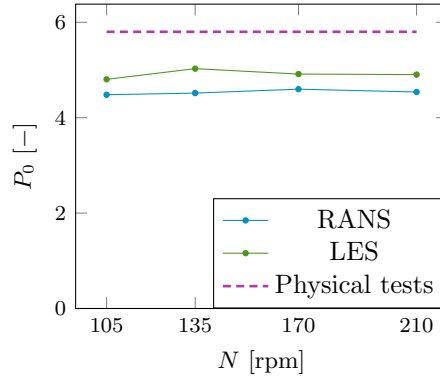


Figure 6.7: Power number for the different rotational speeds for the RANS and LES simulations, together with the result from physical testing at 630 rpm.

6.4 Pumping Number

Pumping number for the RANS and LES simulations are plotted against the rotational velocities in Figure 6.8. Since the pumping number is hard to measure empirically, no results from physical testing were achieved. While the pumping number results from the RANS simulations are fairly constant, the LES gives more varying results for the different velocities. Furthermore, the LES results are lower than the results from RANS simulations. This is probably due to that the impeller swept area was defined based on a RANS simulation, which is further discussed in Section 7.5. Hence, a different impeller swept area may be better suited for this comparison than the one used.

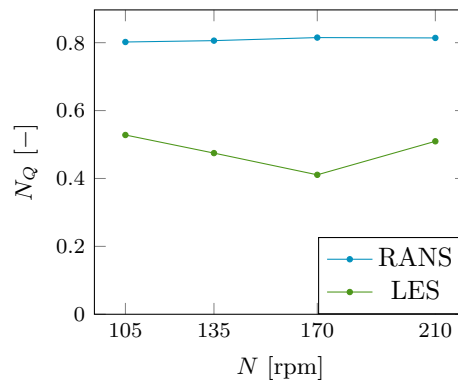


Figure 6.8: Pumping number for the different rotational speeds for the RANS and LES simulations.

6.5 Computational Requirements

To be able to compare the computational demand of the different simulations performed in this project, the total CPU time has been estimated, which is presented in Table 6.1. This table gives an estimate from performing the simulations at 105 rpm using the clusters at FS Dynamics. For the RANS simulations, the times presented are the total time from running the steady-state simulations, which converges after approximately 30 000 iterations, plus the time it takes to reach fully mixed conditions. For the LES, the times are based on the time it takes for the flow to fully develop, which is approximately 60 s, plus the time for the mixing. Note that for these estimations, all non-active models have been turned off, hence the "Multi-component liquid" and gravity was not active before adding the tracer. Having the "Multi-component liquid" model turned on with only one component requires more CPU time than with it turned off, even though the same solution is obtained.

Table 6.1: *Computational requirements for the simulations performed at 105 rpm.*

Turbulence model	Tracer introduction	Number of cells	Time step size [s]	Total CPU time [CPUh]	Physical time if using 20 processors
RANS	T1	1 600 000	0.01	296	14.8 h
RANS	T2	1 600 000	0.01	480	24 h
LES	T2	650 000	0.002	1644	3 days 10 h
LES	T2	3 500 000	0.001	18 670	38 days, 22 h

As seen from the table, it takes more than 3 times longer time to perform the LES simulation with 650 000 cells than the RANS simulation using method T2 with a much denser mesh, which is due to the much smaller time step. If the cell size of the LES is cut in half, which gave approximately 3 500 000 cells, it requires approximately 10 times more CPU hours. Furthermore, when comparing the two different RANS simulations, it is seen that using method T1 is cheaper than using T2. A lot of computational power is saved when the solvers for velocity, pressure, turbulent kinetic energy and turbulent dissipation rate are frozen during the mixing. This is the reason for the difference between the two RANS simulations, since the two require the same computational power for their steady-state solutions. However, the mixing times for the simulation using method T1 are longer than those using T2, which means that if the two simulations would have been run for the same amount of time in the simulation, the difference would be even greater.

Even though the LES simulations require more computational power than the RANS simulations, it is not too much to be considered completely unfeasible in these kinds of applications. There is always a trade-off between accuracy and computational requirements. If a high accuracy is needed and the computational requirements can be afforded, using this type of LES with wall functions can be a good option.

7 Evaluation of Simulation Method

The simulation method, described in Section 4, was evaluated to see how robust it is in terms of changing some different variables. In the beginning of this chapter, the effects of the placement and volume of tracer are discussed for the RANS simulations using method T1. After that, the influence of the Schmidt number and the viscosity is examined. This investigation was performed using method T2 since this method accounts for the different properties of saline and water, which were not captured using method T1. Finally, the evaluation methods of the mixing time and the pumping number are discussed.

7.1 Volume of Tracer

A RANS simulation at 105 rpm using tracer method T1 with 24.6 litres of tracer was performed. This value corresponds to approximately 10% of the total water volume inside the tank, which corresponds to the tracer volume that has been used before in the existing simulation method at FS Dynamics. This simulation was compared to the RANS T1 simulation using 3.3 litres, in order to see how the mixing time is affected when using a larger volume of tracer. The tracer volumes are seen in Figure 7.1 and the results from the performed simulations are presented in Figure 7.2. The difference in mixing times is only about 1.4%, which is assumed negligible. Hence, it is not crucial to have exactly the right amount of tracer when using this method.

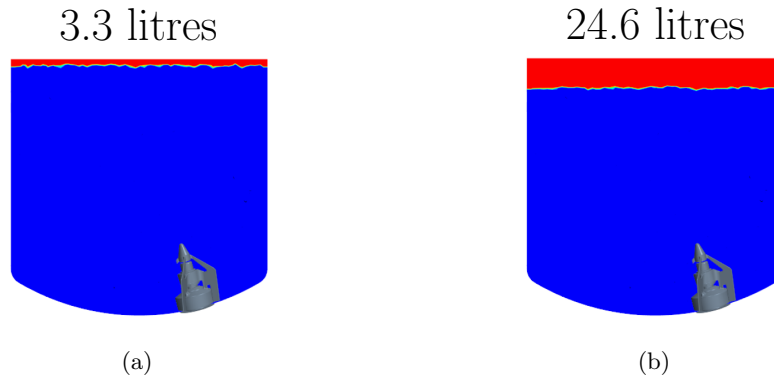


Figure 7.1: Visualization of the tracer amounts (a) 3.3 litres and (b) 24.6 litres, projected on a plane cutting through the center of the tank and impeller.

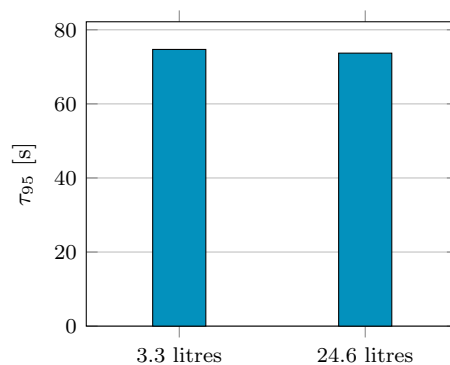


Figure 7.2: Mixing time for different tracer amounts from RANS simulations using method T1.

7.2 Shape and Placement of Tracer

Four different placements and shapes of tracer have been simulated using the RANS T1 method at 105 rpm to see how the mixing time is affected. How the mixing components are introduced in a real mixing case is not

always known, hence it is of interest to investigate the effect different initialization of tracer in the simulations has on the mixing time. The simulated tracer positions and shapes were based on how the pouring from the physical tests distributes the tracer into the domain. Four combinations have been tested, all with a volume of 3.3 litres:

- S1: A cylinder covering the whole top surface, see Figure 7.3a.
- S2: A cube placed in the middle, see Figure 7.3b.
- S3: A cube placed at the side above the impeller, see Figure 7.3c.
- S4: A cuboid placed at the side above the impeller that goes down to half the tank height, see Figure 7.3d.

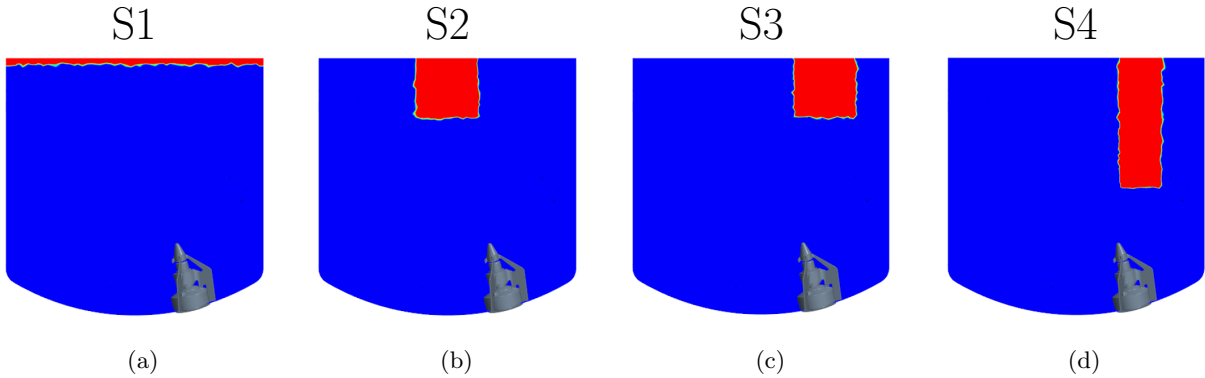


Figure 7.3: Visualization of the tracer placements (a) S1, (b) S2, (c) S3 and (d) S4, projected on a plane cutting through the center of the tank and impeller.

The mixing times for the different placements and shapes are shown in Figure 7.4, and pictures of the mixing process at every 6 seconds are found in Appendix E. The highest observed value corresponds to almost twice the size of the lowest value. It is therefore safe to conclude that the placement and shape of the tracer has a large impact on the mixing time. From S3 and S4, which are placed at the same location at the side of the tank, it is clear that the further down the placement is stretched, the faster the mixing is. Moving the placement of tracer a small amount, as for the cubes for case S2 and S3, does also affect the mixing time.

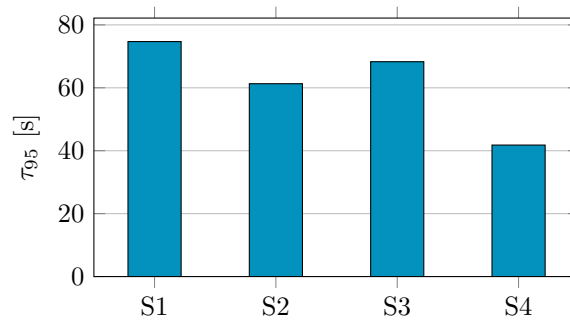


Figure 7.4: Mixing time for tracer placements S1-S4 for RANS simulations using method T1.

7.3 Influence of Schmidt Number and Viscosity

The Schmidt number is used when deciding the molecular diffusion of the mixture of liquids, according to Equation (2.42), which is used for the mass transport equation of the species in Equation (2.41). To investigate the effect of this parameter, results were compared for simulations performed for $Sc = 1$, $Sc = 450$ (corresponds approximately to self-diffusion of water) and $Sc = 8000$ (corresponds approximately to pure NaCl in water).

The simulations were performed using both RANS and LES methods, however $Sc = 450$ was not used in an LES simulation. The simulations were conducted at 105 rpm using method T2, mimicking the pouring of saline. The results are shown in Figure 7.5. For the RANS simulations, the difference is only 0.1 s between the maximum and minimum mixing time. For LES, $Sc = 8000$ gave 0.7 s longer mixing time than $Sc = 1$. Hence, the effects of different Schmidt numbers within the range of $Sc = 1$ to $Sc = 8000$ are deemed negligible.

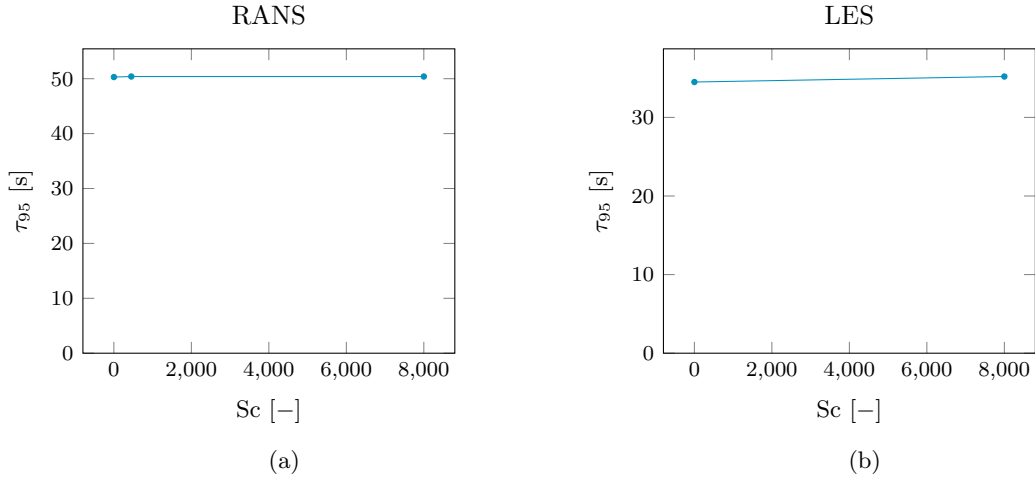


Figure 7.5: *Mixing times for different Schmidt numbers for (a) RANS simulations using method T2 and (b) LES simulations using method T2.*

In addition to the investigation of the influence of Schmidt number, a different viscosity was used for the simulation at $Sc = 1$ using the RANS method. For this simulation, a dynamic viscosity of $\mu = 0.8871 \cdot 10^{-3}$ kg/ms was used for both tracer and water. For the other Schmidt numbers, $\mu = 1.676 \cdot 10^{-3}$ kg/ms was used for the tracer (corresponding to approximately 22% mass concentration of salt in water at 20°C[17]), and $\mu = 0.9532 \cdot 10^{-3}$ kg/ms was used for water (corresponding to the viscosity of water at 22°C[20]). As stated above, the difference between the mixing times for different Schmidt numbers is negligible. Since no change in results occurred for different viscosities, this parameter is also deemed to have a negligible effect on the mixing times in the tested range.

7.4 Evaluation of Mixing Time

In this study, 95% mixing time was taken as the time for the coefficient of variance to reach 0.05, which was proposed by Kukukova et al.[13]. However, the two other methods for calculating global mixing time discussed in Section 2.2.7 have been evaluated as well.

One of these other methods was proposed by Hartmann et al.[11], who took 95% mixing from $CV = 0.0283$. Mixing time results for all performed simulations using both $CV = 0.05$ and $CV = 0.0283$ are presented in Figure 7.6 together with the results from the physical testing. The mixing times using $CV = 0.0283$ are approximately 15-20% longer than using $CV = 0.05$. Both evaluations of mixing time corresponds well to the physical tests when using LES. LES simulations using $CV = 0.05$ slightly underpredicts the mixing time for the two lower velocities, whereas using $CV = 0.0283$ slightly overpredicts the time for the two higher velocities. It can be argued that using $CV = 0.0283$ would be too conservative when comparing the global mixing time with an average of two local mixing times from the physical tests. Hartmann et al.[11] based the value of CV on a numerical experiment, by taking statistically independent values between 0.95 and 1.05 and then calculating the CV . This was repeated several times and the CV was averaged, giving the resulting value of 0.0283. Hence, using $CV = 0.0283$ would correspond more to taking the longest local mixing time from the physical tests, instead of an average, since the numerical experiment performed by Hartmann et al.[11] is more comparable to when the concentrations at all locations are between $0.95 \cdot \bar{c}_t$ and $1.05 \cdot \bar{c}_t$.

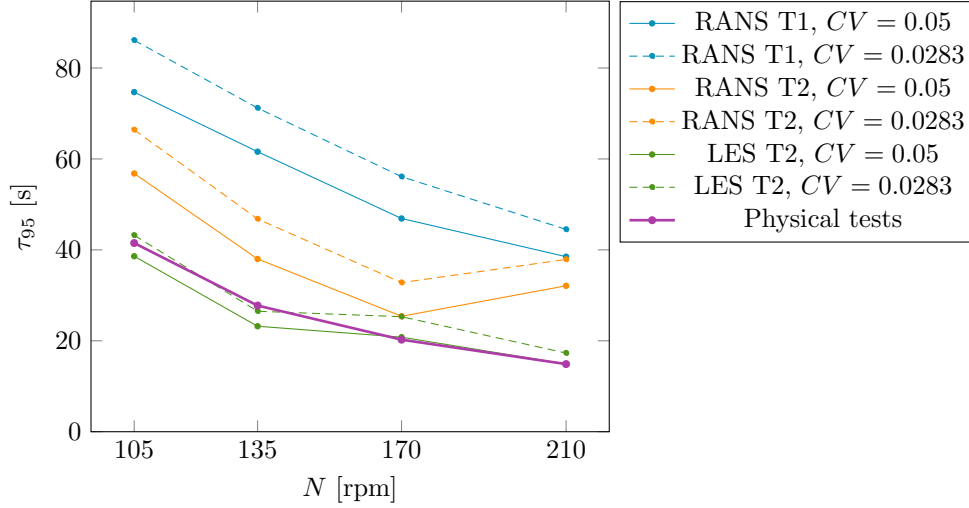


Figure 7.6: Global mixing time using $CV = 0.05$ (solid lines) and $CV = 0.0283$ (dashed lines) for RANS and LES simulations together with the average of the two local mixing times from physical tests, for all four rotational speeds.

Another option of global mixing time evaluation is to take the time it takes for all cells to reach a concentration between $0.95 \cdot \bar{c}_t$ and $1.05 \cdot \bar{c}_t$, proposed by Yeoh et al.[24]. Results using this method, together with both methods using coefficient of variance are presented in Figure 7.7 for LES simulations at 105 rpm using two different meshes with different cell counts. From these results, it is seen that this method is even more conservative than using $CV = 0.0283$. Furthermore, it is also seen that the method of tracking the global maximum and minimum concentrations is highly mesh dependent. The finer mesh gave 20% longer mixing time than the regular mesh, compared to the methods using CV which gave 1.7% and 1.4% longer mixing time for the fine mesh for $CV = 0.0285$ and $CV = 0.05$ respectively. This is probably due to that local variations in the tank are better captured by a finer mesh, allowing for more extreme values at small cells. In the same way as it can be argued that using $CV = 0.0283$ would be too conservative when comparing to an average of two local mixing times from physical tests, using the maximum and minimum concentrations method should be compared to taking the maximum time from the physical testing as well.

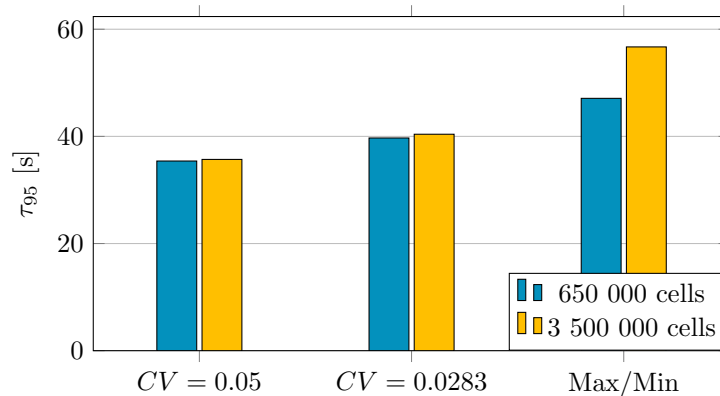


Figure 7.7: The three different methods of evaluating global mixing time from LES simulations using meshes containing 650 000 and 3 500 000 cells. Results taken from the rotational speed of 105 rpm.

Note that the meshes used in Figure 7.7 are taken from the LES mesh study, presented in Table 5.9, before changing the prism layer settings in the final meshes. Hence, the results differ slightly from the ones presented in Section 6.2, but it is the overall trend that is of interest here, not the exact values.

7.5 Evaluation of Pumping Number

The pumping number is calculated using Equation (2.49), which is dependent on the impeller swept area. Since the geometry of the Metenova ZG5 Magnetic mixer is different from a purely radial impeller, the definition of the impeller swept area is not straightforward. The area is defined as a cylinder with a radius of 80 mm, without any top or bottom surface. At first, the height was chosen such that the whole impeller was enclosed in the cylinder. From a RANS simulation performed at 105 rpm, it was seen that the flow was both going into the cylinder at the upper part and out from the lower part. This gave a low volume net flux, which would give a too low pumping number. To circumvent this problem, different heights of the cylinder were evaluated and the one giving the most volume flux was chosen as the impeller swept area. A plot of pumping numbers from the different heights can be seen in Figure 7.8. The curve has a maximum at 60 mm, hence the cylinder used as the impeller swept area has a height of 60 mm.

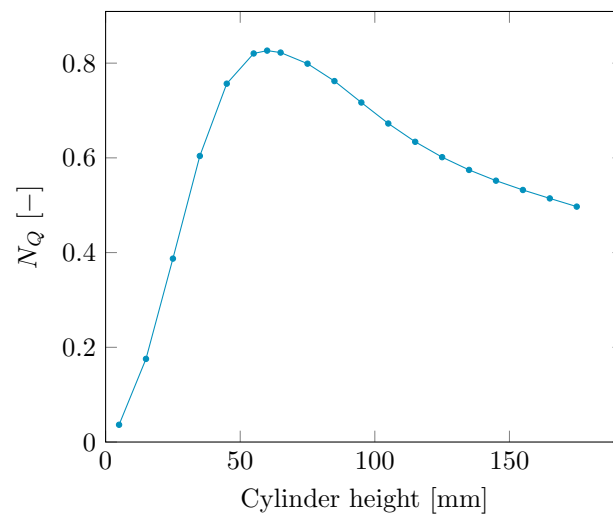


Figure 7.8: *Pumping number for different heights of the cylinder representing the impeller swept area.*

8 Conclusions and Future Work Recommendations

The purpose of this thesis was to improve and validate an existing method used for CFD simulations of active mixing applications. During this study, the simulation method has been extended by implementing LES as turbulence model, as well as developing a new method for introducing the tracer in a more physical manner. Physical tests have been performed and used for validation, and the simulation method has been evaluated by changing some of the properties of the mixing components. The main conclusions drawn from this study are presented below, together with some recommendations for future work.

Regarding guidelines for creating a mesh for these types of simulations, it can be concluded that a mesh containing approximately one million cells is sufficient for a domain of the used tank size. If wall functions are used, the first cell should be located such that the average y^+ values on the impeller and tank walls are above 15.

The mixing times from LES simulations agree well with the performed experiments. Hence, using this type of LES with wall functions seems to work well in this application. By not resolving the whole boundary layer, the computational demand for the LES was held low enough to be a possible method to use if high accuracy is needed. The RANS simulations using method T2 overpredict the mixing time by 50% when compared to the physical tests, and require less than 1/3 of the CPU hours as compared to the LES at 105 rpm.

The two methods used for introducing the tracer result in different mixing processes. For method T1, the tracer is mixed from the top of the domain and downwards. For method T2, the tracer gathered in the bottom of the tank due to the higher density and the velocity at the inlet and is then mixed upwards. This difference in mixing processes and the observed difference in mixing time concludes that method T1 is not an appropriate method to use for evaluating mixing times and processes in this type of set up. However, for cases where it is unknown how the different mixing components are introduced or only a relative comparison between two or more setups are of interest, method T1 can still be an appropriate method to use since it is general and fast.

When using method T1, the results indicate that increasing the total volume of the tracer from 3.3 litres to 24.6 litres does not influence the mixing time when it is placed as a cylinder covering the whole top surface. However, if the shape and placement of the tracer are changed, the mixing time is affected.

As concluded in the previous two paragraphs, the initialization of tracer affects the results substantially. Hence, it is of importance to know how the real mixing procedure is conducted in order to get an accurate prediction of both mixing time and mixing process.

Both the RANS and LES simulations underpredict the power number as compared to the physical tests, by 20% and 15% respectively. Regarding the pumping number, the results from the LES simulations do not agree with the results from the RANS simulations. Hence, the chosen method for determining the impeller swept area for the pumping number should probably be re-evaluated.

The mixing times are not affected if the Schmidt number is changed within the range of $Sc = 1$ to $Sc = 8000$ or when changing the dynamic viscosity of the tracer within the range of 0.8871 – 1.676 kg/ms.

The method of calculating the mixing time by tracking the maximum and minimum concentrations in the tank is not recommended, since it was concluded that it is too mesh sensitive. Two other methods using CV to evaluate mixing time have been discussed. Which method that should be applied for evaluating τ_{95} depends on how the condition for 95% homogeneity of tracer concentration is defined. For the physical tests performed in this study, 95% mixing was estimated by taking an average of two local mixing times. Hence a similar estimation was used for the simulation results, where using $CV = 0.05$ could be compared to an average value of 95% mixing in the whole tank. However, if the 95% homogeneity is defined from having the conditions in the whole tank at at least 95%, this would rather correspond to using $CV = 0.0283$ and taking the maximum local mixing time from the physical tests.

Some recommendations for future work have been thought of during this project. These are listed below, in no particular order:

- Evaluate what influence the size of the rotational region has on the solution.
- Investigate how the impeller swept area should be defined for calculating the pumping number in a better way.
- Investigate the possibility to combine the MRF and SM methods. By applying a small part of the rotation using SM and the rest with an MRF, some of the accuracy of actually rotating the impeller will be gained while still having a less demanding method than pure SM. If this was to be used in an LES, a larger time step may be used which would require less CPU time.
- Perform several LES simulations with the same settings to investigate the identified variation of mixing times.
- Compare different RANS turbulence models to see if it has any impact on the results.
- Explore the possibilities of using a second order temporal discretization scheme for the RANS simulations. However, if this requires a smaller time step due to stability reasons, it will result in a longer CPU time.
- Evaluate the performance of the simulation method when used in other setups. For example, include particles or change the geometry, water level and rotational speed.

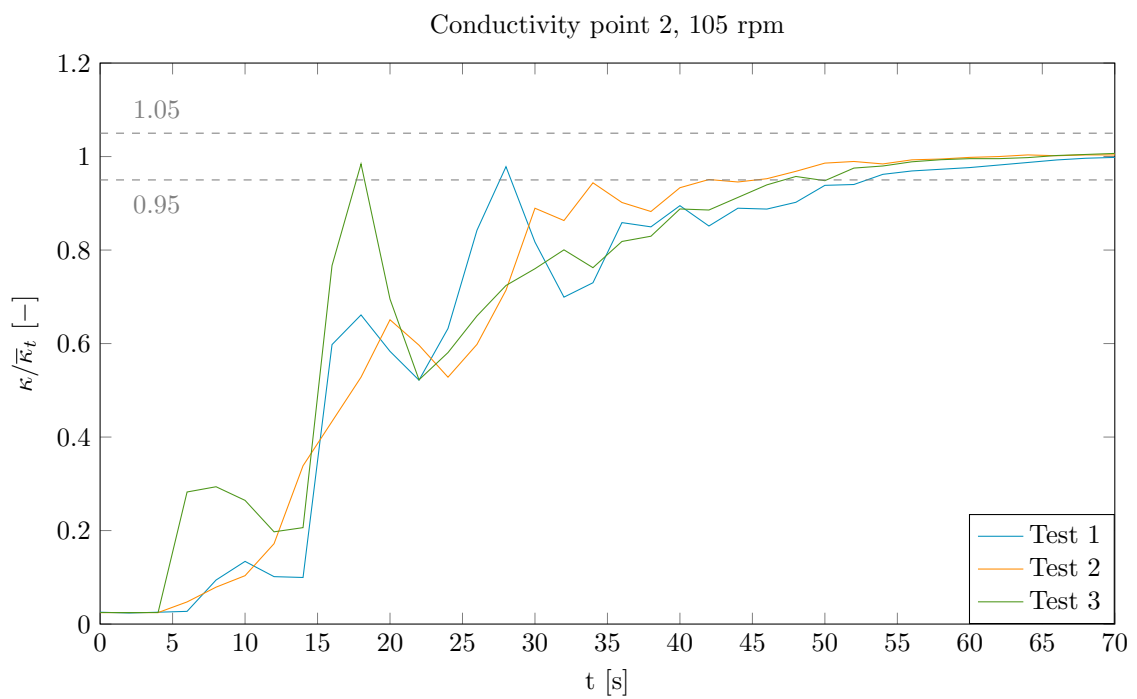
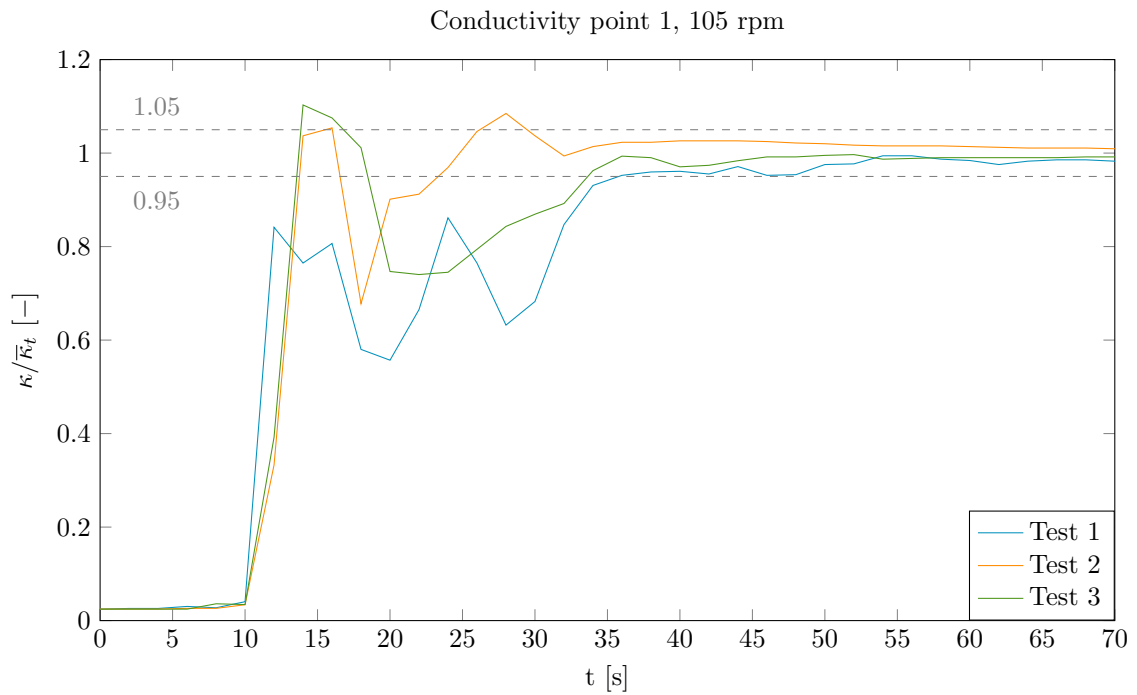
References

- [1] J. D. Anderson. *Computational fluid dynamics : The basics with applications*. McGraw-Hill, 1995. ISBN: 0-07-001685-2.
- [2] B. Andersson et al. *Computational Fluid Dynamics for Engineers*. Cambridge University Press, 2012. ISBN: 9781107018952.
- [3] G. Ascanio. “Mixing time in stirred vessels: A review of experimental techniques”. In: *Chinese Journal of Chemical Engineering* 23.7 (2015), pp. 1065–1076. DOI: 10.1016/j.cjche.2014.10.022.
- [4] Z. Chara et al. “Study of fluid flow in baffled vessels stirred by a Rushton standard impeller”. In: *Applied Mathematics and Computation* 272.3 (2016), pp. 614–628. DOI: 10.1016/j.amc.2015.06.044.
- [5] A. Corsini, G. Delibra, and A. G. Sheard. “A Critical Review of Computational Methods and Their Application in Industrial Fan Design”. In: *ISRN Mechanical Engineering* 2013 (2013). DOI: 10.1155/2013/625175.
- [6] L. Davidson. *Fluid mechanics, turbulent flow and turbulence modeling*. Chalmers University of Technology, 2018.
- [7] A. Delafosse et al. “LES and URANS simulations of hydrodynamics in mixing tank: Comparison to PIV experiments”. In: *Chemical Engineering Research and Design* 86.12 (2008), pp. 1322–1330. DOI: 10.1016/j.cherd.2008.07.008.
- [8] S. Hall. *Rules of thumb for chemical engineers*. Elsevier Science & Technology, 2012. ISBN: 9780128110379.
- [9] C. Haringa, R. Vandewijer, and R. F. Mudde. “Inter-compartment interaction in multi-impeller mixing: Part I. Experiments and multiple reference frame CFD”. In: *Chemical Engineering Research and Design* 136 (2018), pp. 870–885. DOI: 10.1016/j.cherd.2018.06.005.
- [10] C. Haringa, R. Vandewijer, and R. F. Mudde. “Inter-compartment interaction in multi-impeller mixing. Part II. Experiments, sliding mesh and large eddy simulations”. In: *Chemical Engineering Research and Design* 136 (2018), pp. 886–899. DOI: 10.1016/j.cherd.2018.06.007.
- [11] H. Hartmann, J. J. Derksen, and H. E. van den Akker. “Mixing times in a turbulent stirred tank by means of LES”. In: *AICHE Journal* 52.11 (2006), pp. 3696–3706. DOI: 10.1002/aic.10997.
- [12] S. M. Kresta et al. *Advances in Industrial Mixing - A Companion to the Handbook of Industrial Mixing*. John Wiley & Sons, 2017. ISBN: 978-1-5231-0992-0.
- [13] A. Kukukova et al. “Impact of sampling method and scale on the measurement of mixing and the coefficient of variance”. In: *AICHE Journal* 54.12 (2008), pp. 3068–3083. DOI: 10.1002/aic.11639.
- [14] N. A. Lange. *Lange’s Handbook of Chemistry*. Ed. by J. A. Dean. 15th ed. McGraw-Hill, Inc, 1999. Chap. 5, p. 86. ISBN: 0-07-016384-7.
- [15] L. Li and B. Xu. “CFD Simulation of local and global mixing time in an agitated tank”. In: *Chinese Journal of Mechanical Engineering* 30.1 (2017), pp. 118–126. DOI: 10.3901/CJME.2016.1107.129.
- [16] V. X. Mendoza-Escamilla et al. “Assessment of k- models using tetrahedral grids to describe the turbulent flow field of a PBT impeller and validation through the PIV technique”. In: *Chinese Journal of Chemical Engineering* 26.5 (2018), pp. 942–956. DOI: 10.1016/j.cjche.2018.02.012.
- [17] J. R. Rumble. *CRC Handbook of Chemistry and Physics*. 99th ed. CRC Press, 2018. ISBN: 9781138561632.
- [18] *Simcenter. STAR-CCM+*. Version 13.04.010. Siemens PLM Software.
- [19] R. Smith. *Moving Reference Frame for Computational Fluid Dynamics*. URL: <https://www.symscape.com/blog/moving-reference-frame-for-cfd>.
- [20] E. Toolbox. *Water - Dynamic and Kinematic Viscosity*. URL: https://www.engineeringtoolbox.com/water-dynamic-kinematic-viscosity-d_596.html.
- [21] I. Torotwa and C. Ji. “A Study of the Mixing Performance of Different Impeller Designs in Stirred Vessels Using Computational Fluid Dynamics”. In: *Designs* 2.1 (2018), p. 10. DOI: 10.3390/designs2010010.
- [22] H. K. Versteeg and W. Malalasekera. *An introduction to computational fluid dynamics: the finite volume method*. Pearson Education Limited, 2007. ISBN: 978-0-13-127498-3.
- [23] M. Wolfstein. “The velocity and temperature distribution in one-dimensional flow with turbulence augmentation and pressure gradient”. In: *International Journal of Heat and Mass Transfer* 12 (1969), pp. 301–318. DOI: 10.1016/0017-9310(69)90012-X.
- [24] S. L. Yeoh, G. Papadakis, and M. Yianneskis. “Determination of mixing time and degree of homogeneity in stirred vessels with large eddy simulation”. In: *Chemical Engineering Science* 60.8 (2005), pp. 2293–2302. DOI: 10.1016/j.ces.2004.10.048.

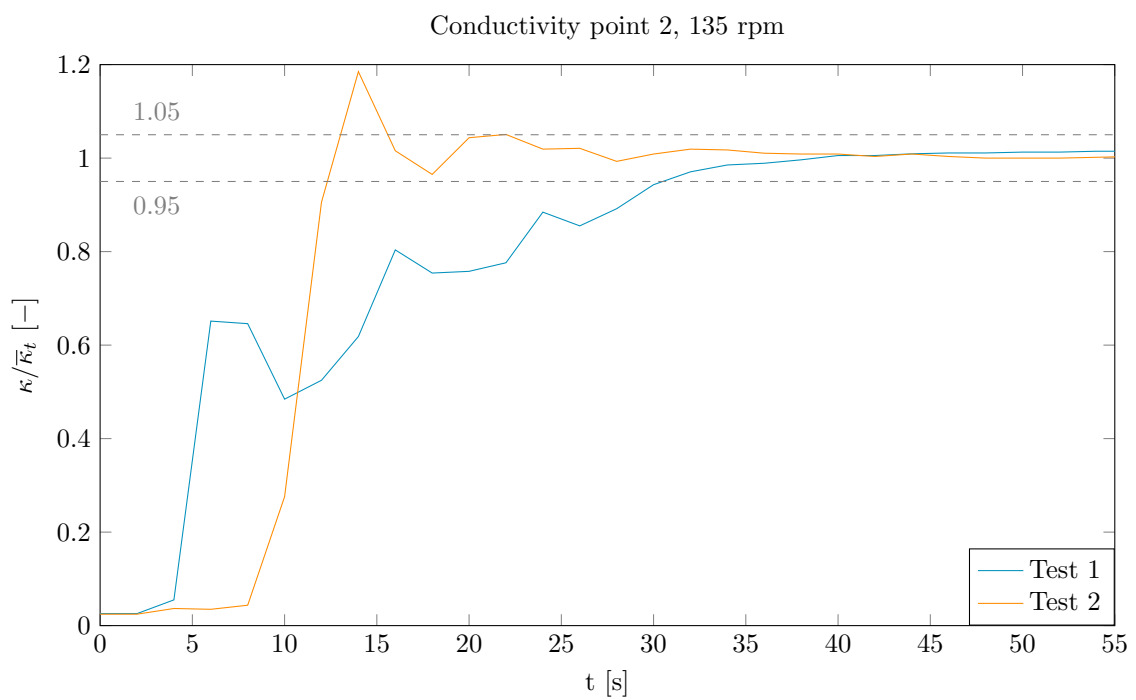
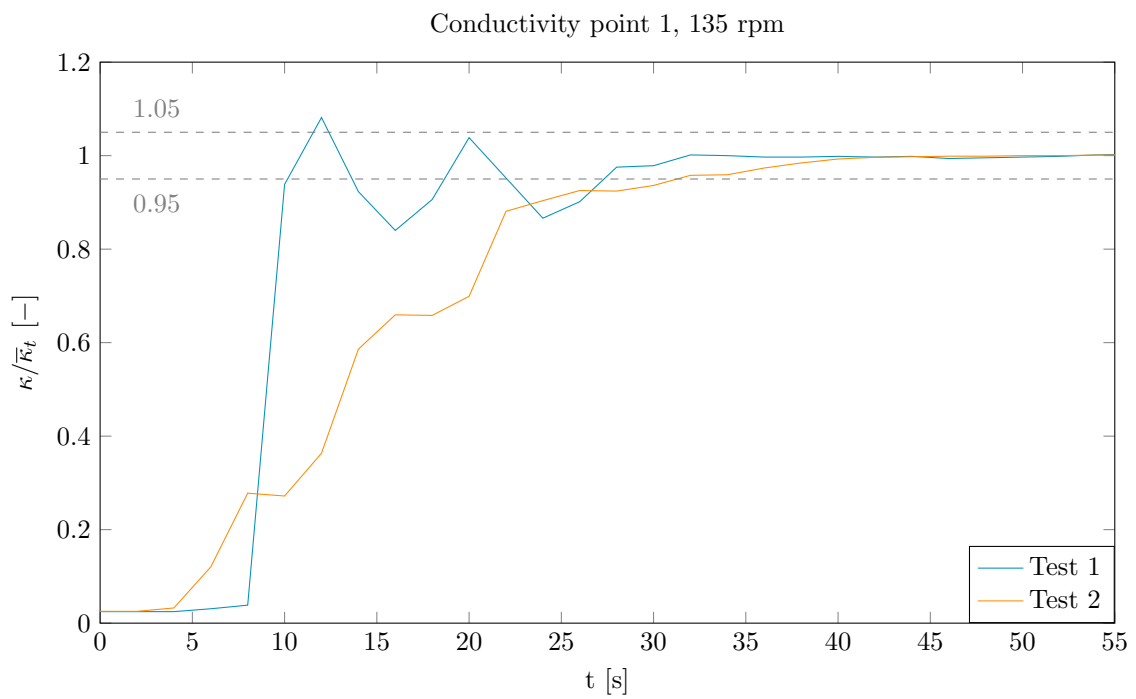
Appendices

A Conductivity curves from physical testing

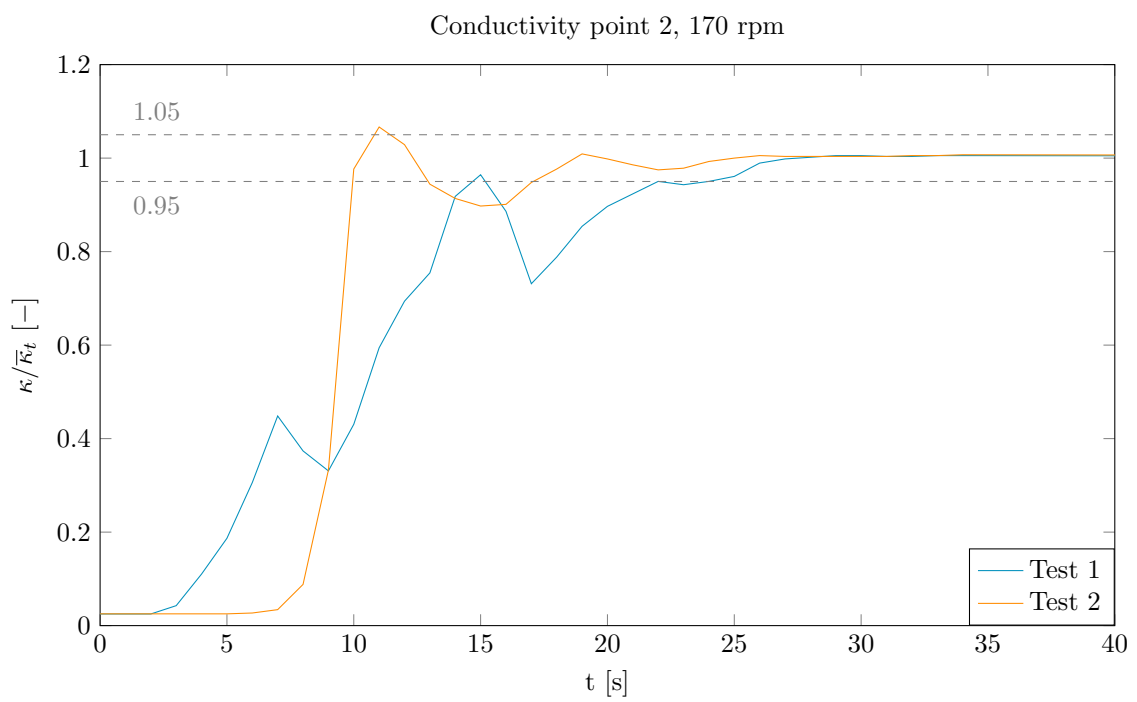
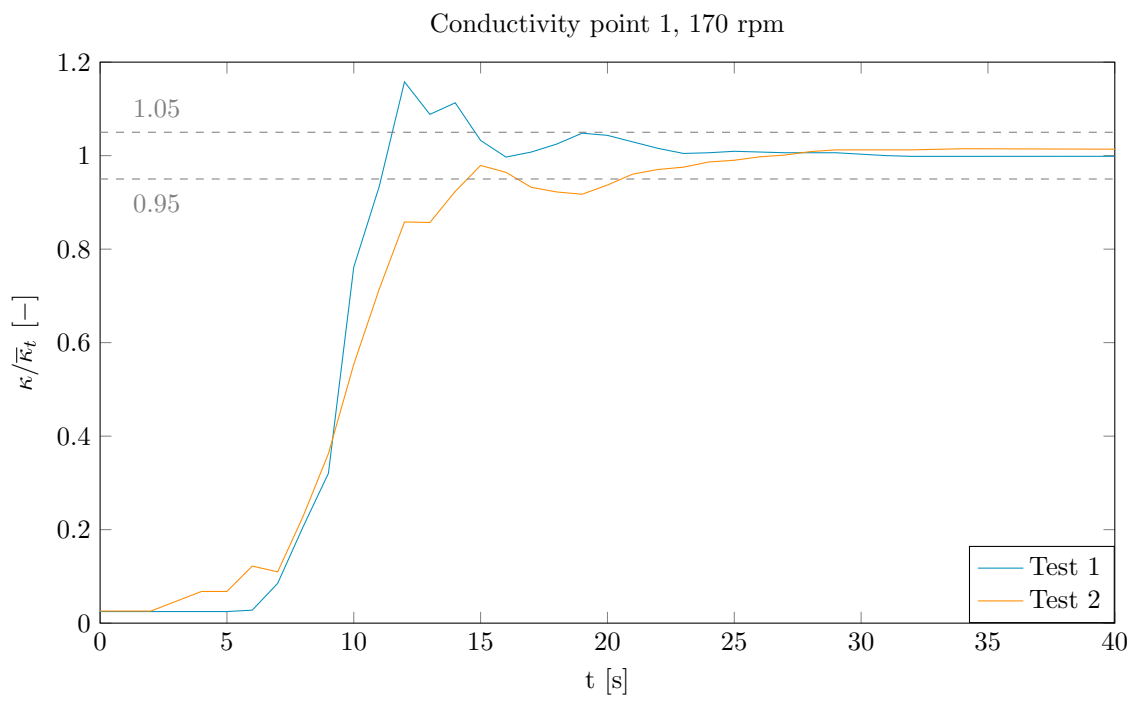
A.1 105 rpm



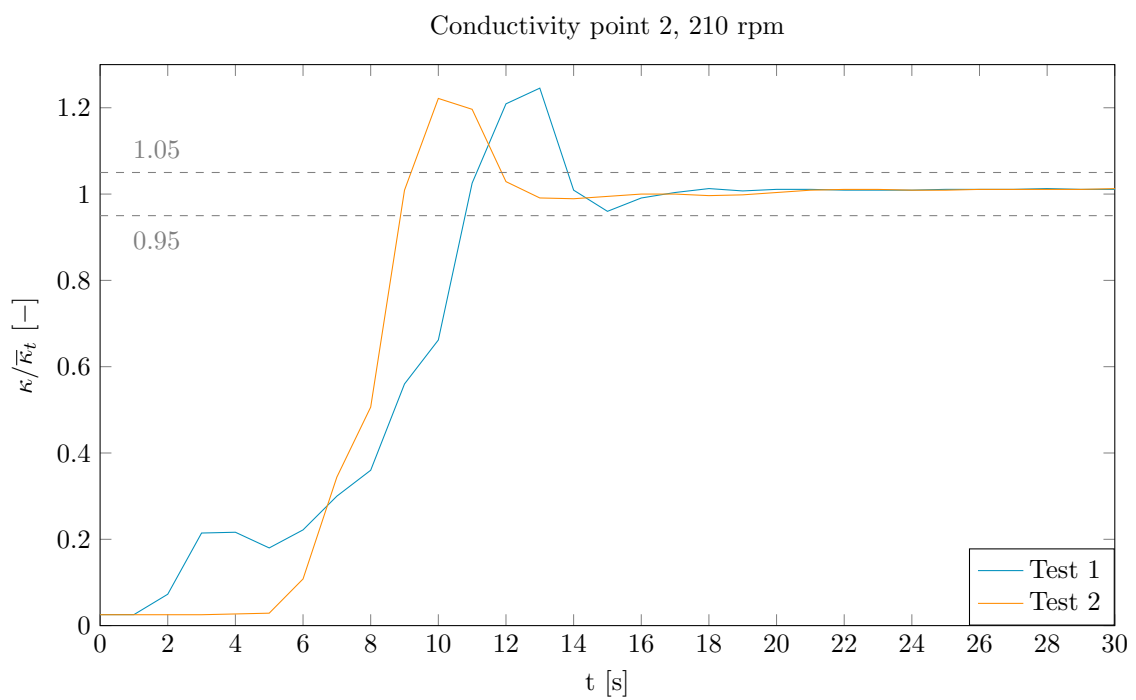
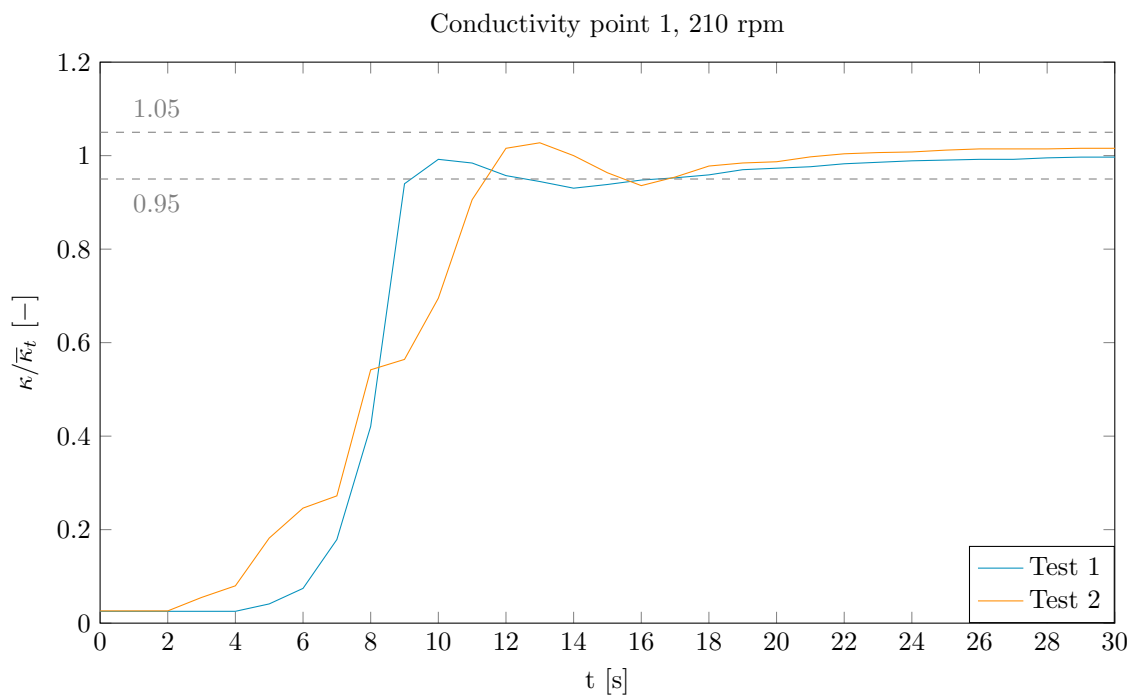
A.2 135 rpm



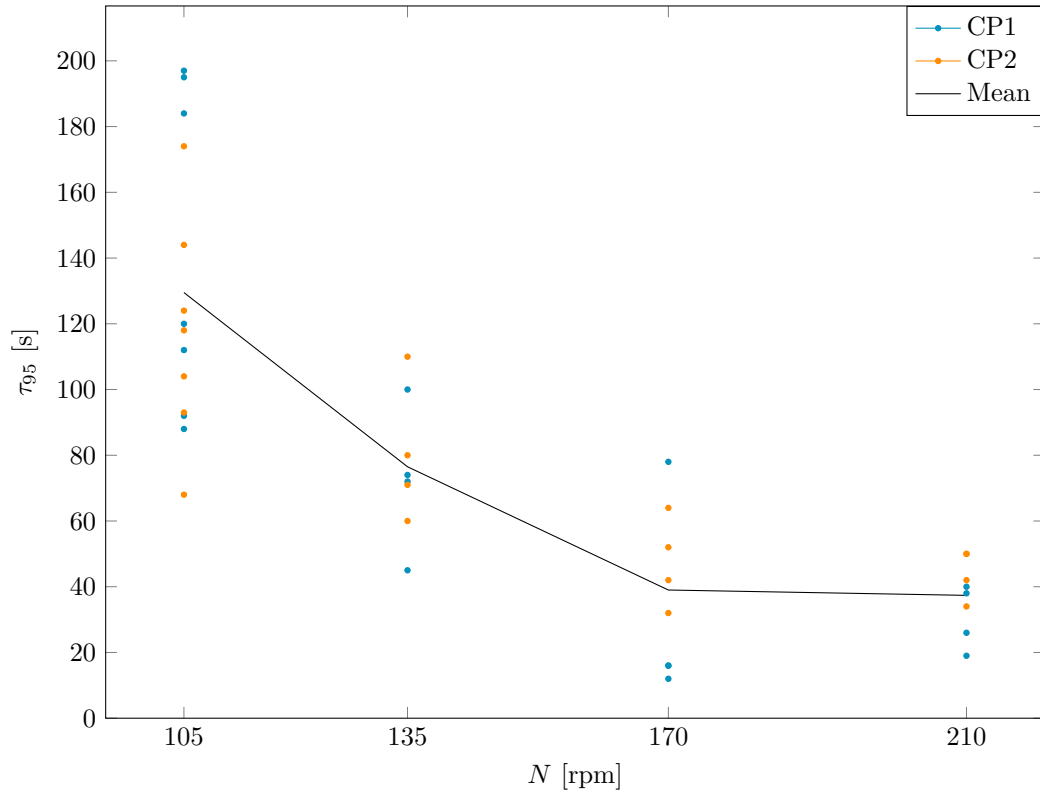
A.3 170 rpm



A.4 210 rpm



B Results from physical testing using vertical alignment of conductivity probes

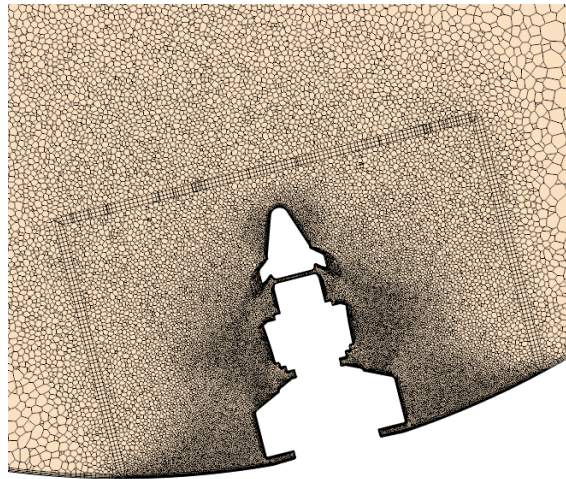
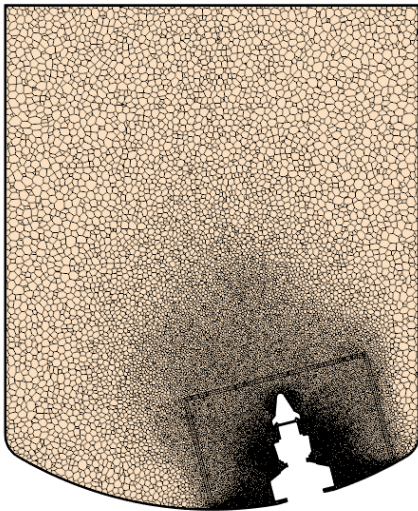


C Meshes

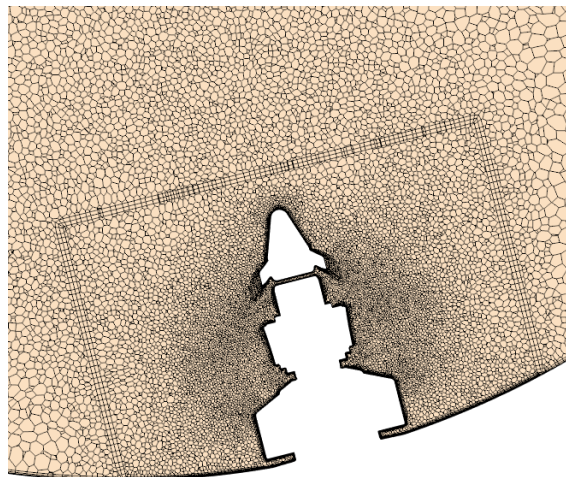
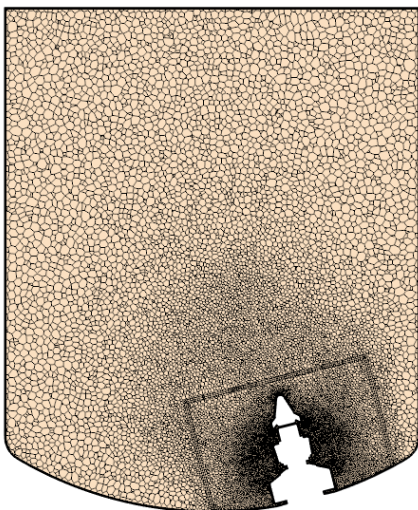
C.1 RANS - Mesh study

C.1.1 RANS - A: Rotational region

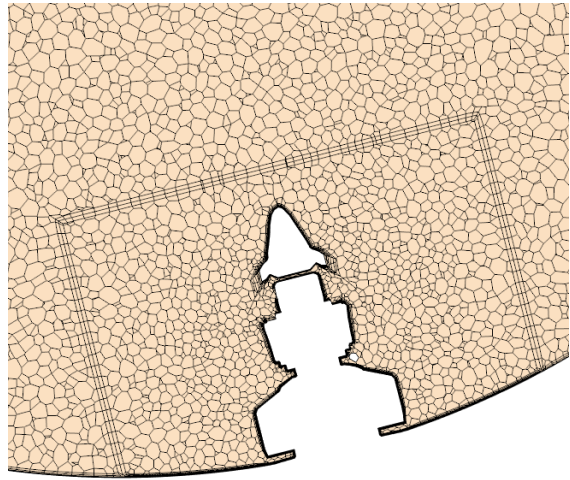
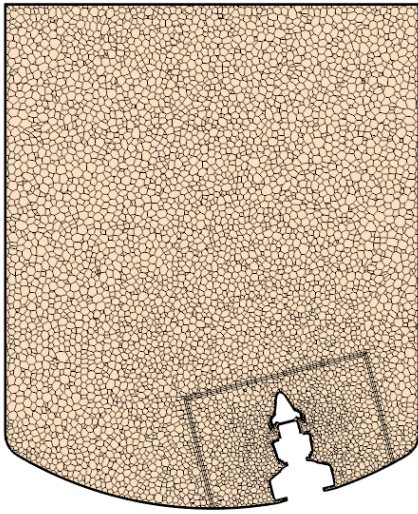
A1



A2

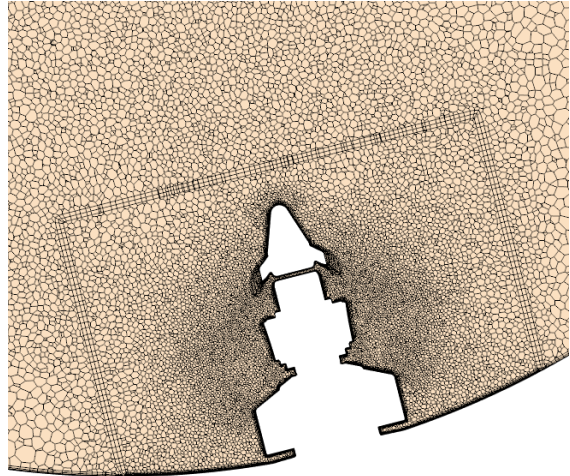
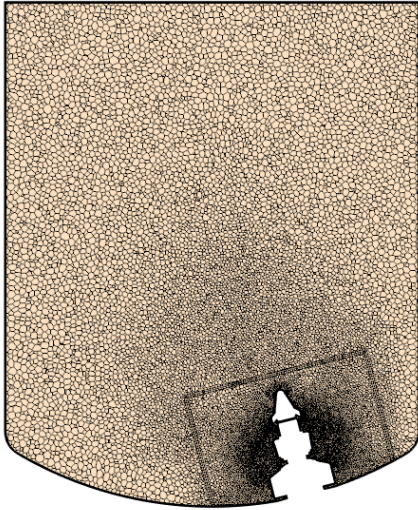


A5

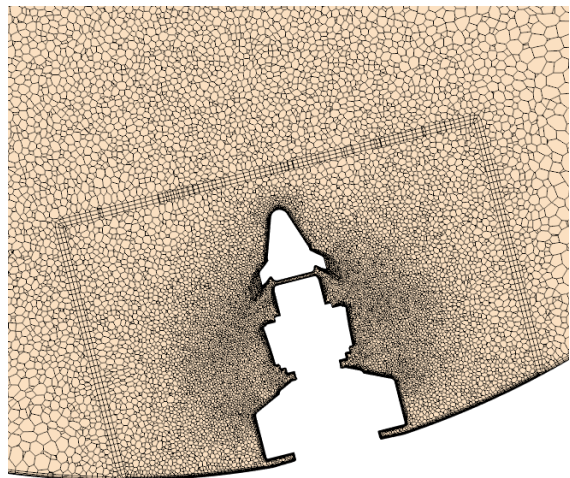
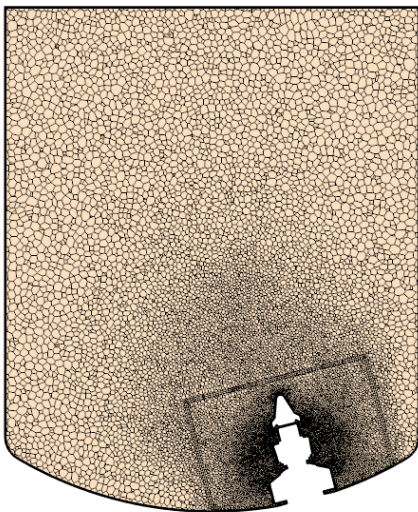


C.1.2 RANS - B: Stationary region

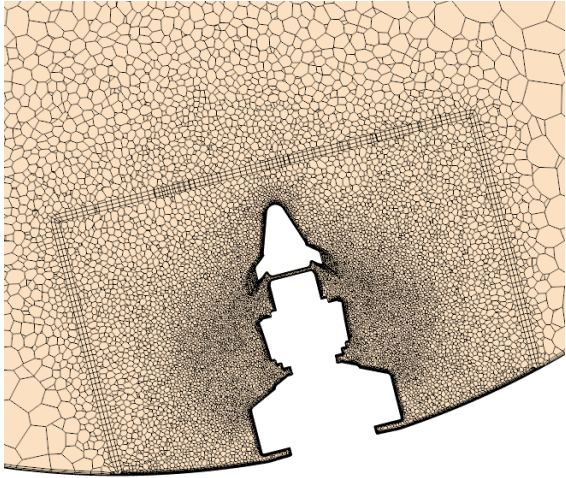
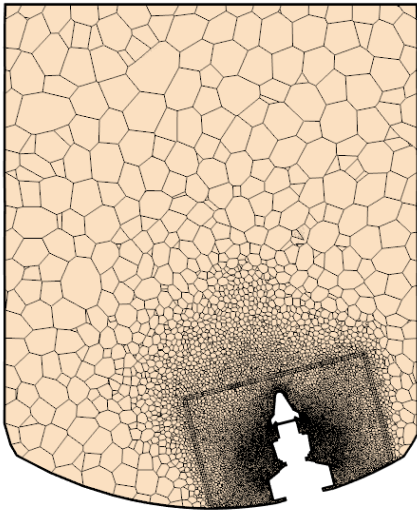
B1



B2

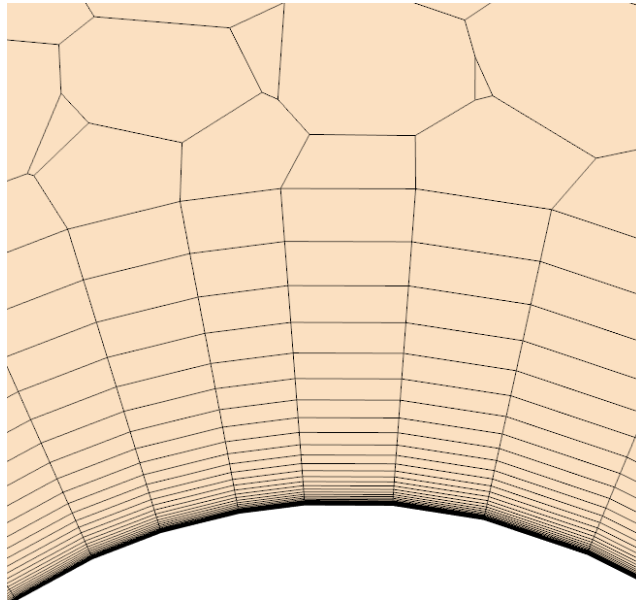


B4

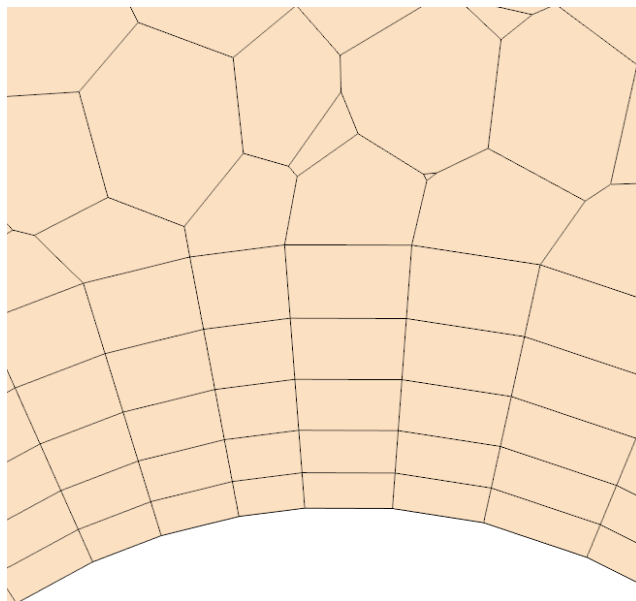


C.1.3 RANS - C: Boundary layer

Resolved boundary layer

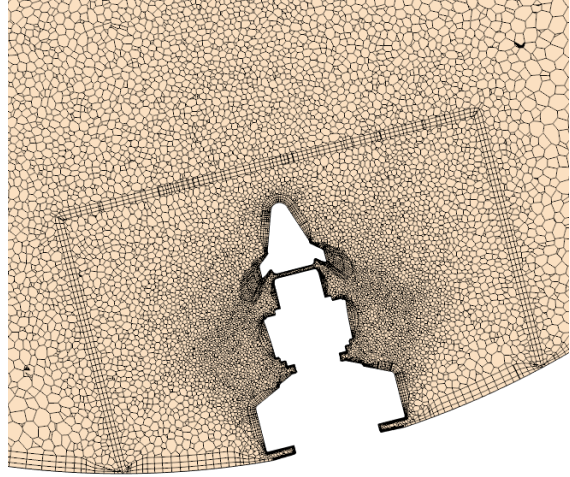
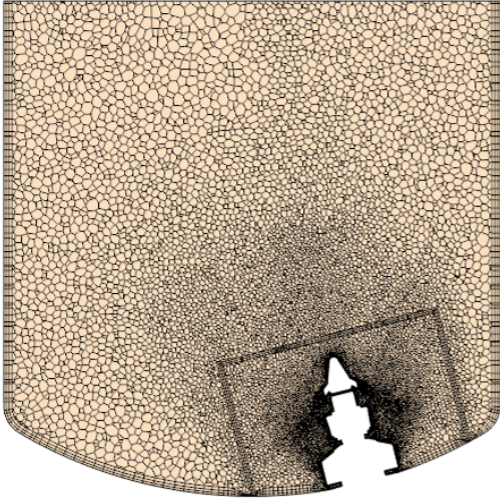


C4

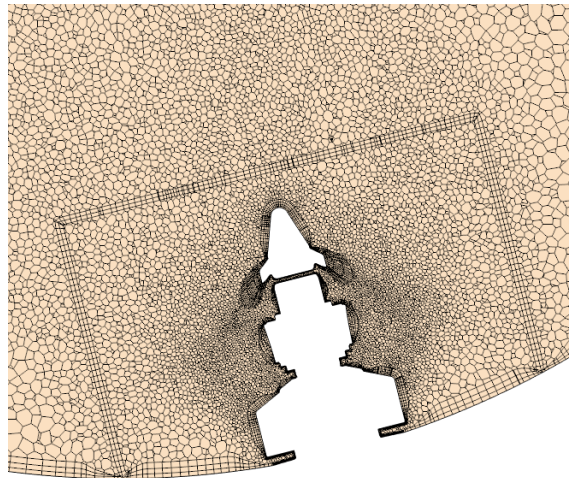
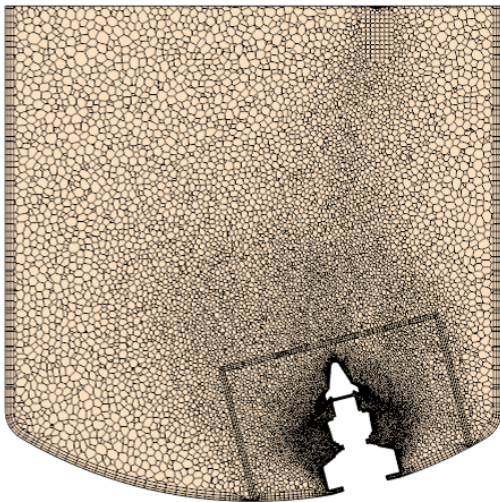


C.2 RANS - Final meshes

T1

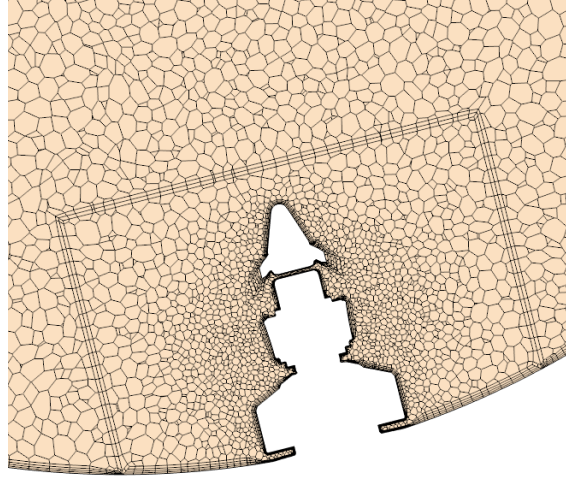
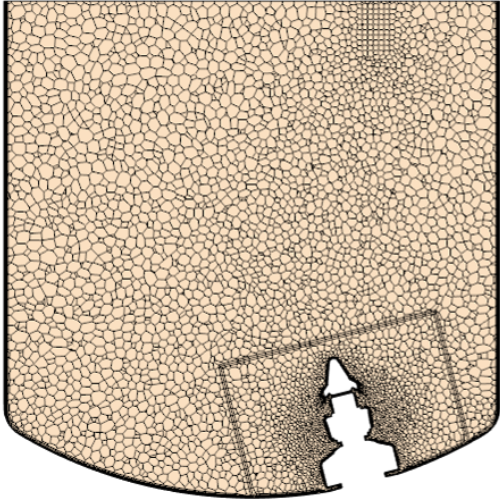


T2

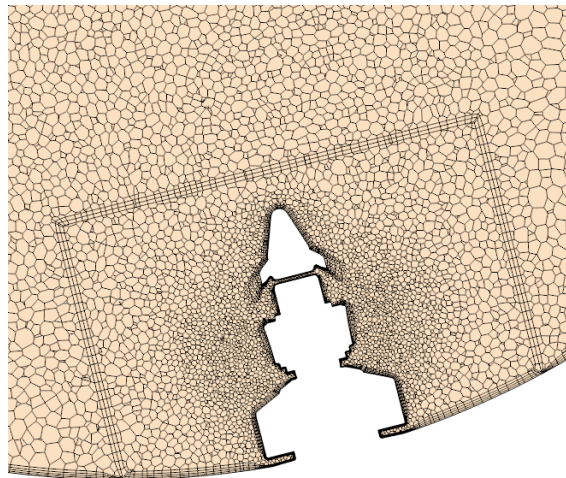
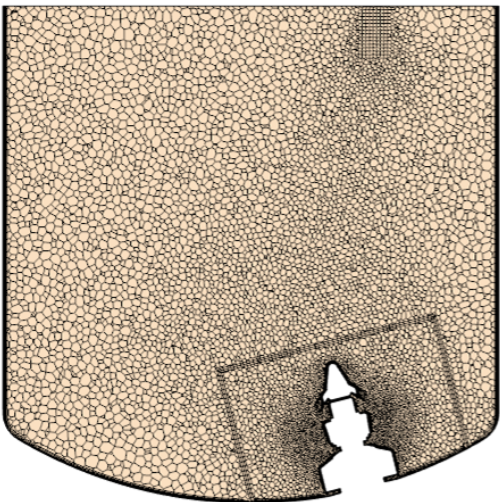


C.3 LES - Mesh study

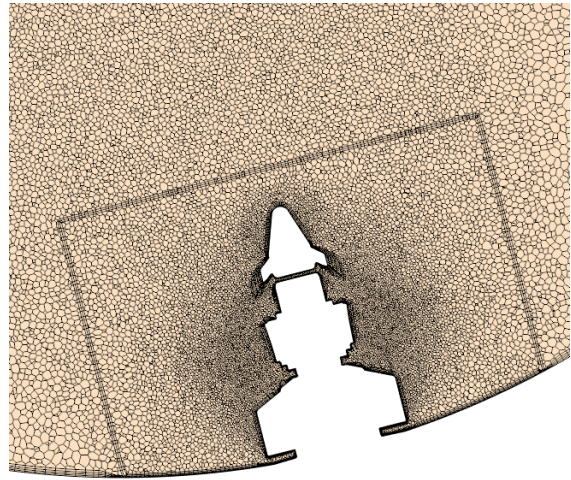
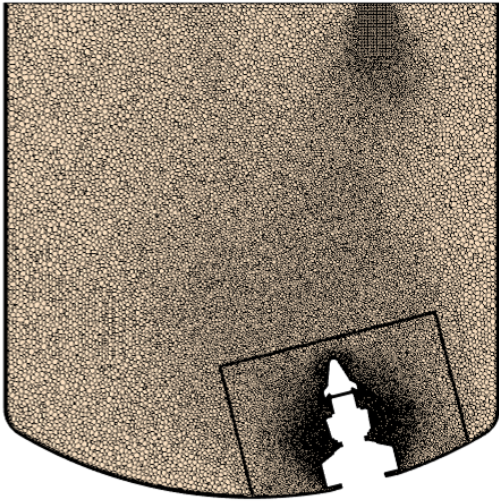
Coarse



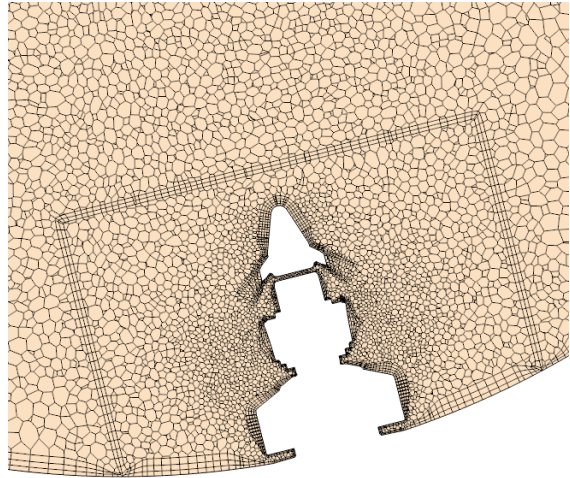
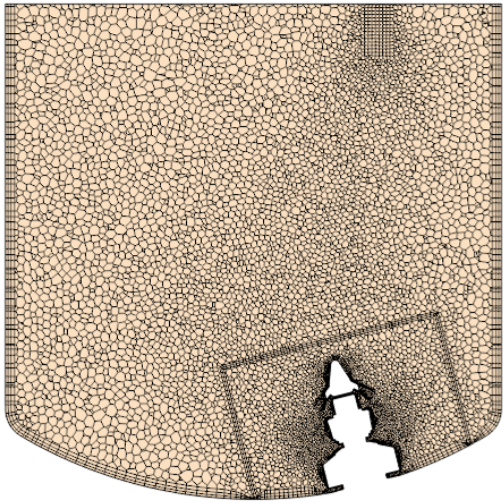
Base



Fine

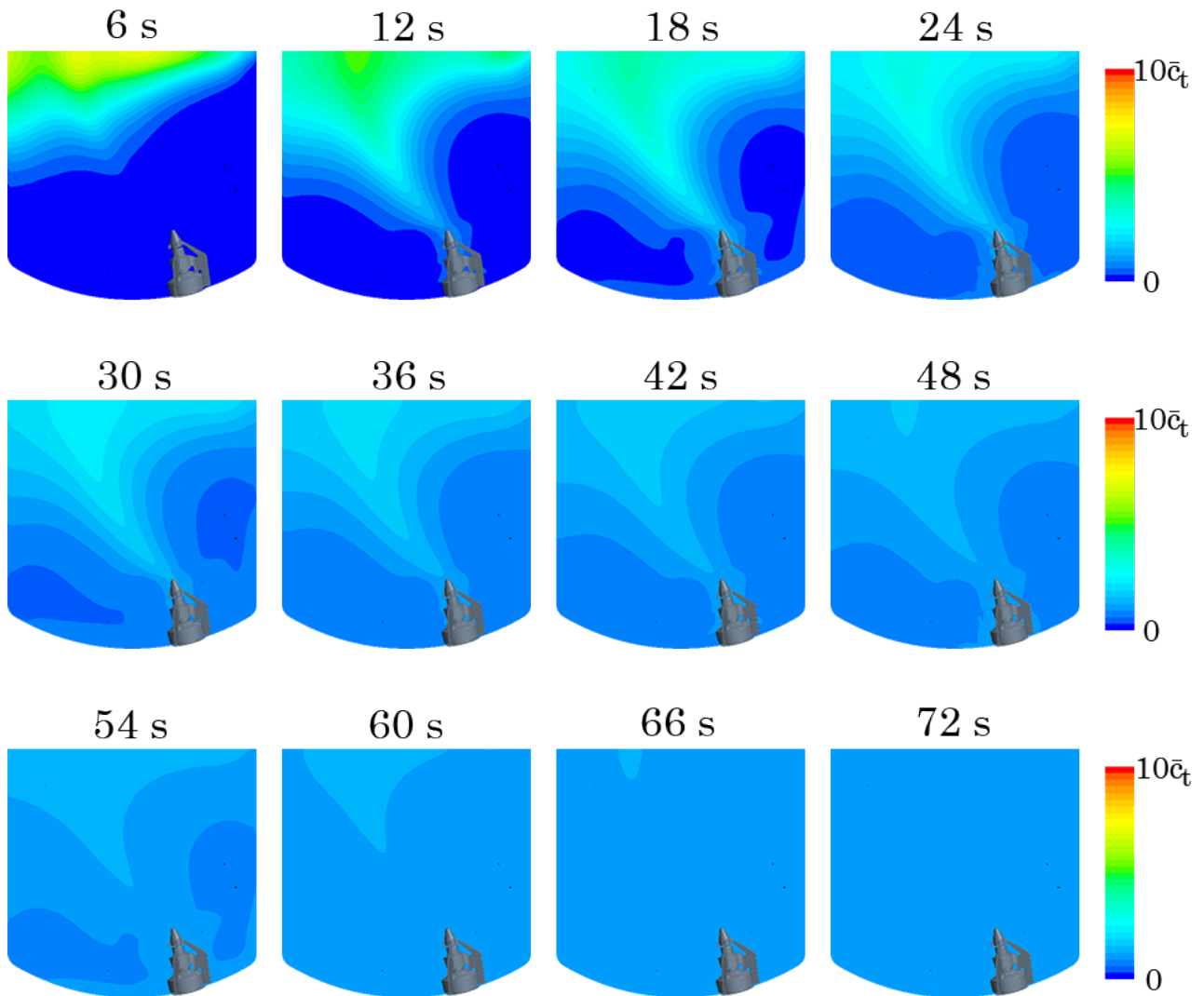


C.4 LES - Final mesh

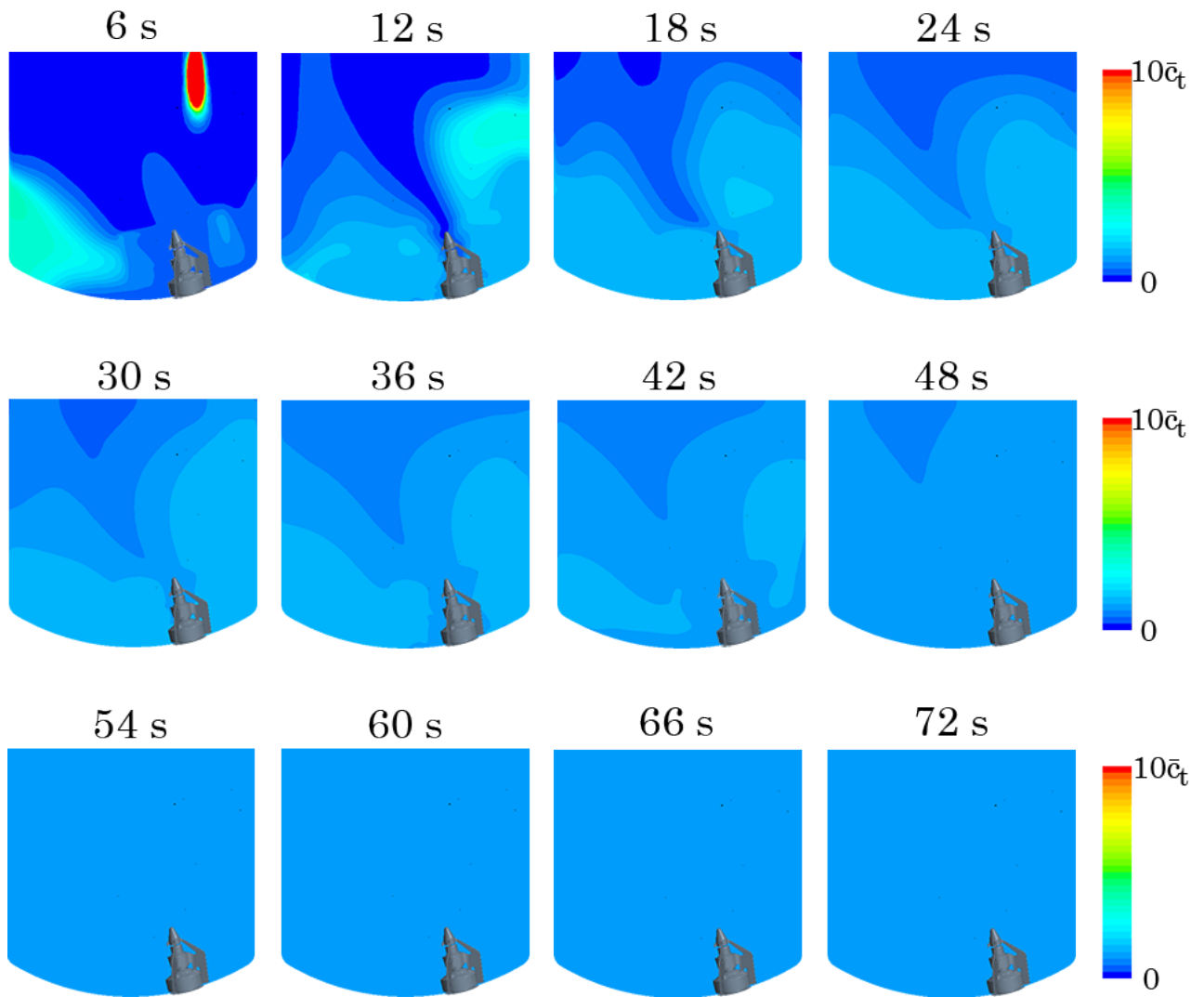


D Mixing process at 105 rpm

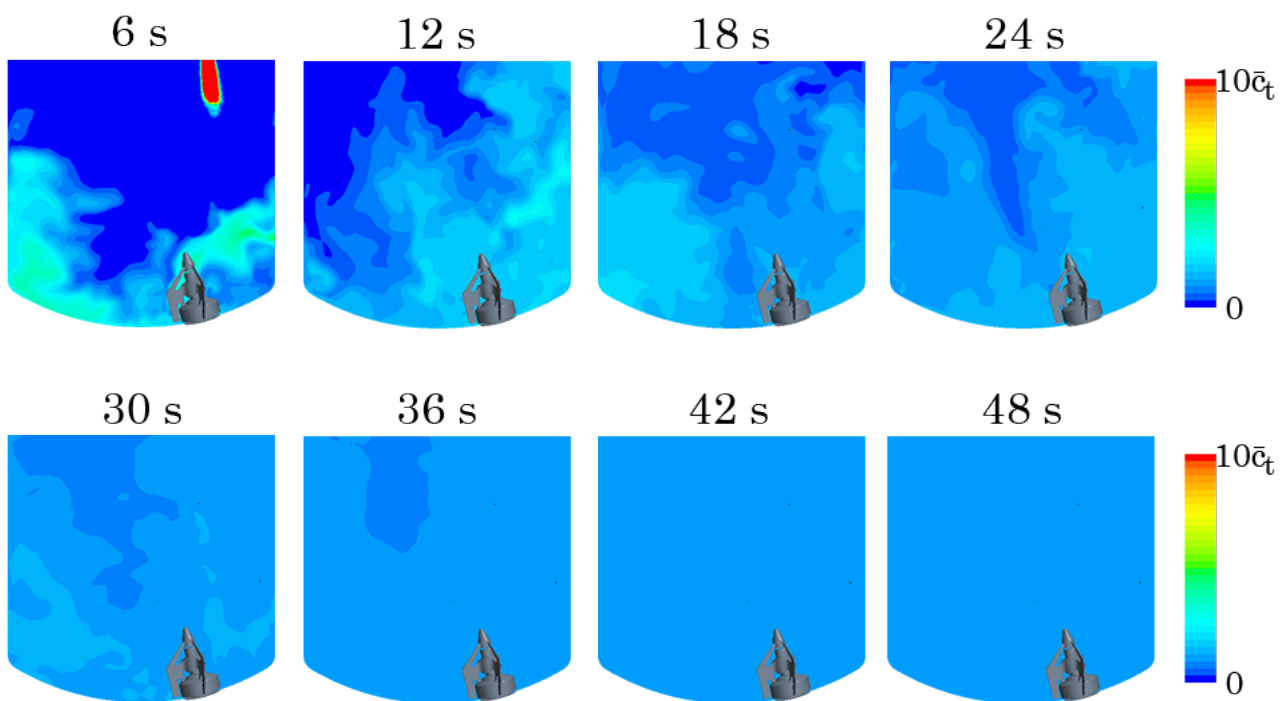
D.1 RANS T1



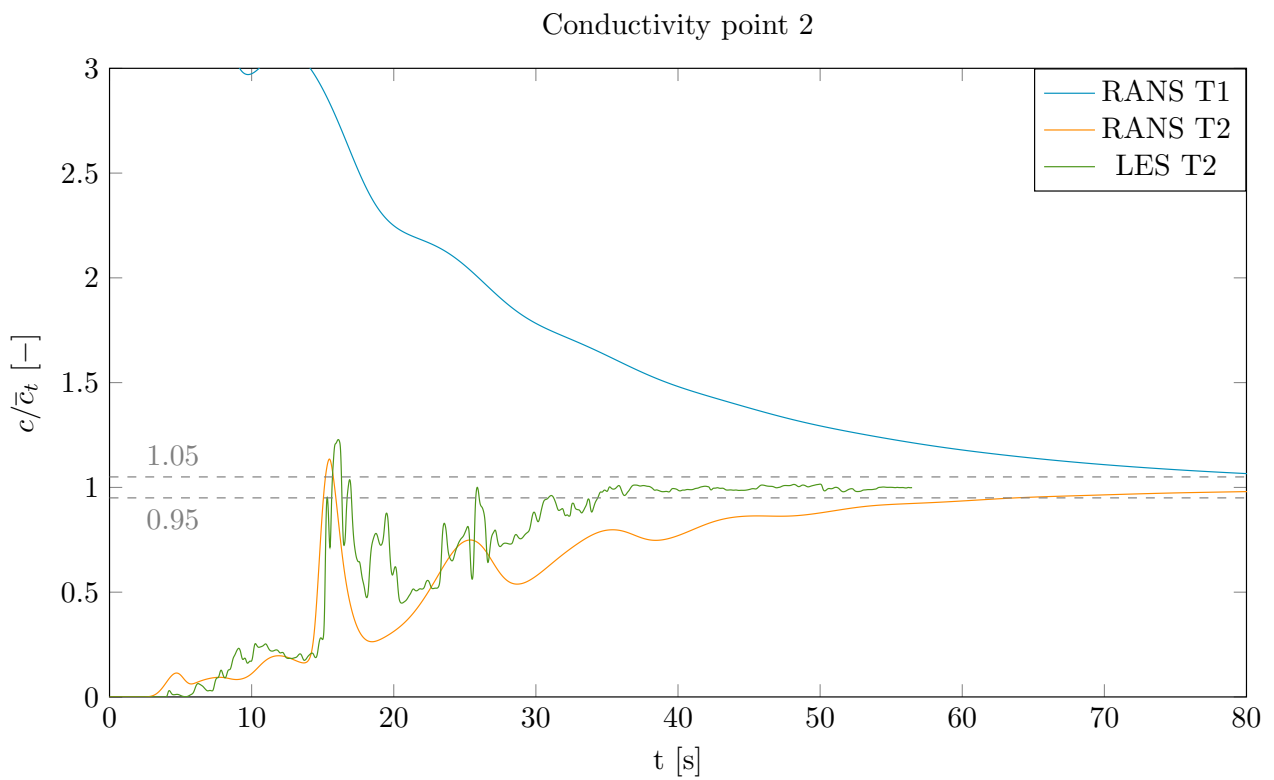
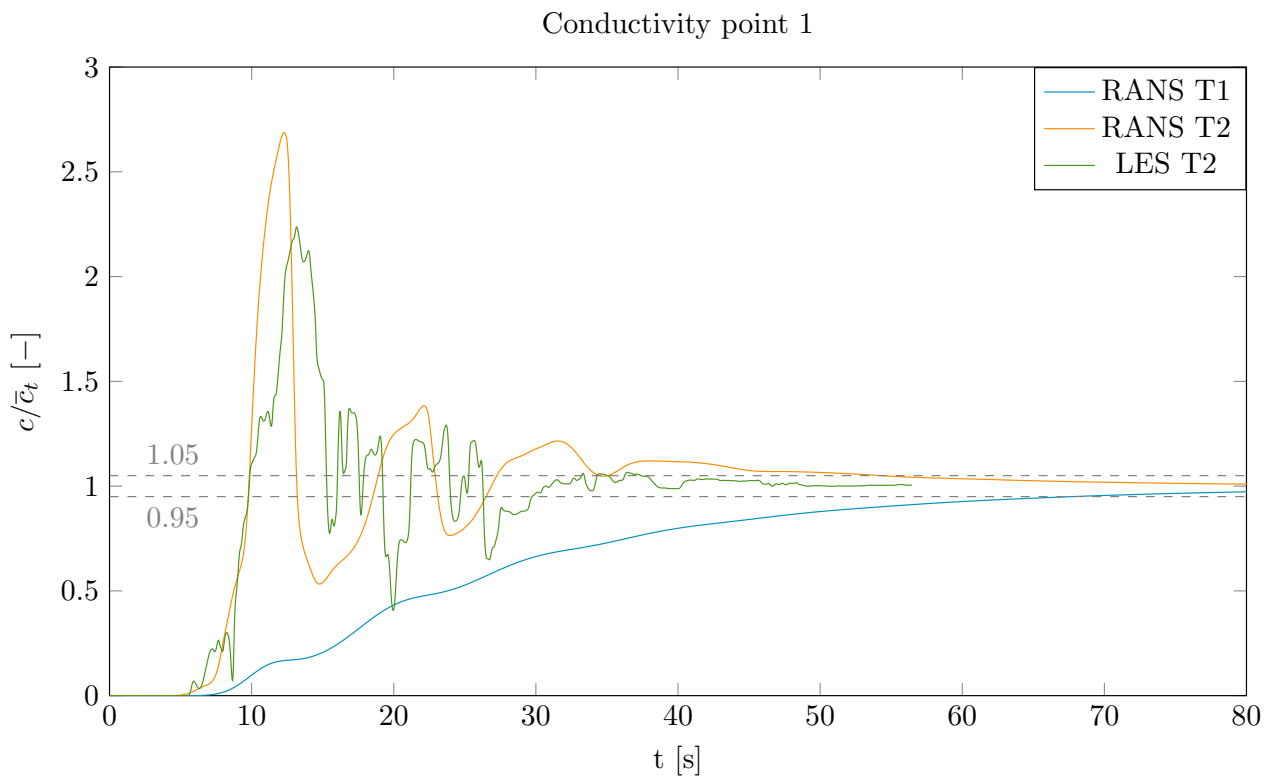
D.2 RANS T2



D.3 LES T2

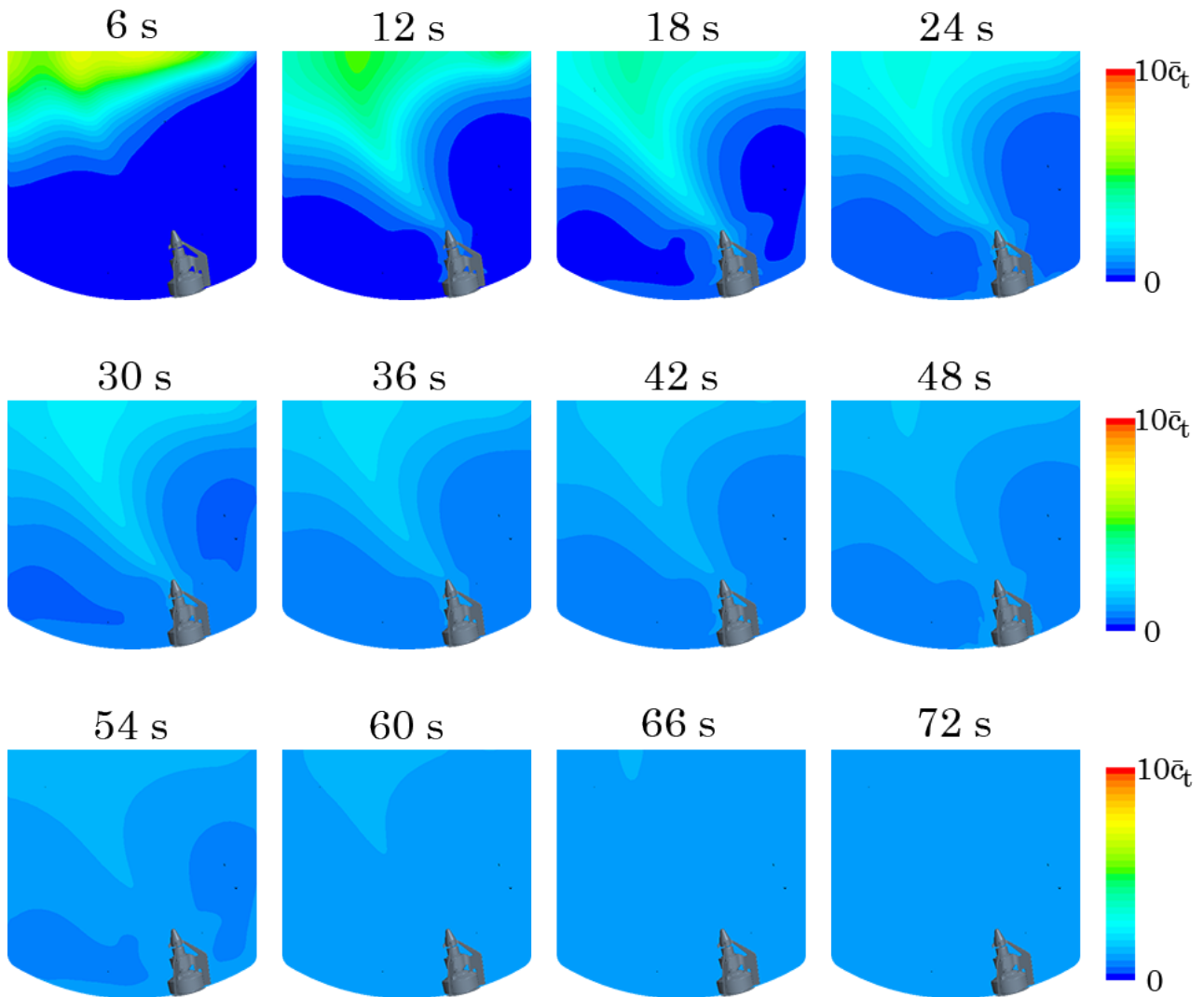


D.4 Normalized tracer concentration at conductivity points

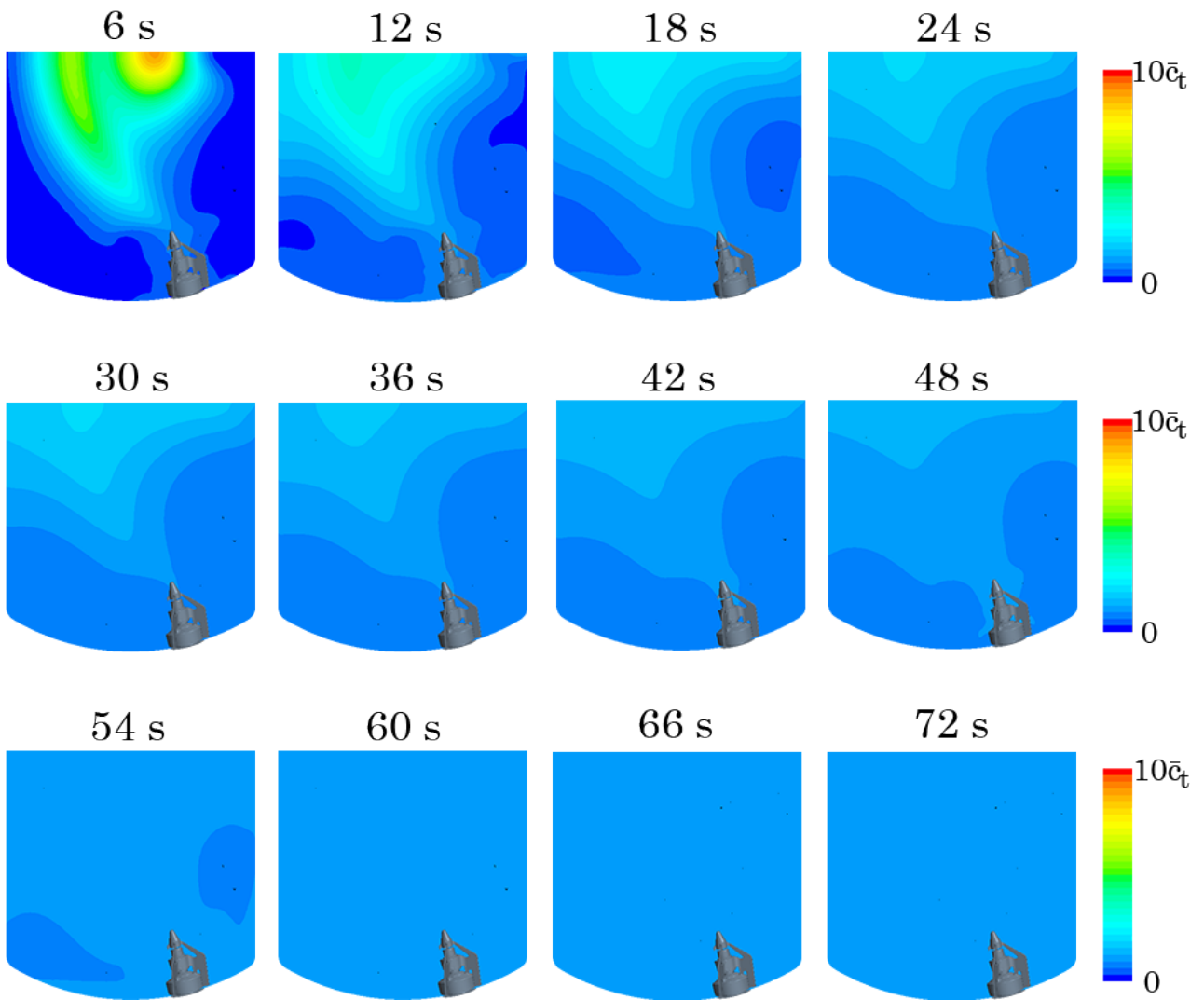


E Mixing process for different tracer shapes and placements

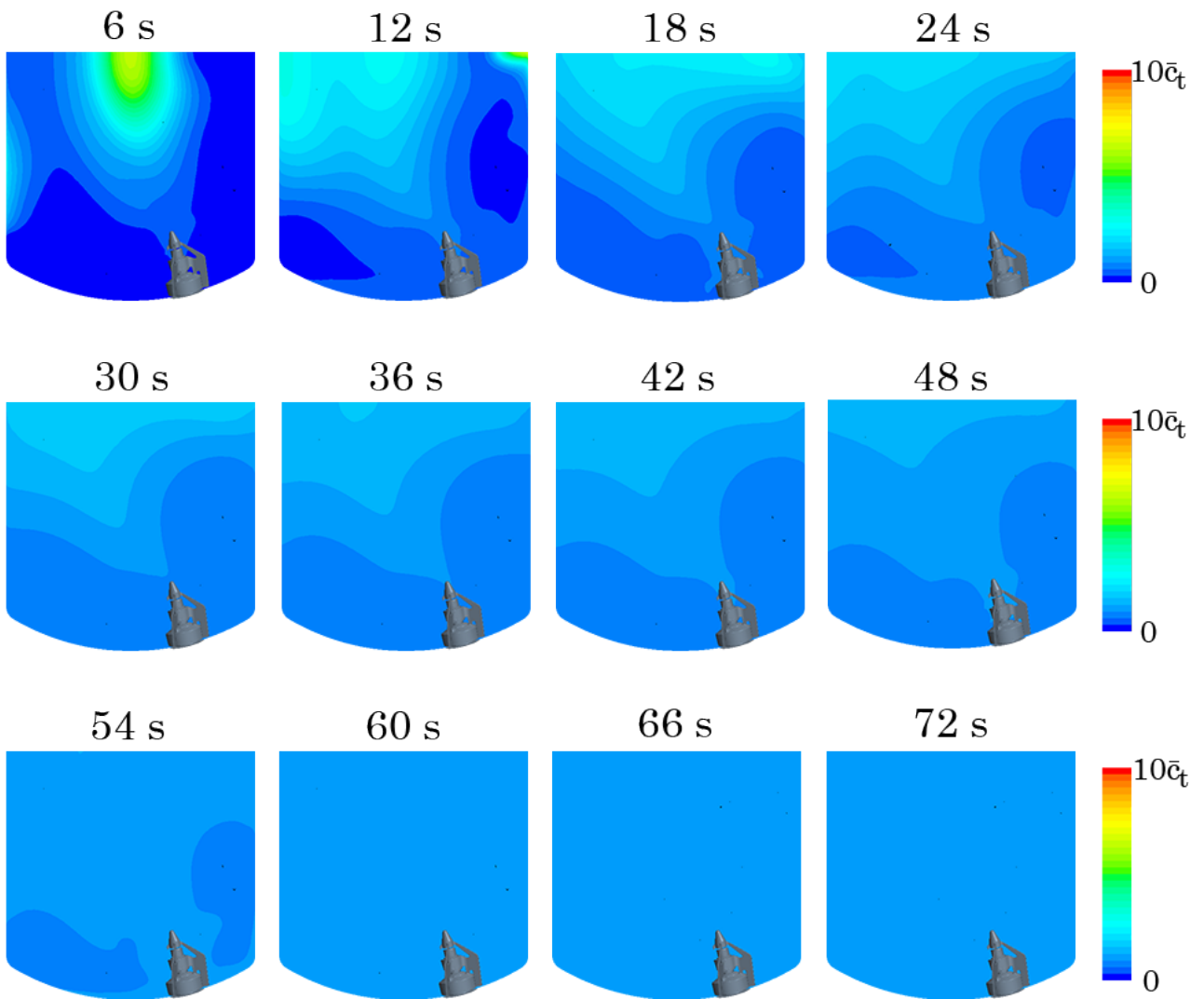
E.1 S1



E.2 S2



E.3 S3



E.4 S4

